

Université du Québec
Institut National de la Recherche Scientifique

Center for Materials, Energy and Telecommunications

**COMPARING THE CATALYTIC MECHANISMS OF DIFFERENT
SURFACE TERMINATIONS OF STRONTIUM TITANATE FOR THE
DEGRADATION OF ORGANIC POLLUTANTS**

par

Balasurya, SENTHILMURUGAN

Mémoire présenté pour l'obtention du grade de
Maître ès Sciences (M.Sc.)
en sciences de l'énergie et des matériaux

Jury d'évaluation

Président du jury et examinateur interne	Professor Shuhui Sun Institut national de la recherche scientifique Centre Énergie Matériaux Télécommunications
Examineur externe	Professor Eva Hemmer University of Ottawa Department of Chemistry and Biomolecular Sciences
Directeur de recherche	Professor Andreas Ruediger Institut national de la recherche scientifique Centre Énergie Matériaux Télécommunications

ACKNOWLEDGMENTS

While this MSc journey was adventurous, I wholly thank God for HIS divine enablement and providence. First and foremost, I would like to express my deep and sincere gratitude to the Center for Energy, Materials and Telecommunications, Institut national de la recherche scientifique - Université du Québec (INRS), Varennes, Canada that provided the productive environment to carry out this research for my MSc project. I am also grateful for the financial support received through the Mitacs Globalink Graduate Scholarship.

My profound gratitude goes to my research supervisor Prof. Andreas Ruediger for his encouragement, patience and the opportunity to pursue my MSc degree under his guidance at INRS-EMT. He gave me consistent motivation, valuable guidance, meticulous direction, and continuous support throughout my study.

I extend my thanks to Dr. Ifeanyichukwu Amaechi, Dr. Aparna Kharade and Katharina Kohlmann, to whom I owe a special gratitude. My heartfelt thanks go to my friend Amira Becheikh for her constant support and cooperation during my study. Her unwavering patience and encouraging words have been a source of motivation and strength. It was a privilege to have you as my colleague in this endeavor.

I am deeply grateful to my labmates for their unselfish help, encouragement, support, and trust every time. Thanks goes to my beloved lab mates Mohammad Bakhtbidar, Lilian Skokan, Maria Dekermenjian, Daniel Gueckelhorn, Elise Salmon and Aaron Dove for their friendly and encouraging atmosphere throughout my research period.

A special mention of thanks to Dr. Sudheer Khan for his moral support, his confidence and unwinding support that continue to be a source of motivation that boosted my confidence.

I am deeply grateful to my friends Dipon Kumar Ghosh, Afjalur Rahman, Vinayak Venkataraman, Kokilavani Shanmugasundaram, Harikumar Bethanasamy, Nirmal Anand, Swedha Madhu, Harini, Raaji, and Dinesh. I will always cherish the warmth shown by them and their presence filled my life with happiness and joy that will always be treasured.

I owe my heartfelt thanks to my cousin Premkumar Rajendran and my sister-in-law Kanchana Raman for their everlasting support in understanding of my goals and aspirations. I would like to express my gratitude to my cousin Vishvapriya Rajagopal for her moral support, which guided me to an awareness of my objectives and desires.

I would like to offer special thanks to my family for their tremendous understanding, encouragement, their unconditional love and optimistic support. I have no words to show how indebted I feel towards my beloved Father, Senthilmurugan and Mother, Nagajothi for giving me

the opportunity to pursue my dream. Their patience and sacrifice will remain my inspiration throughout my life.

ABSTRACT

In the past decades, environmental water pollution has emerged as a major challenge that calls for scalable water treatment as water scarcity adversely affects more than 40% of the world population. Semiconductor-based nanomaterials have been widely deployed as photocatalysts as they are effective in making use of the high-energy portion of the solar spectrum.

In this context, strontium titanate, a wide-band-gap semiconductor, offers a noticeable catalytic efficiency for waste water remediation. While the bulk properties have been subject to substantial investigation, research on the impact of the surface still remains in its infancy. Nanoparticles of strontium titanate provide for surfaces with different Miller indices but as these particles grow larger, two surface orientations prevail: (100) and (110). We focus on the (100) surface that has mixed terminations under otherwise arbitrary conditions of production: (100) planes have vicinal surfaces that are either SrO- or TiO₂-terminated. With two possible terminations, the question arises as to whether these surface terminations affect the catalytic performance.

We implement a strategy to control the surface terminations of SrTiO₃: (1) Hydrothermal etching removes the SrO layer, resulting in pure TiO₂-terminated SrTiO₃ and (2) Annealing above 1000°C under ambient atmosphere results in pure SrO-terminated SrTiO₃. Raman spectroscopy shows the signature of a carbonate (CO₃²⁻) contamination that selectively chemisorbs onto an SrO-terminated surface while it is not observed in a TiO₂-terminated SrTiO₃ surface. This carbonate signature is attributed to the adsorption of CO₂ onto SrO terraces causing the formation of SrCO₃. The photocatalytic activity of surface-engineered SrTiO₃ was evaluated to study the effects of surface terminations and the impact of SrCO₃ on the degradation of toxic pollutants.

A combination of catalytic processes (sono-, photo-catalysis) was employed to determine whether different catalytic mechanisms may be combined to accelerate the degradation of methyl orange as a model pollutant. Considering that strontium titanate is neither piezo-, nor pyroelectric, the focus of the investigation was on the effect of sono-catalysis, often attributed to cavitation under sonification.

A relevant question of this MSc thesis relates to the nature of the rate limiting step in catalytic reactions. Compared to their photovoltaic counterparts, where photogenerated charges deliver energy in an external circuit, commonly achieving energy conversion efficiencies of 0.1 (10%), the energy conversion efficiency of photocatalysts is roughly 4 to 5 orders of magnitude lower. This cannot be explained by any aspect of the light-induced charge transport inside the catalyst as it is exactly the same for photovoltaics and photocatalysts. We identify the mass transport at

the catalyst's surface as the rate limiting step and discuss the effect of sonification in terms of a positive contribution to mass transport.

Keywords: Photocatalysis; sono-catalysis ; waste-water remediation; light-induced charge transport.

RÉSUMÉ

Au cours des dernières décennies, la pollution de l'eau a émergé comme un défi majeur qui nécessite un traitement évolutif de l'eau, car la pénurie d'eau affecte plus de 40 % de la population mondiale. Les nanomatériaux à base de semi-conducteurs ont été largement déployés en tant que photocatalyseurs car ils sont efficaces dans l'utilisation de la partie à haute énergie du spectre solaire.

Dans ce contexte, le titanate de strontium, un semi-conducteur à large bande interdite, offre une efficacité catalytique notable pour l'assainissement des eaux usées. Si les propriétés globales ont fait l'objet d'études approfondies, la recherche sur l'impact de la surface n'en est encore qu'à ses balbutiements. Les nanoparticules de titanate de strontium présentent des surfaces avec différents indices de Miller, mais à mesure que ces particules grossissent, deux orientations de surface prévalent : (100) et (110). Nous nous concentrons sur la surface (100) qui présente des terminaisons mixtes dans des conditions de production par ailleurs arbitraires : les plans (100) présentent des surfaces vicinales terminées soit par du SrO, soit par du TiO₂. Avec deux terminaisons possibles, la question se pose de savoir si ces terminaisons de surface affectent la performance catalytique.

Nous mettons en œuvre une stratégie pour contrôler les terminaisons de surface de SrTiO₃: (1) la gravure hydrothermale élimine la couche de SrO, ce qui donne du SrTiO₃ à terminaison TiO₂ pure et (2) le recuit à plus de 1000°C sous atmosphère ambiante donne du SrTiO₃ à terminaison SrO pure. La spectroscopie Raman montre la signature d'une contamination par le carbonate () qui se chimisorbe sélectivement sur une surface à terminaison SrO alors qu'elle n'est pas observée sur une surface SrTiO₃ à terminaison TiO₂. Cette signature carbonatée est attribuée à l'adsorption de CO₂ sur les terrasses de SrO provoquant la formation de SrCO₃. L'activité photocatalytique de SrTiO₃ modifié en surface a été évaluée pour étudier les effets des terminaisons de surface et l'impact de SrCO₃ sur la dégradation des polluants toxiques.

Une combinaison de processus catalytiques (sono, photo-catalyse) a été employée pour déterminer si différents mécanismes catalytiques peuvent être combinés pour accélérer la dégradation de l'orange de méthyle comme polluant modèle. Étant donné que le

titanate de strontium n'est ni piézoélectrique, ni pyroélectrique, l'étude s'est concentrée sur l'effet de la sono-catalyse, souvent attribuée à la cavitation sous sonification. Une combinaison de processus catalytiques (sono-photocatalyse) a été employée pour déterminer si différents mécanismes catalytiques peuvent être combinés pour accélérer la dégradation de l'orange méthylique en tant que polluant modèle. Étant donné que le titanate de strontium n'est ni piézoélectrique, ni pyroélectrique, l'étude s'est concentrée sur l'effet de la sono-catalyse, souvent attribuée à la cavitation sous sonification.

Une question pertinente de cette thèse de maîtrise concerne la nature de l'étape limitant la vitesse dans les réactions catalytiques. Par rapport à leurs homologues photovoltaïques, où les charges photogénérées fournissent de l'énergie dans un circuit externe, atteignant généralement des rendements de conversion énergétique de 0,1 (10 %), le rendement de conversion énergétique des photocatalyseurs est inférieur d'environ 4 à 5 ordres de grandeur. Cela ne peut s'expliquer par aucun aspect du transport de charge induit par la lumière à l'intérieur du catalyseur, car il est exactement le même pour les cellules photovoltaïques et les photocatalyseurs. Nous identifions le transport de masse à la surface du catalyseur comme l'étape limitant le taux et discutons de l'effet de la sonification en termes de contribution positive au transport de masse.

Mots-clés : Photocatalyse ; sono-catalyse ; assainissement des eaux usées ; transport de charge induit par la lumière

TABLE OF CONTENTS

ACKNOWLEDGMENTS	<i>i</i>
ABSTRACT	<i>iii</i>
RÉSUMÉ	<i>v</i>
TABLE OF CONTENTS	<i>vii</i>
LIST OF FIGURES	<i>x</i>
LIST OF TABLES	<i>xiii</i>
LIST OF SYMBOL AND ABBREVIATIONS	<i>xiv</i>
1 INTRODUCTION	<i>1</i>
1.1. Photocatalysis	<i>2</i>
1.1.1. Photocatalyst.....	<i>2</i>
1.1.2. Photocatalytic mechanism	<i>2</i>
1.1.3. Surface reaction.....	<i>6</i>
1.1.4. Rate limiting step of photocatalysis	<i>7</i>
1.2. Sono-catalysis	<i>8</i>
1.2.1. Principles of sono-catalysis.....	<i>9</i>
1.2.2. Mechanism of sono-photocatalysis.....	<i>9</i>
1.2.3. Rate limiting step on sono-catalysis	<i>11</i>
1.3. Tribo-catalysis	<i>14</i>
1.3.1. Principle of tribo-catalysis.....	<i>14</i>
1.3.2. Mechanism of tribo-catalysis	<i>15</i>
1.3.3. Rate limiting step on tribo-catalysis	<i>15</i>
1.4. Piezo-catalysis	<i>16</i>
1.4.1. Principles of piezo-catalysis	<i>16</i>
1.4.2. Mechanism of piezo-catalysis.....	<i>18</i>
1.5. Flexo-catalysis	<i>21</i>
1.6. Reaction order	<i>21</i>
1.7. Efficiency indicator – degradation rate	<i>22</i>
1.8. Perspective of nanomaterial on catalysis	<i>23</i>
1.9. Methyl orange as a model pollutant	<i>24</i>
1.10. Nanomaterial as a catalyst	<i>24</i>
1.11. SrTiO₃ nanoparticles	<i>25</i>
1.12. Geometry and structural attributes of SrTiO₃	<i>26</i>
1.13. Application of SrTiO₃ on catalysis	<i>27</i>
1.14. Objective	<i>28</i>

2 EXPERIMENTAL TECHNIQUES	29
2.1. X-ray diffraction	29
2.2. Raman spectroscopy	30
2.2.1. Working principle	32
2.2.2. Modes of vibration	32
2.3. Transmission electron microscopy	34
2.4. X-ray photoelectron spectroscopy	35
2.5. Optical absorption (UV-VIS-NIR) spectroscopy	36
3 MATERIALS AND METHODS	38
3.1. Microwave assisted hydrothermal synthesis.....	38
3.2. Materials.....	38
3.3. Synthesis of SrTiO ₃	39
3.4. Photocatalytic experiment	39
3.5. Spectrophotometric set up to determine the optical density	40
3.6. Sono-photocatalytic experiment	41
3.7. Characterization of samples	42
3.8. Band structure determination	42
4 RESULTS AND DISCUSSION	43
4.1. X-ray diffraction	43
5.2. Raman spectroscopy	44
5.3. Transmission electron microscopy	44
5.4. X-ray photoemission spectroscopy	47
5.5. UV-visible-NIR spectroscopy.....	49
5.6. Photoluminescence of SrTiO ₃	50
5.7. Zeta potential.....	51
5.7. Photocatalysis	52
5.8. Sono-photocatalysis	53
5.9. Optimization of sono-photocatalytic activity of TiO ₂ terminated SrTiO ₃	65
5.10. Scavenging and photocorrosion.....	67
5.10. Tribo-catalysis of TiO ₂	71
6 CONCLUSION AND PERSPECTIVES	75
6.1. Conclusion	75
6.2. Perspectives	76
8 REFERENCES	77

Résume en Français.....	94
1. Introduction.....	94
1.2 Objectifs.....	95
1.3. Étape limitant la vitesse de la photocatalyse	95
1.4. Efficacité de conversion - photocatalyse	95
2. La méthodologie.....	96
2.1. Synthèse de SrTiO ₃	96
2.2. Expérience photocatalytique.....	97
2.3. Spectroscopie Raman	97
2.4. Photocatalyse	98
2.5. Sono-photocatalyse	99
3. Conclusion	111

LIST OF FIGURES

Figure 1. Band structure of different nanocatalysts with respect to NHE against redox potentials for different photocatalytic reactions [17].	3
Figure 2. (a) Schematic representation of photocatalysis mechanism [40] and (b) Solar spectrum (AM 0: Air Mass Zero, AM 1.5 G: Air Mass 1.5 Global and AM 1.5 D: Air Mass 1.5 Direct) [41].	5
Figure 3. The mechanism of cavitation (a) process of cavitation in a liquid due to acoustic waves and (b) stages of bubble cavitation dynamics in a liquid medium [58].	10
Figure 4. Schematic representation of the mechanism of sono-catalysis (a) hydroxyl radical generation on cavitation and (b) activation of catalyst by the energy produced on bubble collapse [53] (US – ultrasound and SL - sonoluminescence).	11
Figure 5. The phenomenon of cavitation at different temperatures (a) stages of bubble cavitation dynamics during sonocatalysis and (b) graph illustrating the radius $R(t)$ of a cavitating bubble over time [60].	14
Figure 6. Schematic illustration of tribo-catalytic effect [66].	15
Figure 7. Energy band tilting mechanism and subsequent piezo-catalytic radical formation [59].	19
Figure 8. Screening charge mechanism (a) Initial electrostatic balance: The catalyst begins in a state of electrostatic equilibrium with an internal polarization vector P_1 , (b) Release of charges: Upon mechanical deformation, the polarization changes to P_2 , leading to the release of charges from the catalyst surface, (c) Electrostatic rebalance: The system undergoes a rebalancing of electrostatic forces, with the polarization adjusting to P_3 and (d) Adsorption of charges: Finally, as the deformation is reversed, the polarization changes to P_4 , facilitating the adsorption of charges (e.g., O_2 and $\cdot OH$ tend to form $\cdot O^{2-}$ and $\cdot OH$) leading to the completion of the catalytic cycle [59].	20
Figure 9. Phase transitions of $SrTiO_3$. (a) The crystal structure of $SrTiO_3$, (b) Ferroelectric displacement. (c) Antiferrodistortive rotation.	25
Figure 10. Band diagram of $SrTiO_3$ against redox potentials of radical formation.	27
Figure 11. (a) Schematic representation of major components of an x-ray diffractometer, (b) diffraction of monochromatic x-rays on atomic planes of a material [99].	30
Figure 12. Schematic illustration of Raman spectroscopy and major components of a Raman Spectrometer [102].	31
Figure 13. Different light scattering processes (a) Rayleigh, (b) Stokes and (c) Anti-Stokes [104].	33
Figure 14. Different phonon modes (acoustic phonon and optical phonon).	33
Figure 15. Major components of a typical transmission electron microscope [106].	34
Figure 16. Schematic representation of the mechanism of photoemission leading to both Auger and photoelectrons in x-ray photoelectron spectroscopy [109].	36
Figure 17. Schematic representation of components of UV-VIS-NIR spectrophotometer [111].	37
Figure 18. Photocatalytic setup to perform degradation of methyl orange.	40
Figure 19. Optical setup to measure the transmittance of the reaction mixture.	41

Figure 20. Graphical illustration of sonophotocatalytic experiment for alternating sonification with photocatalysis.	41
Figure 21. XRD pattern of different surface engineered SrTiO ₃ (SrO- terminated and TiO ₂ -terminated and untreated SrTiO ₃).	43
Figure 22. Raman measurements of SrTiO ₃ samples.....	44
Figure 23. TEM images of TiO ₂ terminated (a), SrO terminated (b) and untreated SrTiO ₃ (c) nanoparticles.	45
Figure 24. TEM image (a), ImageJ processed (b), and the histogram plot on the surface of the nanomaterial (c), of untreated SrTiO ₃ (a1-3), SrO terminated (b1-3) and TiO ₂ terminated SrTiO ₃ (c1-3).....	46
Figure 25. Particle size distribution graph of TiO ₂ terminated (a), SrO terminated (b) and untreated SrTiO ₃ (c).	47
Figure 26. XPS spectrum of different surface terminated SrTiO ₃ samples.	49
Figure 27. (a) UV-VIS-NIR absorption spectra and (b) Tauc plots of SrTiO ₃ nanoparticles (normalized y axis).	50
Figure 28. Photoluminescence spectra of SrTiO ₃ samples.	51
Figure 29. Zeta potential analysis of TiO ₂ -terminated, SrO-terminated and untreated SrTiO ₃ samples.	51
Figure 30. Plots of C/C ₀ : (a) Time-dependent variation of C/C ₀ , and (b) linear fit for the photocatalytic degradation of methyl orange using SrTiO ₃ nanoparticles (MO – methyl orange, SrTiO ₃ :SrO – SrO terminated SrTiO ₃ and SrTiO ₃ : TiO ₂ – TiO ₂ terminated SrTiO ₃).	52
Figure 31. Plot of C/C ₀ (a), liner fit on plot C/C ₀ (b) on the sono-photocatalytic degradation of methyl orange by TiO ₂ terminated SrTiO ₃ nanoparticles.	54
Figure 32. Plot of the reaction rate of sono-photocatalytic activity versus sonification interval duration on the catalytic degradation of methyl orange against TiO ₂ -terminated SrTiO ₃	55
Figure 33. Plots of C/C ₀ : (a) Time-dependent variation of C/C ₀ , and (b) linear fit for the sono-photocatalytic degradation of methyl orange using TiO ₂ -terminated SrTiO ₃ , SrO-terminated SrTiO ₃ , and untreated SrTiO ₃ nanoparticles (sonication interval: 600 s, MO – methyl orange).	56
Figure 34. Sono-photocatalytic degradation of methyl orange using TiO ₂ : (a) Time-dependent variation of C/C ₀ , (b) linear fit of C/C ₀ , and (c) reaction rate as a function of sonication interval duration.....	58
Figure 35. Photocatalytic degradation of methyl orange by TiO ₂ -terminated SrTiO ₃ at room temperature (light-off pulse): (a) Time-dependent variation of C/C ₀ , (b) linear fit of C/C ₀ , and (c) reaction rate as a function of light- on and off pulse.	59
Figure 36. Sono-photocatalytic degradation of methyl orange at 60 °C by TiO ₂ -terminated SrTiO ₃ : (a) Time-dependent variation of C/C ₀ , (b) linear fit of C/C ₀ , and (c) reaction rate as a function of sonication duration.	62
Figure 37. Sono-catalytic degradation of methyl orange by TiO ₂ -terminated SrTiO ₃ at 60 °C (varying sonication interval): (a) Time-dependent variation of C/C ₀ , (b) linear fit of C/C ₀ , and (c) reaction rate as a function of sonication duration.....	64
Figure 38. Sono-catalytic degradation of methyl orange by TiO ₂ -terminated SrTiO ₃ : (a) Time-dependent variation of C/C ₀ , (b) ln(C/C ₀) at room temperature (600 s sonication	

interval), and (c) sonocatalytic effect of methyl orange at 25 °C and 60 °C (600 s sonication interval).....65

Figure 39. Plot of C/C_0 (a) and linear fit on plot C/C_0 (b) on the sono-photocatalytic degradation of methyl orange by TiO_2 terminated $SrTiO_3$ for different concentrations of methyl orange.....66

Figure 40. Plot of C/C_0 (a) and $\ln(C/C_0)$ (b) on the sono-photocatalytic degradation of methyl orange by TiO_2 terminated $SrTiO_3$ for different concentrations of the nanoparticle.67

Figure 41. Radical sequencing on the sono-photocatalytic degradation of methyl orange against TiO_2 terminated $SrTiO_3$ (a) plot of C/C_0 vs time and (b) linear fit on plot C/C_0 vs time.68

Figure 42. XRD patterns of TiO_2 terminated $SrTiO_3$ before and after catalysis (before irradiation - before catalysis and after irradiation - after catalysis).69

Figure 43. XPS spectrum of TiO_2 terminated $SrTiO_3$ before and after catalysis (before irradiation - before catalysis and after irradiation - after catalysis).70

Figure 44. (a) TEM image and (b) particle size distribution plot of TiO_2 terminated $SrTiO_3$71

Figure 45. Plot of C/C_0 (a), $\ln(C/C_0)$ (b) and the reaction rate versus concentration of TiO_2 (c) on the tribocatalytic degradation of methyl orange by TiO_272

Figure 46. Zeta potential measurement of different concentrations of TiO_273

LIST OF TABLES

Table 1. XPS peaks of Ti, Sr and O spectra of TiO ₂ -terminated, SrO-terminated, and untreated SrTiO ₃ nanoparticles.	48
Table 2. Rate constant and degradation percentage of methyl orange against SrTiO ₃ concentration (photocatalysis)	53
Table 3. Rate constant and degradation percentage of methyl orange of sono-photocatalysis in TiO ₂ -terminated SrTiO ₃ with varying sonification interval duration.....	54
Table 4. Rate constant and degradation percentage of methyl orange against TiO ₂ terminated SrTiO ₃ , SrO terminated SrTiO ₃ and untreated SrTiO ₃ nanoparticles (sono-photocatalysis at 600s sonification interval)	56
Table 5. Rate constant and degradation percentage of methyl orange against TiO ₂ (sono-photocatalysis)	57
Table 6. Rate constant and degradation percentage of methyl orange against TiO ₂ terminated SrTiO ₃ photocatalysis.	60
Table 7. Rate constant and degradation percentage of methyl orange against sono-photocatalysis in TiO ₂ terminated SrTiO ₃ at 60 °C.....	61
Table 8. Rate constant and degradation percentage of methyl orange against sono-catalysis in TiO ₂ terminated SrTiO ₃ at 60 °C.	63
Table 9. Rate constant and degradation percentage of methyl orange against sono-photocatalysis in TiO ₂ terminated SrTiO ₃ by varying the concentration of methyl orange.	66
Table 10. Rate constant and degradation percentage of methyl orange against sono-photocatalysis in TiO ₂ terminated SrTiO ₃ by varying the concentration of nanoparticle .	66
Table 11. Rate of the reaction and the degradation percentage of radical sequencing on the sono-photocatalytic degradation of methyl orange against concentration of TiO ₂ -terminated SrTiO ₃	67
Table 12. Zeta potential of different concentrations of TiO ₂	72
Table 13. Comparison table on catalytic degradation of methyl orange	74

LIST OF SYMBOL AND ABBREVIATIONS

AOP – Advanced oxidation process

UV-VIS-NIR – Ultraviolet (200 to 400 nm), visible (400 to 700 nm), near infrared (700 nm to 2500 nm)

CB – Conduction band

VB- Valance band

E_g – Band gap energy (eV)

E_{VB} – Valance band potential (eV)

E_{CB} – Conduction band potential (eV)

NHE – Normal hydrogen electrode

T – Temperature (K)

MO – Methyl orange

SrTiO₃ - Strontium titanate

SrTiO₃:TiO₂ – TiO₂ terminated strontium titanate

SrTiO₃:SrO – SrO terminated strontium titanate

e⁻ - Electron

h⁺ - Hole

ROS – Reactive oxygen species

•OH – Hydroxide radical

$\bullet\text{O}_2^-$ - Superoxide radical

ρ - Density

γ - Polytropic index

P – Pressure

ϵ_r - Relative permittivity

A – Absorbance

λ - Wavelength

V_a – Acceleration voltage

K_B - Boltzmann constant

J – Current density

Φ - Work function

BE – Binding energy

$h\nu$ - Photon energy

h – Planck's constant

KE – Kinetic energy

I – Intensity

FE - Ferroelectric

AFD – Antiferrodistortive

r_A, r_B, r_O – Ionic radii of anion, cation and oxygen

1 INTRODUCTION

In the past decade, water contamination has experienced a significant global rise, which results in shortages of fresh water mainly due to rapid urbanization and spreading industrialization [1-3]. The major source for water contamination is due to the ejection of toxic effluent (dyes, pigments, pesticides, pharmaceuticals etc.) into environmental waterbodies, causing hazardous effects on humans, plants and aquatic organisms [3-5]. According to the available literature, the technologies that exist for the removal or decontaminating the toxic pollutants are adsorption, osmosis, ozonation, treatment with active carbon, photolysis (with UV and H₂O₂) and other advanced oxidation processes [6-10]. Among the AOP, photocatalysis has attracted researchers owing to its promising abilities in converting solar energy to chemical energy, where the catalyst is excited by solar irradiation leading to the formation of free radicals for the mineralization of toxic pollutants [11-14]. Catalysis is widely used in large-scale water treatment techniques in industries for the effective bond damage on pollutants and thereby generally reduces the toxicity of the effluent. Exceptions where the reaction products have their own toxicity after photocatalysis exist and are subject to independent research that reaches far beyond the scope of this work. Earth-abundant metals have been given priority over rare earth metals and noble metal-based catalysts as scaling to industrial levels requires cost-effective materials [15, 16]. Semiconductor based nanomaterials have been widely used as photocatalysts as they are effective in light harvesting for efficient charge separation.

The main rate-limiting step in catalysis is the rate of mass transfer as the physics in photovoltaics and photocatalysis are the same. The main difference is the charge transport from catalyst to the pollutant in the case of photocatalysis whereas for photovoltaics, it is the collection of charge carriers in an external circuit using an internal electric field [17].

It should be mentioned that the use of nanoparticles for catalysis comes with the obvious advantage of a substantially increasing catalytic surface as the particle size decreases for a given mass of catalyst. While this trend is scientifically favourable, current research on nanoparticles, including this study, focuses on particle sizes for which no efficient technique to remove them from the water body exists. While this highlights the relevance of non-toxic catalysts, it touches two other domains of research: 1) nanotoxicology that relates to the toxicity of nanoparticles even though the bulk phase may not be toxic and 2) removal techniques for nanoparticles. While we

fully acknowledge the crucial importance of both domains of research, the present study focuses on the scientific merits of nanoscale photocatalysts made of materials with a non-toxic bulk phase.

TiO₂ based materials are widely used for catalytic water treatment, as they are relatively non-toxic, affordable on light harvesting for the conversion of solar to chemical energy [18, 19]. A further step led to the development of titanium-based perovskite (ABO₃ – A is cation and B is titanium) nanomaterials, enabling enhanced control over structural properties and improved photocatalytic performance for environmental and energy applications [20]. Strontium titanate, SrTiO₃ with perovskite structure (A²⁺B⁴⁺O²⁻₃) is an interesting emerging material in this regard [21-24]. SrTiO₃ has alternating stacked layers of SrO and TiO₂ along the [001] v direction [25]. As catalysis is a surface phenomenon, the surface engineering of SrTiO₃ should depend on the actual nature of the surface termination that may be either SrO or TiO₂ on {100} vicinal surfaces.

The combination of different catalytic (photo and sono-catalytic) processes including those that may favourably affect the mass transport as the rate-limiting step, should boost the catalytic efficiency of the nanoparticle. Technically, the surface engineering and the combination of different catalytic techniques should enhance the catalytic efficiency if mass transport can be promoted without excessive requirements for much additional energy.

1.1. Photocatalysis

Photocatalysis is generally described as one of the effective advanced oxidation processes that attracted interest for the development of a system for environmental remediation, water treatment and cleaner energy production [26]. Photocatalysis is generally considered to be an environmentally friendly method, as it uses renewable solar energy for water treatment or clean energy production. The most prominent examples of photocatalysis are the mineralization of organic pollutants in water bodies, hydrogen production and conversion of carbon dioxide to methanol, formic acid, and carbon mono-oxide [27-29].

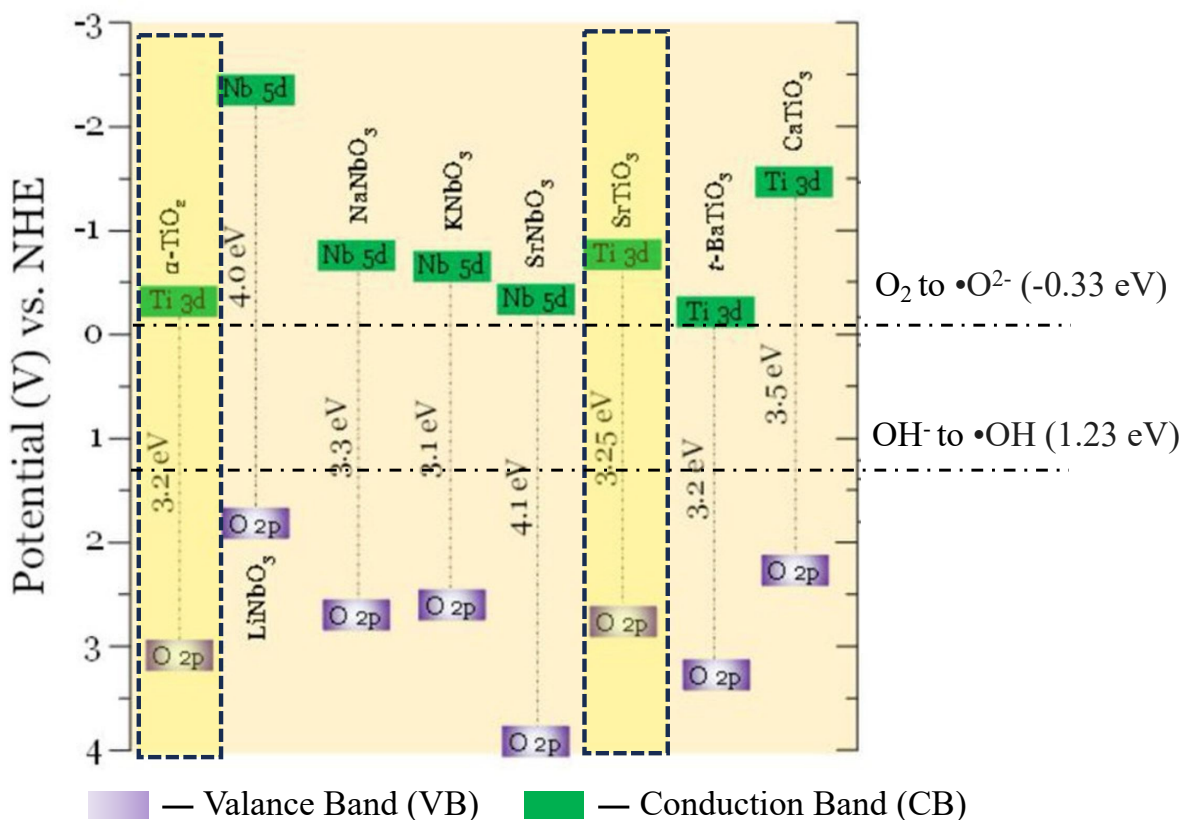
1.1.1. Photocatalyst

In general, photocatalysts are semiconducting materials (e.g: metal oxide, chalcogenides, organic framework etc.) which have their distinct electronic properties, and possess the ability to generate e⁻/h⁺ (e⁻ - electron and h⁺ - hole) pairs when external energy is provided beyond the threshold of bandgap energy [30-32]. Photocatalysts possess characteristic band gap which represented as the difference in the valance band (VB) and conduction band (CB). In the case of photo-excitation, only the direct band gap will be considered.

1.1.2. Photocatalytic mechanism

Photocatalytic mechanism is a multi step process (1) Photon absorption, (2) Exiton dissociation, (3) Charge transportation and (4) Mass transportation of product and reactant

Photon absorption: Firstly, the catalyst absorbs a photon (light energy) under irradiation, which enables the effective generation of an e^-/h^+ pair (exciton) provided that the photon energy exceeds the direct bandgap. Here, the electron in the valence band (VB) gets excited into the conduction band (CB) leaving a hole in the valence band [33, 34]. Nanoparticles may have band gaps that deviate from the bulk structure due to a variety of effects. The band diagram of a nanomaterial with its valence band (VB), conduction band (CB) and the normal hydrogen electrode (NHE) for the photo-oxidation and photo-reduction is illustrated in Fig. 1. The e^-/h^+ pair plays the prominent role in photocatalysis. For the photocatalytic experiments, the AM 1.5 G spectrum was employed to simulate solar irradiation conditions, closely matching the standard solar spectrum used in evaluating photocatalytic performance (Fig. 2b)



The band gap of the catalyst is indicated in dotted line

Figure 1. Band structure of different nanocatalysts with respect to NHE against redox potentials for different photocatalytic reactions [17].

Exciton dissociation: As a second step, the exciton needs to dissociate, as the presence of an electron and a hole results in radiative recombination (photoluminescence) that will annihilate

the exciton. In centrosymmetric materials, the only driving force to separate charge carriers in the valence or the conduction band is diffusion, a weak process that relies on either random motion of individual charge carriers or the electrostatic repulsion of simultaneously excited carriers. Recombination may not only occur at the site of the exciton generation but also during the transport to the surface, in particular when defect states (intentional dopants or unintentional contaminations) temporarily trap charge carriers on their way to the surface. Fortunately, the surface of a nanoparticle is not particularly far away from any exciton generation site in the bulk, however, there is also a noticeable number of possible defect states (again intrinsic or extrinsic) on the surface so that radiative recombination may eventually quench a large number of photogenerated carriers. The quantitative handle to monitor to what extent recombination adversely affects the photocatalytic process is the quantum efficiency of reactions per absorbed photon. The best technique to address recombination rates are fluorescence lifetime measurements, they however go beyond the scope of this work and will be part of my future PhD project in the group of Prof. Ruediger.

Charge transportation: Eventually, the excited e^- and h^+ take part in the photo-oxidation and photo-reduction on the surface for an effective formation of reactive oxygen species (ROS). And even then, whether or not these electrons and holes are able to trigger a chemical reaction depends on the energy of the respective bands and the stability of the bond that is targeted to be broken. For the case of an absorption of a photon with low energy in a semiconductor with low bandgap, there is not enough energy injected into the system to allow for a strong bond to be broken. The reference to determine the relative positions of the band energies in relation to the reduction and oxidation potentials of the molecule is illustrated in Fig. 1. Here, the standard potential for the oxidation and reduction, under irradiation corresponding to the normal hydrogen electrode (NHE), is 1.99 eV for the conversion of OH^- to $\bullet OH$ and -0.33 eV for the conversion of O_2 to $\bullet O^{2-}$. Any catalyst which possesses a higher CB (higher than -0.33 eV) will have sufficiently energetic electrons to react with the adsorbed oxygen in the water for the formation of superoxide radicals and the catalyst which possess a lower VB (lower than 1.99 eV) enables the effective conversion of a hydroxyl ion to a hydroxy radical (Fig. 1) [35, 36].

The generated radical species exhibit strong oxidation properties which could cleave the bond in the targeted organic pollutant and thus enable the mineralization of the toxic organic pollutant to a non-toxic form. There is an additional indirect mechanism in photocatalysis: after the effective separation of the e^-/h^+ pair, a reaction with adsorbed oxygen and water occurs for the formation of hydrogen peroxide (H_2O_2). The formed H_2O_2 is then converted to $\bullet OH$ [37-39]. Here, the formation of the ROS and interaction with the organic pollutant also enables the effective

mineralization of pollutants for water treatment. The schematic illustration on the photocatalytic degradation of toxic pollutants is illustrated in Fig. 2a.

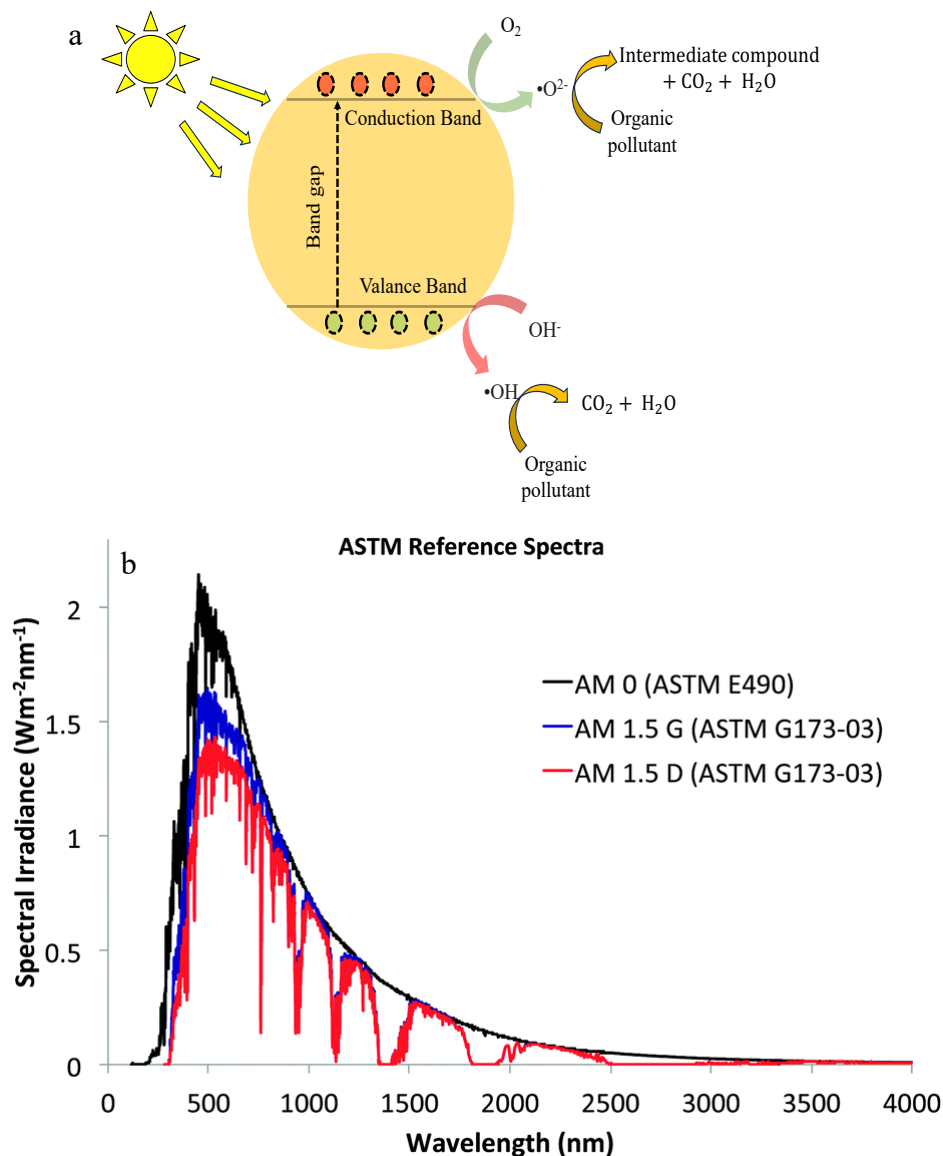


Figure 2. (a) Schematic representation of photocatalysis mechanism [40] and (b) Solar spectrum (AM 0: Air Mass Zero, AM 1.5 G: Air Mass 1.5 Global and AM 1.5 D: Air Mass 1.5 Direct) [41].

Photocatalysts such as TiO_2 , ZnO , $\text{g-C}_3\text{N}_4$, and CdS each have unique properties and applications. TiO_2 is highly stable and widely used for water splitting and air purification, though it primarily absorbs UV light [42]. ZnO has high electron mobility but suffers from photo corrosion. $\text{g-C}_3\text{N}_4$ is non-metallic and active under visible light, useful for hydrogen production, but has limited

active sites. CdS is efficient in the visible spectrum but is toxic and prone to photocorrosion [36]. In terms of the carrier life time, photostability SrTiO₃ is better than TiO₂ and other standard catalyst, offers excellent charge separation and is effective in UV light absorption, making it versatile for water splitting, CO₂ reduction, and pollutant degradation.

SrTiO₃ is chosen for several reasons. It offers excellent thermal stability and resistance to photocorrosion, crucial for long-term applications [43]. These characteristics make SrTiO₃ a versatile and effective photocatalyst for a range of environmental and energy-related applications.

1.1.3. Surface reaction

Photocatalysis is a surface reaction, where the reactive site of the catalyst interacts with the pollutant for the mineralization of the pollutant. In SrTiO₃ nanoparticles, the surface of the nanomaterial is determined by whether the sample is TiO₂- or SrO-terminated [44-46]. The (100) surface of SrTiO₃, a cubic perovskite material, can exhibit two primary terminations: SrO and TiO₂. These terminations significantly influence the surface properties and reactivity, impacting the material's suitability for applications such as photocatalysis. The TiO₂-terminated (100) surface is generally more chemically active due to the presence of exposed titanium ions, which facilitate electron transfer processes essential for photocatalytic reactions. In contrast, the SrO-terminated surface is less reactive, providing a different electronic structure and stability profile. Surface engineering techniques, such as annealing in controlled atmospheres or atomic layer deposition, are used to selectively stabilize these terminations. By carefully controlling the (100) surface termination, researchers can tailor the photocatalytic and electronic properties of SrTiO₃ to enhance its performance in various applications. For the case of an SrO termination, it is only a matter of time, usually a couple of hours, until the surface of the nanomaterial is contaminated with carbonate species, which is due to the stable confinement of SrCO₃ [47]. As a consequence, a large portion the reactive sites become occupied by CO₂, leaving fewer reactive sites for the effective adsorption of pollutant. In the case of TiO₂- terminated SrTiO₃ nanoparticles, the sites remain free of chemisorbates. The adsorption of the methyl orange on the catalyst is mainly due to the electrostatic attraction between the cationic pollutant and local charges on the surface of the catalyst. The adsorbed pollutant will then interact with the ROS formed by the catalyst under irradiation, upon the adsorption the pollutant breaks down into intermediates, then to even smaller non-toxic species and spontaneously desorbs from the catalytic surface.

The reaction mechanism of photocatalysis follows (1) to (7):

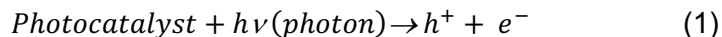


Photo-oxidation reaction



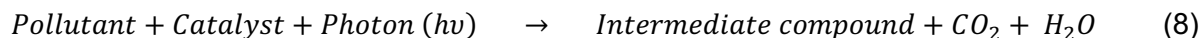
Indirect mechanism,



Photo-reduction reaction



Here, “•” represent radical formation. The photocatalytic reaction can be summarised as follows (8)



In the photocatalytic mechanism, photon absorption, exciton separation, and charge transport occur between pico to millisecond. However, mass transport processes—such as the adsorption and desorption of pollutants occur in microsecond, which act as the rate-limiting steps in photocatalysis.

1.1.4. Rate limiting step of photocatalysis

A first indication of the rate limiting factor can be obtained from the energy conversion rate from solar to chemical energy. The photovoltaic effect and photocatalysis are considered as very similar physical phenomena inside the nanomaterial. In photovoltaic devices, the nanomaterial is irradiated and then connected to an external circuit for the conversion of light energy into electrical energy (solar cell), whereas in photocatalysis the nanomaterial is irradiated and then the charge carriers cause the formation of radicals for chemical conversion. The photovoltaic effect is a process of the conversion of light energy to electrical energy, while photocatalysis is the conversion of light energy to chemical energy. The conversion efficiency of photovoltaics is in the order of 10^{-1} and the conversion efficiency of photocatalysis is substantially lower, typically in the range of 10^{-6} as we shall now estimate, corresponding to the literature [15]:

Considering it is a sunny day, where the pollutant can degrade 1 millimole of methyl orange in 1 h.

Conversion efficiency – photocatalysis:

$$Energy_{in} = P_{total} \left(\frac{W}{m^2} \right) \times Area (m^2) \times time(s) \quad (9)$$

Where P represents the power of the solar irradiation, A represents the area of illumination and time represents the illumination time [17].

Estimation for solar energy_{in}: 1 h of 1 kW/m² over 1 m² = 3600 kJ = 3.6 × 10⁶ J

Energy_{out}: 1 milli mole of pollutant (eg. methylene orange 327g/mol) mineralization (as usually seen from literature) [48, 49]

- Each broken bond is in the order of 1eV

- 1 milli mole of broken bonds: 1 eV × 6 × 10²³ × 10⁻³ = 96 J

$$\begin{aligned} \text{Conversion efficiency} &= \frac{energy_{out}}{energy_{in}} \\ &= \frac{96 J}{3.6 \times 10^6 J} \approx 2.67 \times 10^{-5} \end{aligned}$$

The conversion efficiency of degradation of 1 milli mole of methyl orange over 1 hour with one power sun is 2.67 × 10⁻⁵. Here, we even overestimated the quantity of broken bonds in typically reported photocatalytical degradation experiments [15].

Clearly, something other than the light-induced charge carrier formation causes the difference in these efficiencies. The key differences between photovoltaic devices and photocatalysts occurs at the surface, so we will focus on this part of the process.

1.2. Sono-catalysis

Sonocatalysis is a captivating branch of advanced oxidation processes (AOP). It is a process of producing charge carriers through high frequency ultrasound waves. There are two points to be mentioned: for one, the energy conversion efficiency of this process is inefficient since the mechanical energy to provide sonification is shaking the solvent, hence there is no selective process to activate the catalyst. For the other, it is not even clear if the catalyst gets activated in particular or if sono-catalysis is rather describing effects of an enhanced mass transport at the surface. On the other hand, photocatalytic process need to be stirred to enhance the mixing of the catalyst and the pollutant. Here, sonification might also act as a state of mixing the solution better for effective interaction of catalyst and pollutant.

There is however a debate about how sonification could cause catalytic activity through cavitation, the process of bubble generation in zones of low static pressure in the sonification bath [50]. These bubbles then collapse and are known to release very high energy density waves as they collapse with almost perfect spherical symmetry into a very small volume. Whether or not these

effects are sufficiently strong to generate charge carriers that may contribute directly to catalytic reactions is still the subject of investigation in the scientific community.

1.2.1. Principles of sono-catalysis

In sonocatalysis, catalysts are activation of the catalyst by high frequency ultrasound waves which facilitates catalysis. Briefly, the process enables the localized generation of microbubbles followed by bubble collapse on the reaction mixture. The rapid formation and collapse of microbubble (a shock pulse) generates high temperature and pressure [51-53]. The energy produced on the bubble collapse has been discussed in terms of the catalyst inducing charge carriers, that could effectively adsorb an ion of water on the surface of the catalyst for the effective formation of $\bullet\text{OH}$ and $\bullet\text{O}_2^-$ [54, 55].

1.2.2. Mechanism of sono-photocatalysis

The driving force of sono-catalysis as stated above is the phenomenon of bubble cavitation, which is induced by the external energy (high-frequency ultrasound wave) [53, 55]. Bubble cavitation occurs in two different mechanisms (i) the formation and collapse of the bubble, (ii) the growth of the bubble due to rarefaction and compression leads to the collapse of the bubble.

(i) Acoustic cavitation is the generation and action of cavities, or bubbles, in a liquid. When an acoustic field is applied to a liquid, sound waves move through the liquid and produce variations in the liquid's pressure. During the low-pressure portion (rarefaction) of the acoustic wave, if the pressure momentarily drops below the liquid's vapor pressure, it may promote transition of the surrounding liquid particles into the vapour phase, thereby generating a bubble cavity. After forming, these bubbles are set in motion by the macroscopic pressure wave. The pressure oscillations that create the bubbles also cause them to expand and contract. These cavities quickly become filled with dissolved gasses and/or vapour of the surrounding liquid. Gasses diffuse into the bubble upon expansion and leave the bubble during contraction. If the pressure variation is high enough, any cavities that are present will grow. As the surface tension can no longer sustain the pressure range increases, the bubble will collapse (Fig. 3a).

(ii) The alternating rarefaction and compression cycles of the ultrasound wave in the reaction mixture lead to pressure variations, with reduced pressure during rarefaction. This fluctuation promotes the nucleation of microbubbles rather than the formation of larger bubbles. The microbubbles expand progressively with each rarefaction and compression cycle until they reach a critical (Fig. 3b). At a certain point, the bubble undergoes internal cavitation (after reaching a critical size) on compression due to high pressure, causing the collapse of the microbubble and resulting in the release of high energy density [56, 57].

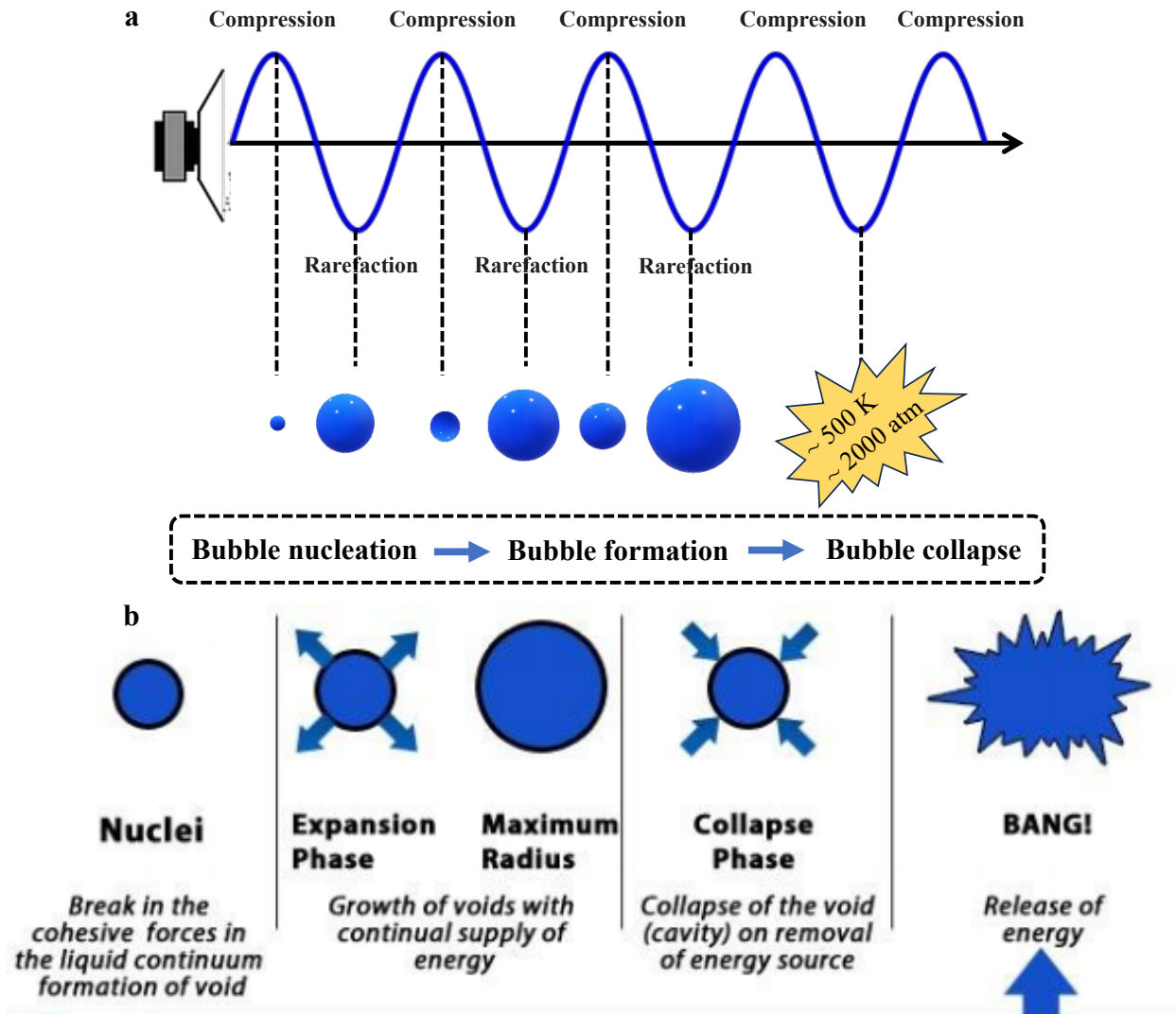


Figure 3. The mechanism of cavitation (a) process of cavitation in a liquid due to acoustic waves and (b) stages of bubble cavitation dynamics in a liquid medium [58].

Sonocatalysis can induce homogeneous nucleation and heterogeneous nucleation: (i) homogeneous nucleation: it occurs within the bulk of the liquid, where cavitation bubbles form spontaneously due to the acoustic pressure. This type of nucleation does not depend on the presence of any foreign particles or surfaces (ii) heterogeneous nucleation: It occurs on pre-existing surfaces or particles within the liquid. Heterogeneous nucleation results in the generation of heat and sonoluminescence (SL). The intrinsic collapse of the bubble generates high, strongly localized temperatures, pressures and sonoluminescence, which could activate the catalyst and may even enable electronic transitions that are required for charge carrier generation (Fig. 4). These charge carriers interact as outlined above with the water and adsorb oxygen, thus causing the formation of $\bullet\text{OH}$ and $\bullet\text{O}_2^-$. On the other hand, the intrinsic collapse produces hot spots, and

the hot spots interact with water, which results in the formation of $\cdot\text{OH}$ that facilitates the catalytic degradation of the toxic pollutant. In addition, the intrinsic collapse with high temperature and pressure provides better mixing of the reaction mixture.

The science of sonocatalysis is still in debate considering that the energy generated might not be enough to activate charge separation within the nanoparticle. The photon energy generated by sonoluminescence is negligible which might not be enough to trigger the reaction, whereas the additional mixing promotes the interaction of the pollutant and the active site of the catalyst. The interaction of the pollutant and catalyst under sonification improves the mass transfer and thus permits the mineralization of the toxic pollutant for water treatment [56]. Nevertheless, the activation of the nanomaterial or splitting of water for the formation of radical might not be the reaction mechanism in this catalytic process. Instead, the ultrasound waves could help to mix the solution better and thereby boost the catalytic efficiency.

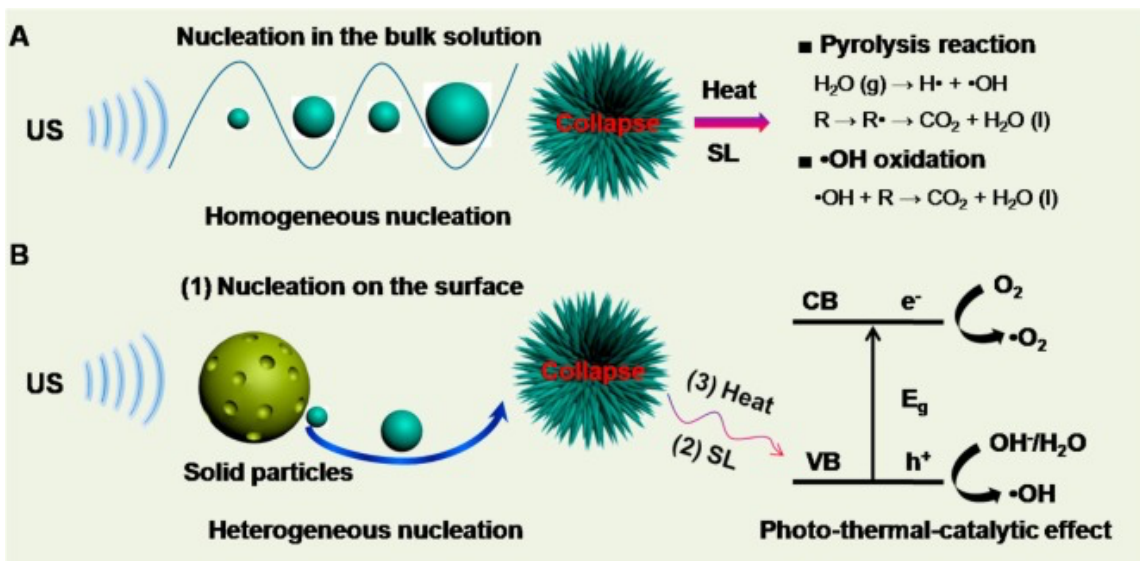


Figure 4. Schematic representation of the mechanism of sono-catalysis (a) hydroxyl radical generation on cavitation and (b) activation of catalyst by the energy produced on bubble collapse [53] (US – ultrasound and SL - sonoluminescence)

1.2.3. Rate limiting step on sono-catalysis

The factors that influence the sono-catalysis depend on the properties of the catalyst such as surface area, active site, and adsorption-desorption efficiency. The above factors determine the efficiency of the catalysis system on the degradation of the pollutants in the environmental water bodies. Further, sono-catalysis can be influenced by the frequency of the ultrasound wave used for bubble cavitation and thus have an influence on the bubble collapse, the generation of energy for the formation of radicals by hot spots in the water, and the mass transfer from the surface of

the catalyst. The two ways of radical formation in both mechanisms (homogeneous and heterogenous nucleation) of hot spot generation and activation of catalyst, therefore depend upon the ultrasound intensities [59]. The pressure and temperature generated on the intrinsic collapse of microbubbles can be described by ultrasound intensities (Eq. 10)

$$I_a = \frac{P_a^2}{2\rho c} \quad (10)$$

Here, P_a represents the acoustic pressure, ρ is the density of the medium and c is the speed of sound in the medium (Eq. 11)

$$T_{max} = T_0 \frac{P_m^{(\gamma-1)}}{P_0} \quad (11)$$

Here, P_m represents the peak pressure of the bubble (sum of the hydrostatic and acoustic pressure amplitude), γ represents the polytropic index, P_0 and T_0 represents the ambient pressure and temperature of the reaction mixture. The above equation represents the maximum temperature generated on bubble collapse (Eq. 12).

$$P_{max} = P_0 \left(\frac{P_m^{(\gamma-1)}}{P_0} \right)^{\frac{\gamma}{\gamma-1}} \quad (12)$$

The above equation represents the maximum pressure generated on bubble collapse, where ρ represents the density of the reaction mixture, c represents the speed of the ultrasound wave in the reaction mixture, γ represents the polytropic index, P_m represents the peak pressure of the bubble (sum of the hydrostatic and acoustic pressure amplitude), P_0 and T_0 represents the ambient pressure and temperature of the reaction mixture (Eq. 11 and 12). The temperature increase assists in bubble cavitation and thus facilitates the catalytic process for the effective degradation of pollutant in the reaction mixture.

Nevertheless, excessive temperature (higher than 60 °C) apparently inhibits the catalytic process [60] through an antagonistic effect. In addition, the intensive increase in the temperature on the catalyst surface can cause corrosion on the catalyst that could inhibit the kinetics of the catalytic process. The stages of bubble cavitation and dynamics of bubble growth is illustrated in Fig. 5a. The stages include quasi-static cavitation, explosive growth, bubble collapse, and the bubble bouncing back to quasi-static cavitation. The curve shows the changes in bubble radius, highlighting the dynamics of growth and collapse (Fig. 5b).

Understanding the factors influencing catalysis enables us to consider several optimization parameters for the sono-catalytic reaction for the mineralization of pollutants for water treatment.

Conversion efficiency – sonocatalysis:

Considering the degradation of methyl orange (30 micro molar) under sonification for 150 min [61].

$$Energy_{in} = P_{total} \left(\frac{W}{m^2} \right) \times Area (m^2) \times time(s)$$

Where P represents the power of the solar irradiation, A represents the area.

Estimation for sonification energy_{in}: 150 min of 150 W/m² over 1 m² = 1.3 x 10⁶ J

Energy_{out}: 1 milli mole of pollutant (eg. methylene orange 327g/mol) mineralization

- Each broken bond is in the order of 1eV

- 1 milli mole of broken bonds: 1 eV x 6x10²³ x 10⁻³ = 96 J

$$\begin{aligned} \text{Conversion efficiency} &= \frac{energy_{out}}{energy_{in}} \\ &= \frac{2.88 J}{1.3 \times 10^6 J} \approx 2.2 \times 10^{-6} \end{aligned}$$

At this point, we emphasize the difference between energy conversion efficiency and rate limiting steps. The energy conversion efficiency of sono-catalysis is very low (approx. 10⁻⁶) due to the requirement of mechanically activating the solvent, which is very dense and heavy. This energy is generally not for free, sonification is achieved through external mechanical motion, so that the overall energetic and economic scenario worsens, as soon as sonocatalysis is added to e.g. photocatalysis.

For a sono-catalysis process we need to plug in the catalytic reactor with the external energy (electrical energy) for the generation of ultrasound. Sonocatalysis should be considered as non-scalable to industrial scales of waste-water remediation, as it is simply not practicable to sonificate all the waste water of a major city for an extended period of time.

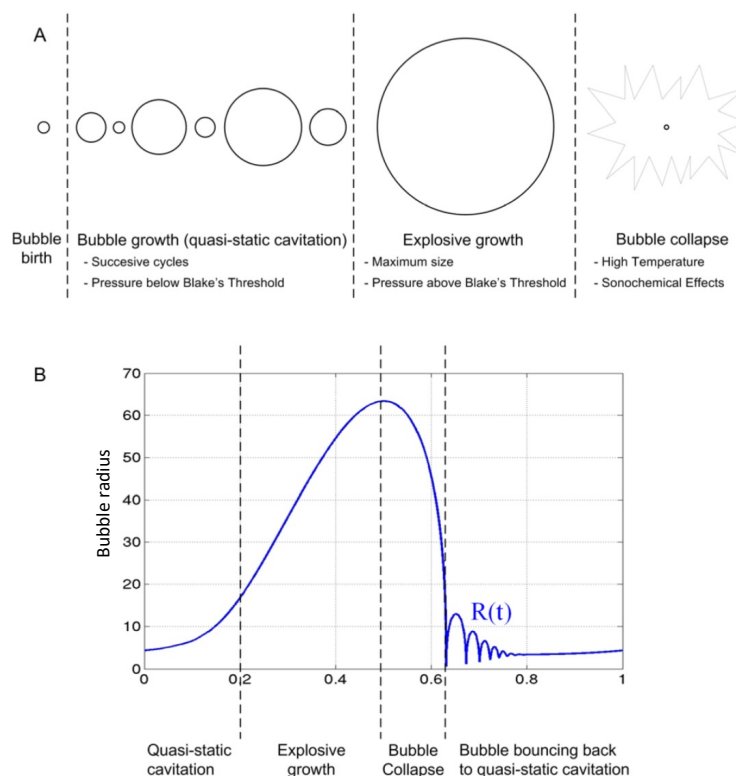


Figure 5. The phenomenon of cavitation at different temperatures (a) stages of bubble cavitation dynamics during sonocatalysis and (b) graph illustrating the radius $R(t)$ of a cavitating bubble over time [60].

1.3. Tribo-catalysis

Tribo-catalysis is another advanced oxidation processes, where mechanical energy is converted into chemical energy. Tribology is the science of friction and for sufficiently high concentrations of catalytic particles, friction should become noticeable and possibly contribute to the overall catalytic performance. Also, the use of stirrers and their contact with walls of reaction containers may contribute to overall efficiency. The following section introduces tribo-catalysis, its fundamental principle, mechanism, shortcomings and challenges.

1.3.1. Principle of tribo-catalysis

Tribo-catalysis is generally described as the activation of the nanomaterial through mechanical forces, to then generate charges at the interface of particles under friction. This way, static electricity was first observed in macromaterials when amber, a natural insulator, was rubbed against other insulators such as fur. The word "electron" originates from the greek word for amber. The application of tribo-catalysis can be shortly explained by the collision of the catalyst (friction or shear) with other particles including itself [62, 63]. Mechanical energy converted to chemical energy depends upon the frictional force and contact surface area of the catalyst. The generated

charge carriers then again react with the adsorbed O_2 and OH^- ions for the formation of radicals and then interact with the pollutant for the environmental water treatment.

1.3.2. Mechanism of tribo-catalysis

Tribo-catalysis is a collision phenomenon between the surfaces of nanoparticles. The mechanical collision of the catalyst may cause deformations and strains, which result in the formation free charges. Here, the generation of the active site and defects/strain enables the effective interaction of the catalyst and pollutant [62, 64]. This phenomenon is well summarized under the term “triboelectricity”.

The mechanical interaction between two catalytic surfaces causes intermolecular interactions on each surface leading to the tribo-electric effect (Fig. 6). The electrostatic interaction on the surface of the catalyst, which necessarily has to be an insulator, enables the charge separation, followed by interaction with adsorbed oxygen and water for the effective formation of the $\cdot OH$ and $\cdot O_2^-$. These radicals interact with the targeted pollutant and cause the aforementioned bond cleavage resulting in the mineralization of the targeted pollutants pollutant (azo dye, antibiotic, beta-blockers and other toxic pollutants) [65] [63].

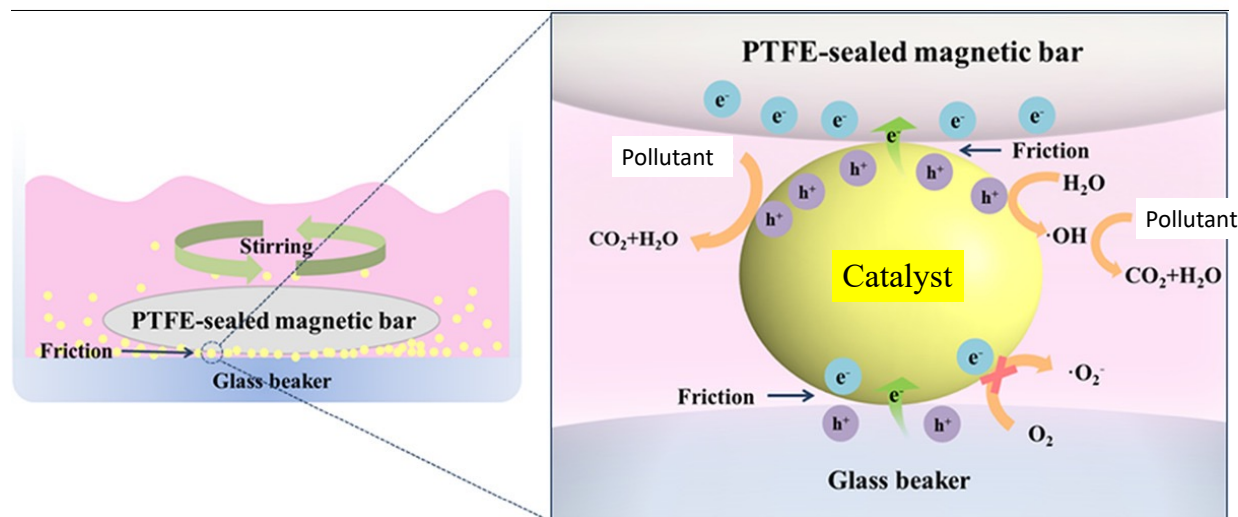


Figure 6. Schematic illustration of tribo-catalytic effect [66].

1.3.3. Rate limiting step on tribo-catalysis

As tribo-catalysis is the conversion of mechanical energy to chemical energy, the two main factors that affect the catalytic reaction as the intensity of the mechanical force and the

concentration of the catalyst. The viscosity of the solvent also plays a noticeable role. The higher the density of the catalyst, the higher the probability of collisions, which could increase the probability of friction. Examples are mechanical stirring by using Teflon bar. On the other hand, the physical properties of the nanomaterial will also influence the rate of tribo-catalysis. Tribocatalysis is to be considered omnipresent due to the necessity of either stirring or sonification in order to avoid sedimentation of insoluble components. The extent to which it contributes however depends on the nature of the materials. Polymeric insulators tend to have a much stronger capability to generate and retain charges through friction than inorganic materials [<https://www.nature.com/articles/s41467-019-09461-x>] leading to the observation that stirring with a teflon-coated magnetic stirrer leads to noticeable catalytic effects. These effects have to be carefully discriminated against intended effects through e.g. piezo, - or photocatalysis.

1.4. Piezo-catalysis

Piezo-catalysis is an emerging oxidation process, with an interesting potential to improve mass transport near the catalyst surface. The phenomenon of piezo-electric effect is the conversion of mechanical energy (like compression, expansion, and shear) to electric energy in form of bound surface charge density [67-69]. The application of the thermodynamically reversible piezo-electric effect is the conversion of mechanical energy to chemical energy on catalytic degradation of organic contaminant by an insulating crystalline material that lacks inversion symmetry. The following section introduces various aspects of piezo-catalysis, their fundamental principles and mechanism.

1.4.1. Principles of piezo-catalysis

Piezo-electric materials lack inversion symmetry (also referred to as being non-centrosymmetric) so that an applied mechanical stress may translate into the formation of an electric dipole, which, integrated over the volume of the sample, is quantified as a dielectric polarization. The conversion of the energy is given by Eq. 13 and 14.

$$D_k = d_{kij}T^{ij} \quad (13)$$

$$S_{ij} = d_{kij}^*E^k \quad (14)$$

where, D represents the dielectric displacement, which linearly depends upon the applied mechanical stress (T), coupled through a 3rd rank tensor of the direct piezoelectric effect, d . S represents the strain induced due to the piezo-electric effect which linearly depends upon the applied electric field (E), also known as the converse piezoelectric effect. Here, d_{ijk} and d_{kij} are the respective elements of the piezoelectric tensor that are numerically identical given that the piezoelectric effect is thermodynamically reversible. A strain tensor is a 2nd rank symmetric tensor,

the symmetric tensor can be identified by $S_{11}=S_1$, $S_{22}=S_2$, $S_{33}=S_3$, $S_{23}=S_4$, $S_{13}=S_5$ and $S_{12}=S_6$ using the Voigt notation. This notation represents that the piezo-electric co-efficient depends on the reduced Voigt matrix (d_m) as given in Eq.5, where k represents the electric displacement (D) or electric field (E), and T, the stress or S strain ($m = 1, 2, 3, 5$ and 6) ($d_{km} = d^*_{km}$)

$$\begin{pmatrix} d_{11} & d_{12} & d_{13} & d_{14} & d_{15} & d_{16} \\ d_{21} & d_{22} & d_{23} & d_{24} & d_{25} & d_{26} \\ d_{31} & d_{32} & d_{33} & d_{34} & d_{35} & d_{36} \end{pmatrix} = \begin{pmatrix} d_{111} & d_{122} & d_{133} & d_{144} & d_{155} & d_{166} \\ d_{211} & d_{222} & d_{233} & d_{244} & d_{255} & d_{266} \\ d_{311} & d_{322} & d_{333} & d_{344} & d_{355} & d_{366} \end{pmatrix} \quad (15)$$

Piezo-electric coupling in the form of built strain-charge is represented in (Eq. 16 and 17)

$$\{S\} = [s^E]\{T\} + [d^t]\{E\} \quad (16)$$

$$\{T\} = [d]\{T\} + [\varepsilon^T]\{E\} \quad (17)$$

where, ε^T and S represents the dielectric permittivity and elastic compliance. The strain equation for poled piezoelectric material (e.g. barium titanate (BaTiO₃, 4mm crystal class) and lead zirconate titanate (Pb(Zr_xTi_{1-x})O₃), an industrially relevant piezoelectric material that is present in almost all injection valves in car manufacturing) can be simplified and given by Eq. 18.

$$\begin{bmatrix} S_1 \\ S_2 \\ S_3 \\ S_4 \\ S_5 \\ S_6 \end{bmatrix} = \begin{bmatrix} S_{11}^E & S_{12}^E & S_{13}^E & S_{41}^E & S_{51}^E & S_{61}^E \\ S_{12}^E & S_{22}^E & S_{23}^E & S_{42}^E & S_{52}^E & S_{62}^E \\ S_{13}^E & S_{23}^E & S_{33}^E & S_{43}^E & S_{53}^E & S_{63}^E \\ S_{14}^E & S_{24}^E & S_{34}^E & S_{44}^E & S_{54}^E & S_{64}^E \\ S_{15}^E & S_{25}^E & S_{35}^E & S_{45}^E & S_{55}^E & S_{65}^E \\ S_{16}^E & S_{26}^E & S_{36}^E & S_{46}^E & S_{56}^E & S_{66}^E \end{bmatrix} \cdot \begin{bmatrix} T_1 \\ T_2 \\ T_3 \\ T_4 \\ T_5 \\ T_6 \end{bmatrix} + \begin{bmatrix} d_{11} & d_{21} & d_{31} \\ d_{12} & d_{22} & d_{32} \\ d_{13} & d_{23} & d_{33} \\ d_{14} & d_{24} & d_{34} \\ d_{15} & d_{25} & d_{35} \\ d_{16} & d_{26} & d_{36} \end{bmatrix} \cdot \begin{bmatrix} E_1 \\ E_2 \\ E_3 \end{bmatrix}$$

$$\begin{bmatrix} D_1 \\ D_2 \\ D_3 \end{bmatrix} = \begin{pmatrix} d_{11} & d_{12} & d_{13} & d_{14} & d_{15} & d_{16} \\ d_{21} & d_{22} & d_{23} & d_{24} & d_{25} & d_{26} \\ d_{31} & d_{32} & d_{33} & d_{34} & d_{35} & d_{36} \end{pmatrix} \cdot \begin{bmatrix} T_1 \\ T_2 \\ T_3 \\ T_4 \\ T_5 \\ T_6 \end{bmatrix} + \begin{bmatrix} \varepsilon_{11}^X & \varepsilon_{21}^X & \varepsilon_{31}^X \\ \varepsilon_{12}^X & \varepsilon_{22}^X & \varepsilon_{32}^X \\ \varepsilon_{13}^X & \varepsilon_{23}^X & \varepsilon_{33}^X \end{bmatrix} \cdot \begin{bmatrix} E_1 \\ E_2 \\ E_3 \end{bmatrix}$$

$$\begin{bmatrix} S_1 \\ S_2 \\ S_3 \\ S_4 \\ S_5 \\ S_6 \end{bmatrix} = \begin{bmatrix} S_{11}^E & S_{21}^E & S_{31}^E & & & \\ S_{12}^E & S_{22}^E & S_{32}^E & & & 0 \\ S_{13}^E & S_{23}^E & S_{33}^E & & & \\ & & & S_{44}^E & 0 & \\ & & & 0 & S_{44}^E & \\ & 0 & & 0 & 0 & \\ & & & 0 & 0 & 2 \cdot (S_{11}^E - S_{12}^E) \end{bmatrix} \cdot \begin{bmatrix} T_1 \\ T_2 \\ T_3 \\ T_4 \\ T_5 \\ T_6 \end{bmatrix} + \begin{bmatrix} 0 & 0 & d_{31} \\ 0 & 0 & d_{32} \\ 0 & 0 & d_{33} \\ 0 & d_{15} & 0 \\ d_{15} & 0 & 0 \\ 0 & 0 & 0 \end{bmatrix} \cdot \begin{bmatrix} E_1 \\ E_2 \\ E_3 \end{bmatrix}$$

$$\begin{bmatrix} D_1 \\ D_2 \\ D_3 \end{bmatrix} = \begin{pmatrix} 0 & 0 & 0 & 0 & d_{15} & 0 \\ 0 & 0 & 0 & d_{15} & 0 & 0 \\ d_{31} & d_{32} & d_{33} & 0 & 0 & 0 \end{pmatrix} \cdot \begin{bmatrix} T_1 \\ T_2 \\ T_3 \\ T_4 \\ T_5 \\ T_6 \end{bmatrix} + \begin{bmatrix} \varepsilon_{11}^X & 0 & 0 \\ 0 & \varepsilon_{22}^X & 0 \\ 0 & 0 & \varepsilon_{33}^X \end{bmatrix} \cdot \begin{bmatrix} E_1 \\ E_2 \\ E_3 \end{bmatrix} \quad (18)$$

The piezo-electric materials can be evaluated by the piezo-electric coupling coefficient (k , electromechanical coupling factor), which linearly depends on the ratio of converted energy ($U_{\text{converted}}$) and input energy (U_{input}) (Eq. 19)

$$k = \sqrt{\frac{U_{\text{converted}}}{U_{\text{input}}}} \quad (19)$$

piezo-electric coefficient for the defined geometry is given by Eq. 20

$$k_{31} = \frac{d_{31}}{\sqrt{s_{11}^E \epsilon_{33}^X}} \quad (20)$$

where ϵ_{33}^X represent the dielectric permittivity of the material [59]. The reason to introduce a coupling factor is in the fact that soft materials are not able to transmit deformations to the environment as effectively as stiffer materials. Only because a material has high piezoelectric coefficients (tensor elements) does therefore not imply that the energy conversion rate is particularly high.

For the same reasons that sono-, and tribocatalysis are problematic in terms of energy efficiency, piezoelectric catalysis also requires the activation of the solvent, making it inefficient in terms of energy conversion. Moreover, strontium titanate is centro-symmetric, so that contributions from piezoelectricity are not expected. We however introduce piezocatalysis here as it is present in the aforementioned structurally related materials such as barium titanate.

1.4.2. Mechanism of piezo-catalysis

Piezo-catalytic mechanism of the catalyst has been explained by two mainstream theories (i) energy band theory and (ii) screening charge effect.

Energy band theory: Few author pretend to state that the mechanical strain acts on the catalyst, it induces a linear electric field as rationalized above on the catalyst resulting in the tilting of the energy band level (CV and VB), shown in Fig. 7, thereby resulting in the change in the potential of VB and CB that could endure the conversion of O_2 to $\bullet O_2^-$ (oxidation) and OH^- to $\bullet OH$ (reduction). Secondly, the formation of the dipoles on the catalyst enables the effective adsorption and desorption of ionic and dipolar pollutants, which increases the catalytic performance on mineralization of pollutants for environmental water treatment [70, 71].

The band tilting model, as popular as it is in literature, is wrong as can be seen from the analogy to photovoltaics. If a catalytical reaction is already possible without the presence of the piezoelectric effect, then the band tilting would not add anything positive to it. While it appears on first sight, that electrons would extend higher into the conduction band and holes deeper into the valance band, charge transport occurs along the edges of the band, so that the additional energy

that the electrons and holes receive, would be immediately dissipated through non-radiative processes, just the same way as this happens in photovoltaics [72].

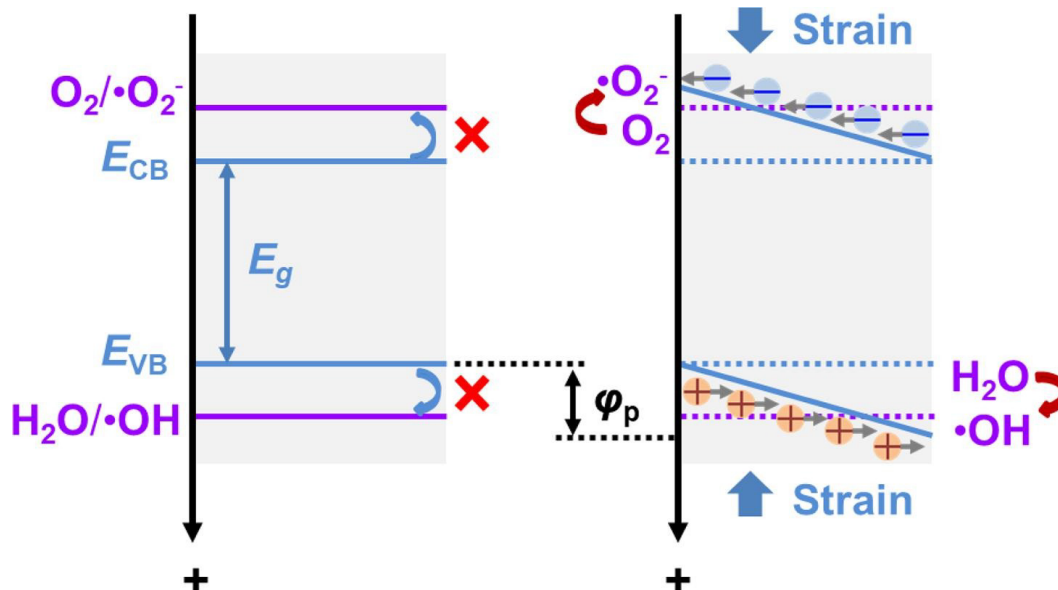


Figure 7. Energy band tilting mechanism and subsequent piezo-catalytic radical formation [59].

Screening charge effect: Here, the mechanical stress induces a dielectric polarization inside the catalyst expressed as bound surface charge density. As mentioned above, this dielectric polarization is the volume integral of all the dipoles across the sample and can be expressed following Gauss' theorem as a surface charge density of bound charges. It is important to state that charges related to the piezoelectric effect are bound and not free, so they cannot directly contribute to the catalytic reaction. Dipoles only interact through the electric field that they generate and that may become very substantial given the small dimensions of the nanoparticles. The dielectric polarization of piezoelectric material is compensated through free surface charges, providing charge neutrality on the surface (Fig. 8). Secondly, the release of charges enables the effective conversion of O₂ to •O₂⁻ (oxidation) and OH⁻ to •OH (reduction) and then follows the interaction of the pollutant with the free radical for catalytic degradation of the contaminant in water bodies [73, 74].

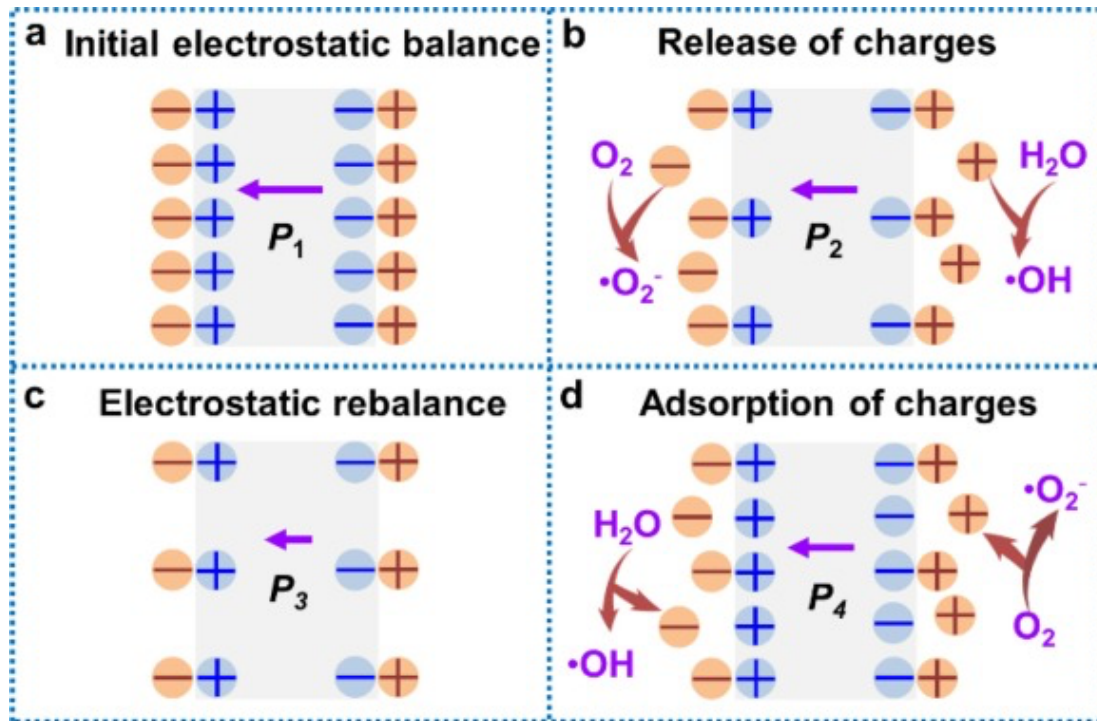


Figure 8. Screening charge mechanism (a) Initial electrostatic balance: The catalyst begins in a state of electrostatic equilibrium with an internal polarization vector P_1 , (b) Release of charges: Upon mechanical deformation, the polarization changes to P_2 , leading to the release of charges from the catalyst surface, (c) Electrostatic rebalance: The system undergoes a rebalancing of electrostatic forces, with the polarization adjusting to P_3 and (d) Adsorption of charges: Finally, as the deformation is reversed, the polarization changes to P_4 , facilitating the adsorption of charges (e.g., O_2 and $\cdot OH$ tend to form $\cdot O_2^-$ and $\cdot OH$) leading to the completion of the catalytic cycle [59].

In screening charge theory, the density of the surface screening is linearly dependent on the piezo-electric potential. The screening charge density (σ_s) in relationship with the polarization of the catalyst (P) is given by Eq. 21.

$$\sigma_s = \frac{d \cdot P}{\varepsilon_r(\delta_1 + \delta_2) + d} \quad (21)$$

where, d represent the thickness of the catalyst, ε_r represent the relative permittivity, δ_1 and δ_2 represent the screening layer on both the electrodes respectively.

In summary, piezo-catalytic degradation of the pollutant can be achieved only with a piezo-electric material. Here, $BaTiO_3$ is an example of a piezoelectric material and recent literature shows that $BaTiO_3$ is more effective than e.g. TiO_2 on the catalytic degradation of pollutants in water [75, 76].

Nevertheless, SrTiO₃ is a non-piezoelectric material where piezo-catalysis is prohibited by symmetry so we will only expect sono-catalysis and tribo-catalysis upon mechanical excitation [77].

1.5. Flexo-catalysis

Flexo-catalysis is a coupling behaviour of mechanical and electronic behaviour, where the mechanical strain gradient upon mechanical stress induces the dipole moment. Flexo-catalysis is a phenomenon following the flexo-electric effect, where the mechanical response in the form of a strain gradient is converted to electric energy for the charge separation and formation of free radicals for the degradation of pollutant [78]. Here, the powder nanomaterials in water media shows very low conversion efficiency on the conversion of mechanical energy to chemical energy and thereby it is neglected in the catalytic process of liquid phase catalysis. The basic idea of flexoelectricity is that any material that is experiencing strain gradients may produce a dielectric polarization and while the effects were demonstrated [79, 80], they remain quantitatively very low and appear to be a feature of current literature with a limited range of applications.

1.6. Reaction order

Kinetics are used to study the rate of the reaction and factors that influence the rate of the reaction like temperature, reactant concentration, and catalysts. The reaction order illustrates the impact of reactant concentration on the rate of the reaction.

For a reaction $A \rightarrow B$

$$\text{Rate} = [A]^x[B]^y$$

Here, A and B are the reactant and product, x and y are the orders of the reaction with respect to the reactant and product respectively. Although there is an infinite variety of rate laws possible, three simple reaction orders are commonly taught: zeroth, first, and second order (*k* is the rate constant).

Zeroth order reaction is given by $-d[A]/dt = k[A]^0 = k$

First order reaction is given by $[A] = -kt + [A]^1$

Second order reaction is given by $-d[A]/dt = k[A]^2$

The integrated form is $1/[A] = kt + 1/[A]_0$

In our case, we obtain zero-order kinetics for high concentrations of the catalyst, where the encounter with specific catalytic particles is not required and where the reaction speed only depends on the available surface that scales linearly with the concentration. For lower concentration rates of the catalyst, we observe first order kinetics, as expected.

Combination of zero and first order:

According to Michaelis Menten kinetics, high aqueous concentrations increase the rate of the reaction changing the reaction from first order kinetics to zero order kinetics. The rate constant of the combination of a first-order and a zero-order reaction can be estimated according to Eq. 22 [81]:

$$k = \frac{[A_0]k_0}{[A_0] + k_{1/2}} \quad (22)$$

where $[A_0]$ is the initial concentration of the pollutant, k_0 and $k_{1/2}$ are the rate constants of zero order and half max of first order reaction [77].

1.7. Efficiency indicator – degradation rate

The efficiency of the catalytic process determines the performance of the catalyst against a pollutant. According to the available literature, for our case, the efficiency of a catalytic degradation process is calculated as the degradation efficiency of the nanomaterial against the targeted pollutant. The degradation percentage is calculated by Eq. 23.

$$\text{Degradation percentage} = \left(\frac{A_0 - A}{A_0} \right) \times 100 \quad (23)$$

where A and A_0 correspond to the initial concentration of the pollutant ($t=0$) and concentration of the pollutant at time ' t '. It represents the relative degradation of the pollutant from $t=0$ to at time ' t '. As indicated earlier, the degradation rate itself is an incomplete indicator of efficiency as it does not take into account how much catalyst was used and how much energy was eventually converted. We will however use it here for the sake of simplicity.

To compare the catalytic efficiency of different catalysts: (i) Degradation efficiency over time: the degradation efficiency of a catalytic process obviously increases with time, making it an unsuitable parameter to compare two different processes in catalysis. (ii) Catalyst concentration: the higher the concentration of the catalyst, the higher the degradation efficiency, which increase the reactive surface area of catalyst, this makes it essential to standardize reactive surface area when comparing different catalysts. (iii) Effect of pH on catalytic efficiency: the change in the pH of the reaction can increase or inhibit the efficiency of the catalyst against pollutants. On the other hand, the rate of the reaction represents the degradation of molecules per minute (unit min^{-1}). Here, the rate of the reaction is one of the most common parameters to compare different materials. In other words, degradation efficiency allows for a convenient comparison of experiments with similar parameters, but it does not allow for a quantification of the reaction efficiency. The energy conversion efficiency would be a much more universal option. However, throughout the literature, it appears as if researchers prefer to report conversion efficiencies above 90% over a certain

number of hours (which varies from article to article) or rather arbitrary target concentrations and other parameters like pH etc., rather than the actual value of the energy conversion of their reaction. This value would likely be very low, as outlined above, but at least it would raise the right questions about why it is so low.

1.8. Perspective of nanomaterial on catalysis

According to the literature, to boost the catalytic activity of a nanomaterial, researchers vary the pH of the reaction mixture and/or engineer the nanomaterial (doping, heterojunction, etc.) by modifying the absorption bands of the nanomaterial [82-84]. The physics behind photovoltaics and photo-catalysis is similar, which is indeed very helpful. Photovoltaics deals with the electronic excitation of nanomaterial and the transfer of the generated photoexciton to the external circuit resulting in the conversion of solar energy to electrical energy, whereas photocatalysis is the conversion of solar energy to chemical energy. The main rate limiting step for the latter is the mass transportation of the charge carriers from the surface of the nanomaterial to pollutant for the mineralization of toxic pollutant. Developing better mass transfer rather than changing the physical properties of the nanomaterial seems to be the method of choice to provide progress to the field.

Further, the photocatalysis on mineralization of different pollutants (various organic dye) does not require different nanomaterials. Rather developing a highly reactive catalytic surface which is efficient for the mass transportation of charges can be used for water treatment. The band alignment of the catalyst needs to be higher than NHE redox potentials of the conversion of e^-/h^+ pair to their corresponding radicals is the basic criteria on the mineralization of the pollutants i.e. the standard potential for the oxidation and reduction under irradiation with respect to the normal hydrogen electrode (NHE) which is 1.99 eV for the conversion of OH^- to $\bullet OH$ and -0.33 eV for the conversion of O_2 to $\bullet O_2^-$. So, one catalyst with sufficient capability to trigger these reactions should be able to break down a large number of possible pollutants. In catalysts, which possess higher CB (lower than -0.33 eV) the excited e^- reacts with the adsorbed oxygen in water to generate a super oxide radical and catalysts which possess a VB higher than 1.99 eV enable the effective conversion of water or hydroxyl ion to hydroxy radical.

Future application of the highly reactive catalytic surface can also be applied for photocatalytic water splitting, where we could produce hydrogen gas, which is a not a greenhouse gas and hence it may have a positive impact on climate change by reducing the consumption of fossil fuel. The potential difference between the working electrode and counter electrode needs to be higher than 1.23 V, the conduction band and valance band must be sufficiently high negative and high positive respectively for oxidation and reduction to permit water splitting.

In addition, the real time application of the nano-photocatalysis has its own advantage for a cost effective way for water treatment rather than osmosis. It also has limitations such as the penetration depth of light to activate the nanomaterial on the bottom of the reactor and the separation of nanomaterial after catalysis. Even though the catalyst is stable for several consecutive cycles to retreat the water, the nanomaterial from the reactor needs to be separated before consumption. The nanomaterial can be separated by filtration and ultra-high centrifugation but as previously stated, these activities belong to a different field of research.

1.9. Methyl orange as a model pollutant

In the present study, methyl orange (MO, $C_{14}H_{14}NaO_3S$) was used as a model pollutant against a catalyst to determine the catalytic properties of the material. Methyl orange is one of the most stable azo dyes (azo functional group $-N=N-$ linking aromatic ring) with an absorption maximum of 464 nm. Methyl orange is a synthetic azo dye, which is widely used as a pH indicator by colorimetric assay (acidity - change in the colour from orange to red-orange; basicity - change in the colour from orange to yellow). In our case, it occurs as a sodium salt, forming ionic species upon dissolution.

According to literature, methyl orange is used as a model pollutant to determine the catalytic activity of the nanomaterial by colorimetric assay or spectrophotometric assay [85]. Determination of the broken bonds in the azo functional group of methyl orange is straight forward through the loss in the absorption spectrum of methyl orange. As such, it also provides the platform to test the catalytic activity of a nanomaterial to treat the contaminant in the environmental water bodies by using a renewable green energy source.

It should be said that the use of optical absorption spectroscopy to determine the concentration of the dye molecule, and as a consequence to determine reaction rates of photocatalysis has two implications. The change of absorption depends exponentially on the concentration of the dye molecule, so the method is highly sensitive to small changes. On the other side, large changes of concentration between the beginning and the end of the experiment may cause absorption changes of the solution that are too large to be detected. The limitation comes from the dynamic range of detectors that are only able to measure a certain range of transmitted intensities.

1.10. Nanomaterial as a catalyst

Nanomaterials derive their characteristics from bulk materials initially, but these characteristics can be significantly influenced by finite size effects, primarily due to a considerable change in the surface-to-volume ratio at the nanoscale [43, 86]. The tunable properties of the nanomaterial (size, surface area, defect, band energy, light harvesting) offer the opportunity to create toolboxes based on certain nanomaterials to e.g. develop a system for environmental treatment by

advanced oxidation process. In the present work, the catalytic activity of surface engineered SrTiO₃ (TiO₂ terminated and SrO terminated) was studied to compare the efficiency with TiO₂ (standard photocatalyst) and the influence of the concentration of TiO₂ on tribo-catalysis.

1.11. SrTiO₃ nanoparticles

Strontium titanate is certainly one of the best known and most investigated oxide materials. The electronic properties range from insulator to superconductor with T_C around 300 mK upon niobium doping. In the early years, Ohtomo and Hwang [87] dominated the discussion about the existence of the 2D transport (LaAlO₃/SrTiO₃) and the intensive properties of the conductivity between the two insulators. Various groups emphasised the use of semiconductor heterojunctions to use it for wide range of application [88]. It also paved the way to study the properties of the semiconductor nanomaterials like SrTiO₃, Al₂O₃, ZnO, BaTiO₃, etc. SrTiO₃ is an idealized cubic crystal structure of space group symmetry Pm3m with the lattice parameter a = 0.3905 nm (Fig. 9a). Generally, perovskites (ABO₃) may undergo deformation under stress or change in temperature and the most relevant phase transitions from the cubic phase are as follow:

- (1) Ferroelectric (FE) – the polar displacement of the anion and cation, results in the spontaneous polarization (Fig. 9b). This instability occurs in barium titanate, not so in strontium titanate.
- (2) Antiferrodistortive (AFD) rotation – it represents the antiphase rotation of the oxygen which occurs in the TiO₆ octahedra phase (Fig. 9c). This is indeed observed in SrTiO₃ at 105 K.

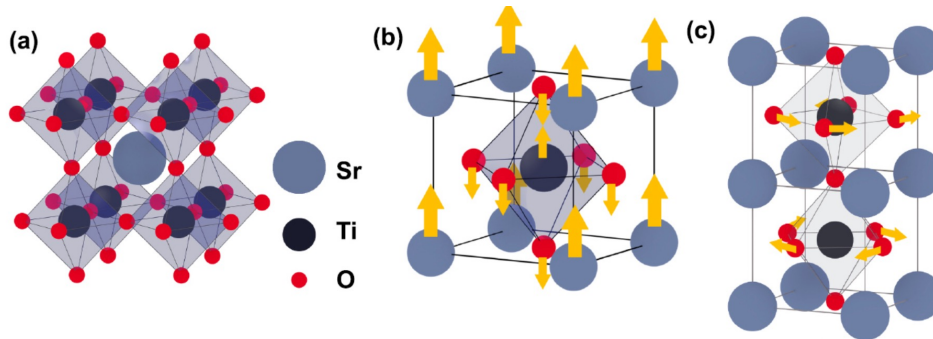


Figure 9. Phase transitions of SrTiO₃. (a) The crystal structure of SrTiO₃, (b) Ferroelectric displacement. (c) Antiferrodistortive rotation.

Whether or not a material of ABO₃ composition crystallizes as a perovskite can be determined by the Goldschmidt tolerance factor which is given by Eq. 24.

$$t = \frac{r_A + r_o}{\sqrt{2}(r_B + r_o)} \quad (24)$$

where r_A , r_B , r_o represents the ionic radii of the anion, cation and oxygen respectively, t represents the tolerance factor [89]. The Goldschmidt tolerance (t) for $BaTiO_3$ is 1.063 ($t > 1$) which shows that $BaTiO_3$ is a ferroelectric material, while the Goldschmidt tolerance for $CaTiO_3$ is 0.946 ($t < 1$) which shows that it has the antiferrodistortive rotation, and the Goldschmidt tolerance for $SrTiO_3$ is unity ($t = 1$) at room temperature, showing that it has almost equal tendency to undergo a ferroelectric phase transition, while it also undergoes the antiferrodistortive transformation at 105K [90]. However, whether they cooperate or compete with each other is still subject of debate. In the present work, the surface engineered $SrTiO_3$ (TiO_2 termination and SrO termination) were synthesised by the post treatment of $SrTiO_3$ (annealing and etching).

1.12. Geometry and structural attributes of $SrTiO_3$

Single crystalline $SrTiO_3$ may be described as a sequence of alternating layers of SrO and TiO_2 along the (100) direction to form a cubic crystal structure. The (100) surfaces of a $SrTiO_3$ single crystalline nanoparticle may therefore be (i) a combination of both SrO and TiO_2 termination, (ii) a SrO surface, or a (iii) TiO_2 surface. The surface composition of the nanoparticle is expected to have an impact on chemical behaviour, and the surface characteristics have their own distinct properties [91, 92].

Catalysis is a surface phenomenon: Surface engineering is expected to provide tunability of the catalytic property of the nanomaterial. It also acts as an indirect tool to determine the surface composition of the $SrTiO_3$ as to whether it is TiO_2 terminated or SrO terminated. Surface engineering the $SrTiO_3$ does not affect the band energy of the $SrTiO_3$ [93], the first limiting step in catalysis, which is the light harvesting, photooxidation and photoreduction for the formation of reactive oxygen species (ROS). The nanomaterial with a band structure suitably aligned with respect to the NHE redox potentials on the conversion of e^-/h^+ pair to their corresponding radicals (superoxide or hydroxyl) is the basic criteria for the mineralization of the pollutants i.e. the standard potential for the oxidation and reduction under irradiation corresponding to the normal hydrogen electrode (NHE) is 1.99 eV for the conversion of OH^- to $\bullet OH$ and -0.33 eV for the conversion of O_2 to $\bullet O^{2-}$. According to the available literature, the direct band gap energy of $SrTiO_3$ nanoparticles ranges from 3 to 3.2 eV. The CB and VB of $SrTiO_3$ were calculated to be 2.45 eV and -0.79 eV, which is higher than 1.99 eV and -0.33 eV showing the potential for effective formation of $\bullet OH$ and $\bullet O^{2-}$ for the mineralization of toxic pollutant (Fig. 10).

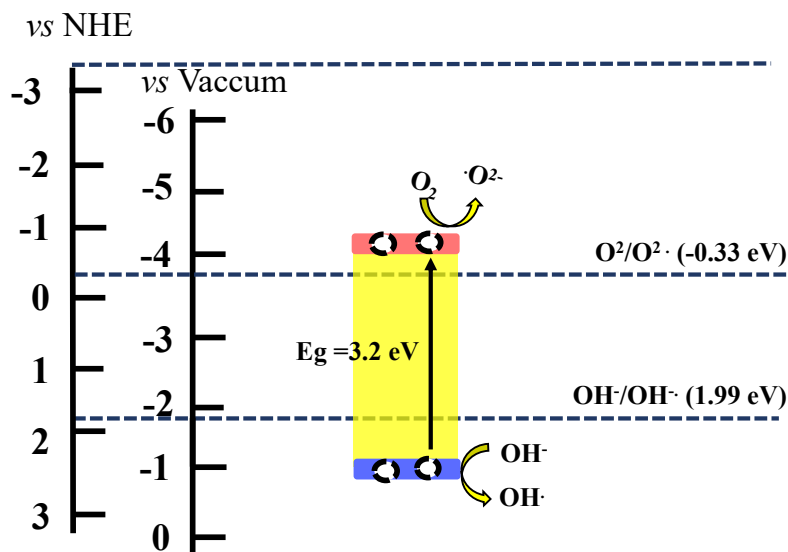


Figure 10. Band diagram of SrTiO₃ against redox potentials of radical formation.

1.13. Application of SrTiO₃ on catalysis

According to literature, to improve the light absorption and to engineer the band energy of SrTiO₃ nanoparticles, doping effect have been studied (doped by Cr, La, Ce, Mn). They reported that doping increased the light absorption and thereby increases the catalytic efficiency for water treatment [94, 95]. In addition, few researchers studied the formation of heterojunctions to utilize the visible light band by combining SrTiO₃ with visible band nanoparticles such as ZnO, NaTaO₃, Ag₃PO₄ etc. [96], which improve the charge separation and reduce electron-hole recombination, thereby increasing photocatalytic efficiency. These composites are effective in degrading various organic pollutants in wastewater as well as in water splitting. Further to tune the band energy of the SrTiO₃, metal defects and oxygen defect were developed in the previous literature to enhance the catalytic activity of SrTiO₃ [94, 95].

J. Qiao et al., studied the SrTiO₃ based heterojunction on sonocatalytic degradation of tetracycline. They have reported that the introduction of ultrasound on the reaction mixture activated the nanoparticle for the conversion of O₂ to [·]O₂⁻ and OH⁻ to [·]OH for the mineralization of pollutant for water treatment.

In the present work, the surface engineering of SrTiO₃ was developed without changing the band energy of the material. As photocatalysis is a surface phenomenon, the fabrication of highly active surface to improve the mass transportation is an important requirement.

1.14. Objective

1. Develop and optimize the synthesis methodology to produce the different terminations of SrTiO_3 .
2. Investigate the impact of the surface termination of SrTiO_3 for the catalytic application on water treatment.
 - Analyze the catalytic performance of the different surface terminated SrTiO_3 nanoparticles.
 - Determine the catalytic active surface and their catalytic mechanisms.
3. Investigate combination of sono- and photocatalytic processes to determine if they improve the efficiency of the nanomaterial.
4. Determine the rate-limiting step in catalysis.
 - Role of sonification in the catalytic process (sono-, or tribo-, or piezocatalysis).

2 EXPERIMENTAL TECHNIQUES

2.1. X-ray diffraction

Generally, X-ray diffraction (XRD) is the most basic characterization tool to determine the atomic spacing and crystallographic structure of the catalyst. XRD is the most common analytical technique to determine the crystallinity as well as the lattice parameter which is obtained by the fact that the X-ray wavelength dimension is typically in the same range as the interatomic spacing of the crystal. Bruker D8 Advance X-ray diffractometer with Cu-K α radiation was used in this study. The X-ray spectrometer has a cathode ray tube followed by a filter to obtain a monochromatic beam, which is then followed by the collimator and detector to detect the signals (Fig. 11a). A goniometer in the spectrometer was used to maintain the incident angle of the beam and the angle of rotation of the sample, as generally, we measure the intensity of the beam scattered versus the angle which depends on the interatomic spacing. The scattering of the X-ray beam follows the Thomson scattering model [97]. The intensity of Thomson scattering of mass (m) and charge (q) is given by Eq. 25-27.

$$I_0 = I_e \left(\frac{q^4}{m^2 c^4} \right) \frac{1 + \cos^2 2\theta}{2} \quad (25)$$

$$I_0 = I_e 7.94 \times 10^{-26} \frac{1 + \cos^2 2\theta}{2} \quad (26)$$

$$I_0 = I_e f \quad (27)$$

The detector measures angle (2θ) versus intensity which appears as the Fourier transformation of the electronic density of the material. Fourier transformation of the electronic density of the crystal as intensity is produced by the constructive interference of the x-ray wave after scattering which must satisfy the Bragg's law (Fig. 11b) [98]. Bragg's law states that for constructive interference, the path difference between the incident and emergent X-ray beams must be an integral multiple of the wavelength of the X-ray which is given by Eq. 28.

$$n\lambda = 2d_{hkl} \sin\theta \quad (28)$$

where n corresponds to the order of reflection, λ corresponds to wavelength of the X-ray beam, d_{hkl} corresponds to the interatomic distance of the crystal (provided by the Miller indices of the material) and θ corresponds to the diffraction angle.

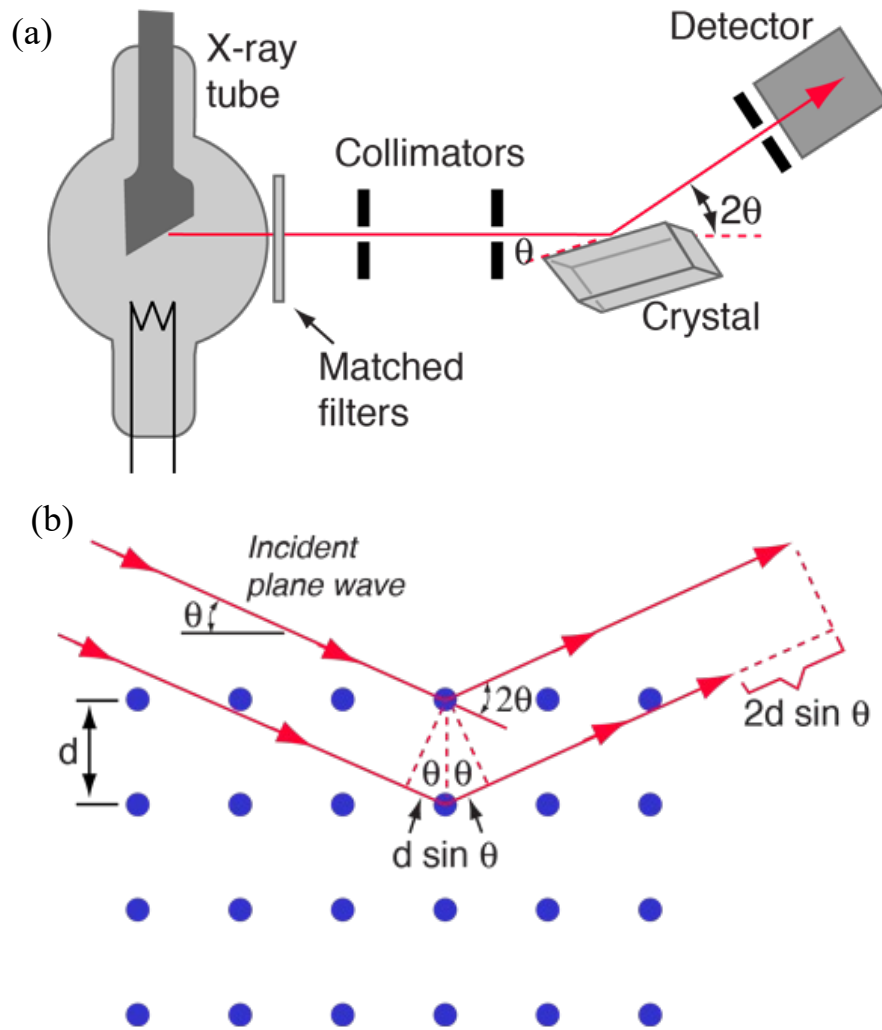


Figure 11. (a) Schematic representation of major components of an x-ray diffractometer, (b) diffraction of monochromatic x-rays on atomic planes of a material [99].

2.2. Raman spectroscopy

Raman spectroscopy is used to determine the optical properties of nanomaterial, which is generally non-destructive. It follows the Raman effect on the inelastic scattering of light interacting with the different vibrational energies of the material, as Stokes (energy towards the formation of a phonon) and anti-Stokes (annihilation of a phonon). We can only perform a qualitative analysis of the material using Raman spectroscopy since a quantitative analysis by Raman spectroscopy by comparing the intensity of the scattered light depends upon the sample cross-section [100, 101].

The major components in the typical Raman spectroscopy were:

- (i) Monochromatic high power light source

- (ii) Sample holder (mounting and irradiation)
- (iii) CCD detector (spectrophotometer)

The schematic illustration of the Raman effect is given in Fig. 12. Generally, a high power single-mode laser is used as illumination source for scattering after interaction. Firstly, the material is excited after illumination by the laser and the scattered light is collected back to the lens. Then it is transmitted to the notch filter (band stop) to cut off the Rayleigh light without affecting the scattered Raman light (Stokes in most cases) and transmitted towards the detector (spectrophotometer). The transmitted light is then passed through the grating to the CCD detector. The intensity of the Raman scattering is inversely proportional to the fourth power of the wavelength (Eq. 29 and 30).

$$I_s \propto I_0(\omega_0 - \omega_R)^4 \left[\left(\frac{\partial \alpha}{\partial k} \right)_{k=0} \right]^2 \quad (29)$$

$$I_s \propto \lambda^{-4} \quad (30)$$

Here, I_s represents intensity of the scattered signal, I_0 represents intensity of the incident signal, ω_0 represents frequency of the incident signal and ω_R represents frequency of the scattered signal. The CCD detector will then convert the optical signal to the charge proportional to the intensity of the signal impinging. In the present study, the Raman measurements were performed by using Horiba iHR320 with thermoelectrically cooled Scientific Synapse Back-Illuminated Deep Depletion CCD detector. The excitation source is a 473 nm solid-state blue Cobolt 04-01 laser (linearly polarized, TEM00).

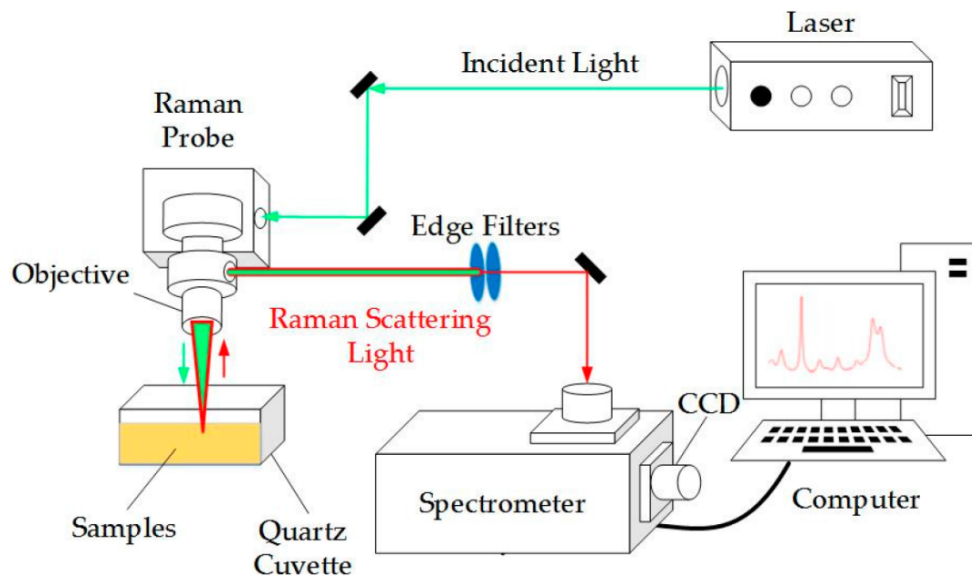


Figure 12. Schematic illustration of Raman spectroscopy and major components of a Raman Spectrometer [102].

2.2.1. Working principle

Generally, the illumination of materials by high-power monochromatic lasers induces an electric polarization or electric dipole in the material. The electric dipole moment scales linearly with the electric polarization with the applied electric field (Eqs. 31 and 32)

$$E = E_0 \cos(\omega_0 t) \quad (31)$$

$$P = \alpha E \quad (32)$$

where α is defined as the polarizability of the medium, E is defined as the instantaneous electric field strength at time 't', E_0 is defined as the maximum amplitude of the electric field, ω_0 is defined as the angular frequency of the wave, which is related to the frequency f by $\omega_0 = 2\pi f$ and t is time. The relative displacement, k , of the material is given by (Eq. 33),

$$k = k_0 \cos(\omega_R t) \quad (33)$$

According to Taylor series expansion the polarizability of the material can be expressed in terms of k , as (Eq. 34-37).

$$\alpha = \alpha_0 + \sum \left(\frac{\partial \alpha}{\partial k} \right)_{k=0} k + \frac{1}{2} \sum \left(\frac{\partial^2 \alpha}{\partial k^2} \right)_{k=0} k^2 + \dots \dots \quad (34)$$

$$\alpha = \alpha_0 + \sum \left(\frac{\partial \alpha}{\partial k} \right)_{k=0} k + \frac{1}{2} \sum \left(\frac{\partial^2 \alpha}{\partial k^2} \right)_{k=0} k^2 + \dots \dots \quad (35)$$

As $P = \alpha E$

$$p = \left[\alpha_0 + \sum \left(\frac{\partial \alpha}{\partial k} \right)_{k=0} k + \frac{1}{2} \sum \left(\frac{\partial^2 \alpha}{\partial k^2} \right)_{k=0} k^2 + \dots \right] \times E_0 \cos(\omega_0 t) \quad (36)$$

Assuming $\Rightarrow \cos A \times \cos B = \frac{1}{2} \{ \cos(A - B) + \cos(A + B) \}$

$$P = \alpha_0 E_0 \cos(\omega_0 t) + \frac{1}{2} \sum \left(\frac{\partial^2 \alpha}{\partial k^2} \right)_{k=0} k_0 E_0 \cos(\omega_0 t - \omega_R t) + \frac{1}{2} \sum \left(\frac{\partial^2 \alpha}{\partial k^2} \right)_{k=0} k_0 E_0 \cos(\omega_0 t + \omega_R t) \quad (37)$$

According to the above equation the first, second and third represents the Rayleigh, Stokes and anti-Stokes respectively, where ω_R corresponds to the frequency of the phonons.

2.2.2. Modes of vibration

Lattice vibrations or phonons are an essential way to determine the type of scattering such as Raman or Brillouin (Fig. 13). The type of vibration of in a crystal is mainly based on the crystal structure, symmetry and occupation number. In terms of phonon vibrations, it is further branched into two: (i) Acoustic and (ii) Optical phonons (Fig. 14) [103].

(i) Acoustic phonon - The mode vibration with low energy $\sim \frac{K_B T}{n(\omega)}$ where $n(\omega)$ represents number density function, K_b represents Boltzmann constant and T represent temperature ($k \rightarrow 0$, zero energy on $k=0$). The vibration corresponds to neighboring atoms which are in phase. If the

displacement is in the direction of wave propagation, then it is longitudinal (denoted as LA), if the displacement is in the perpendicular direction then it is transverse, denoted as TA .

(ii) Optical phonon - The mode of vibration possesses sustainable energy as $k \rightarrow 0$ the vibration is mainly based on the atoms or ions, which are out of phase. If the displacement is in the direction of wave propagation, then it is longitudinal (denoted as LO), if the displacement is in the perpendicular direction then it is transverse, denoted as TO.

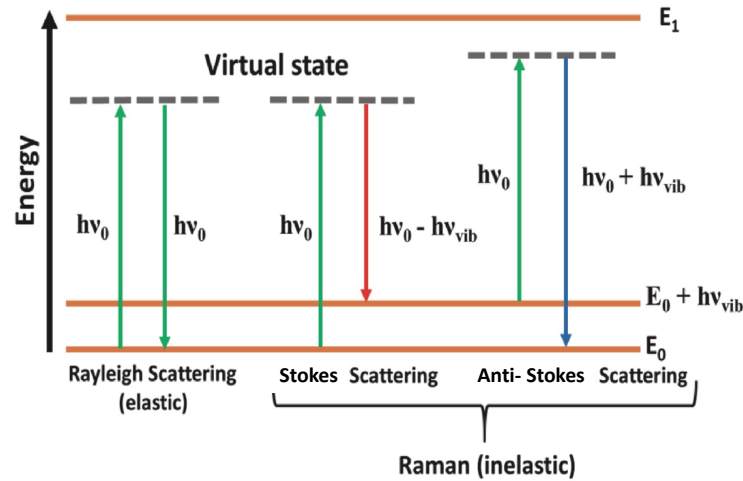


Figure 13. Different light scattering processes (a) Rayleigh, (b) Stokes and (c) Anti-Srokes [104].

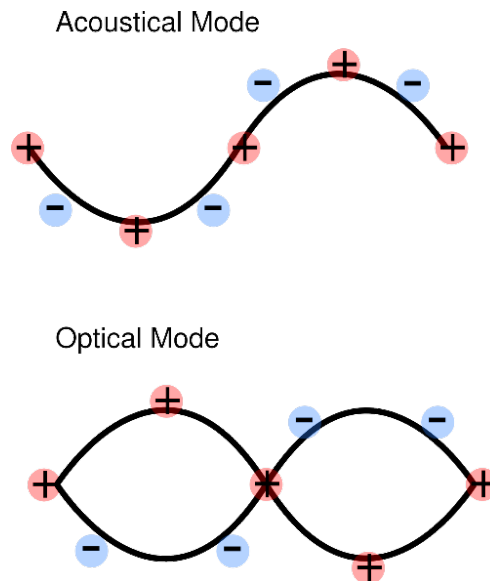


Figure 14. Different phonon modes (acoustic phonon and optical phonon).

2.3. Transmission electron microscopy

Transmission electron microscopy (TEM) is an imaging technique used to determine the grain boundaries, diffraction pattern, structure, and dislocations in the material. It can easily be altered into an electron diffraction technique that uses a highly energetic electron beam to determine the morphological characteristics of a crystal [105]. Optical microscopes have different wavelengths in the range of 400 to 800 nm, whereas the wavelength of the electron beam microscopic technique would be ~ 0.004 nm for an electron energy of $V_a = 100$ keV. The wavelength of TEMs is far less than the typical distance between the atoms, the wavelength can be adjusted by the accelerating voltage. The characteristics of the TEM technique (short wavelength and high-resolution spatial arrangement) paved the way to determine the properties of crystals at the atomic scale. The major components in TEM are (i) electron gun, (ii) illumination system, (iii) imaging system and (iv) viewing chamber (Fig. 15).

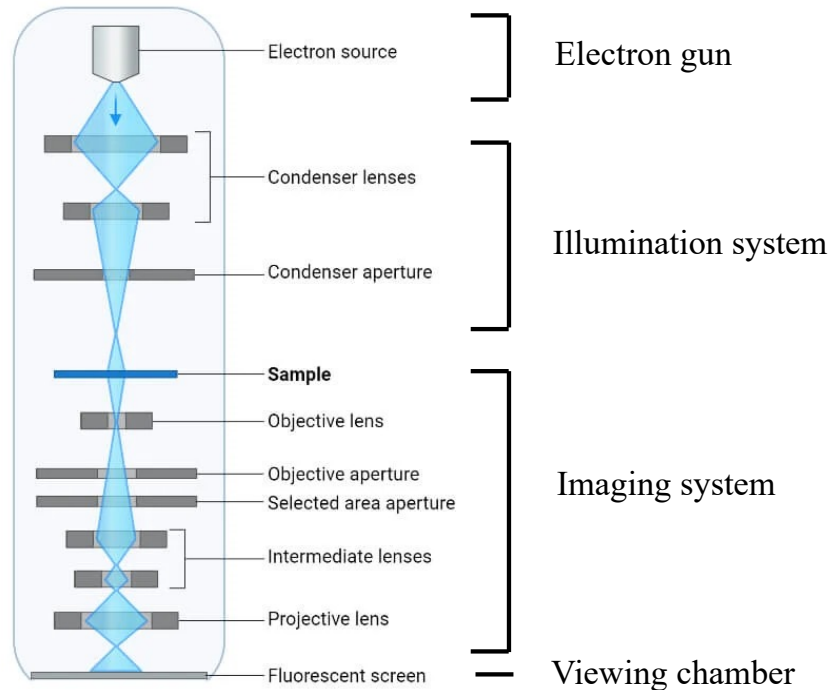


Figure 15. Major components of a typical transmission electron microscope [106].

The electron emission from the electron gun is a thermionic emission, where the hot cathode is heated to produce the energetic stream of electrons. The electron emission of the system at INRS is based on Richardson's law [107] (Eq. 38)

$$J \propto T^2 \exp\left(\frac{-\phi}{k_B T}\right) \quad (38)$$

where K_B , T , J and Φ represent the Boltzmann constant, temperature, current density, and work function of the cathode material respectively. The electron beam then passes through the illumination system, which comprises of lenses and is then directed towards the imaging system after hitting the sample. The electrons scattered from the sample are focused on the objective lenses, the electron scattering is mainly based on the thickness of the sample. The scattered electron beam is then focused on the 2D viewing chamber. The major advantage of the electron scattering technique is the electron diffraction pattern after scattering correlation referred to as selective area electron diffraction (SAED), which gives the information on the atomic arrangement in the crystal with spatial resolution. In the present study, the TEM was performed by using JOEL-JEM-2100F with 200 kV to determine the size and shape of the nanomaterial.

2.4. X-ray photoelectron spectroscopy

X-ray photoelectron spectroscopy (XPS) is a photoelectric effect technique to determine the elemental composition based on the kinetic energy of the ejected photoelectrons. XPS is a surface phenomenon where it determines the surface characteristics of the material (penetration depth of a few nanometers < 10 nm), targets like Al-K α (1486.6 eV) or Mg-K α (1253.6 eV) are used as the source for X-rays which depends on the configuration of the instrument [108]. The XPS using the photoelectric effect, measures the binding energy (BE). The quantitative measurement of BE is determined by Eq. 39 and 40.

$$BE = h(\nu - \nu_0) - \frac{mv^2}{2} \quad (39)$$

$$BE = h\nu - \phi - KE \quad (40)$$

where KE , $h\nu$ and $h\nu_0$ (ϕ) correspond to the kinetic energy, photon energy, and work function respectively (Planck's constant, $h = 6.624 \times 10^{-34}$ Js). Firstly, X-ray irradiation ejects a core electron by electronic collision and leaves an empty space in the inner shell of the atom. Next, a high energy level electron loses its energy to move towards the space left by the ejected electron. Post-photoemission, relaxation of the ions or instability of the atom results in the ejection of an Auger electron (Fig. 16). The ejected electron is counted by the electron analyzer in the XPS, which is an inelastic loss of the electron. In the present study, the XPS spectra of nanomaterial is performed by using VG Escalab 220i XL with a monochromatic Al-K α source.

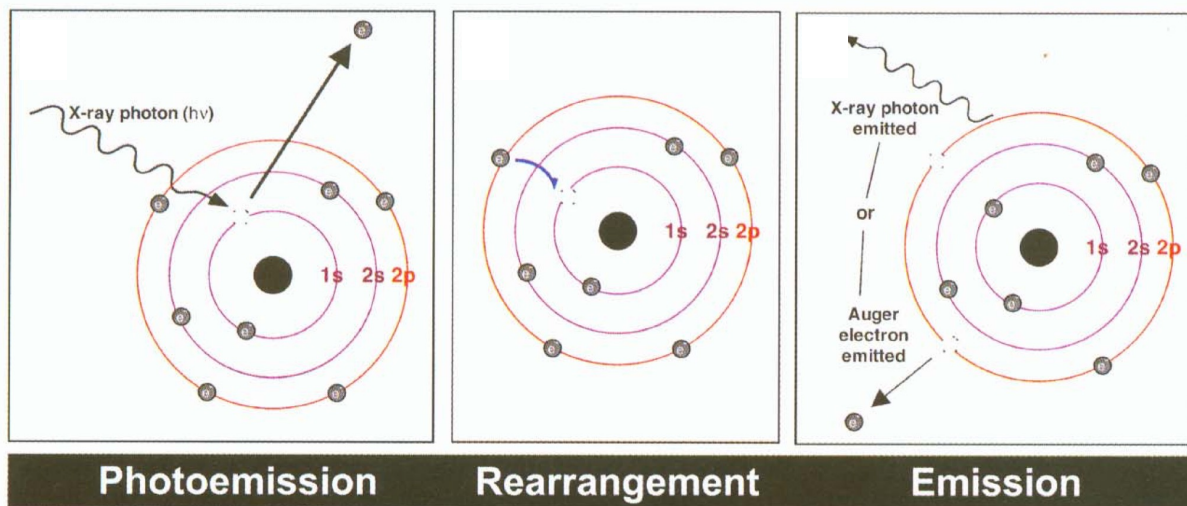


Figure 16. Schematic representation of the mechanism of photoemission leading to both Auger and photoelectrons in x-ray photoelectron spectroscopy [109].

2.5. Optical absorption (UV-VIS-NIR) spectroscopy

UV-vis-NIR spectroscopy offers an avenue to study the optical properties of the material by scattering, reflection, absorption, and transmittance on solid or liquid phase samples. In general, when the material is irradiated, the material may undergo electronic transition, which is mainly based on the intrinsic optical properties of the material [110]. The optical spectroscopic technique determines the difference in the incident intensity and intensity of the light after the interaction with the material (I_0-I), which follows the Lambert-Beer law (Eq. 41) for the case of absorption.

$$A = \epsilon l C \quad (41)$$

where A , ϵ , l and C correspond to the absorbance, molar absorptivity, path length and concentration of the solution. The components of the optical spectroscope are (i) light source, (ii) filter wheel, (iii) monochromator, (iv) sample and (v) detector (Fig. 17). Firstly, the light source of the spectrometer varies depending upon the configuration, where Deuterium lamp is used for UV light (200 to 400 nm) and Tungsten lamp for visible and IR (350 to 2500 nm). It passes through the filter wheel to filter the spectral ranges (UV, visible and IR region) and the hits the monochromator (fine grating) followed by a beam splitter. Then after, the beam passes through the sample and the integrating sphere accessory can be incorporated to collect the diffused light. In the present study, the UV-vis-IR spectroscopy of the nanomaterial sample was performed using PerkinElmer, Lambda 750.

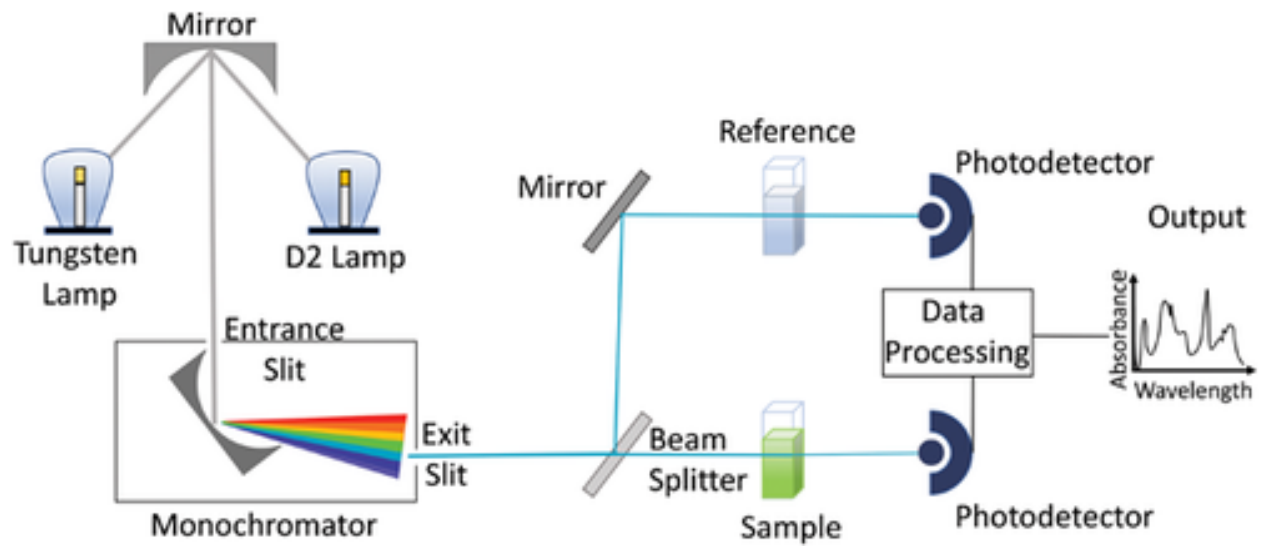


Figure 17. Schematic representation of components of UV-VIS-NIR spectrophotometer [111].

3 MATERIALS AND METHODS

3.1. Microwave assisted hydrothermal synthesis

In the present work, the SrTiO₃ nanoparticles were synthesised by a microwave hydrothermal method (using Padinox MWO021, 2.5 2.5 GHz). Unlike high temperature solid-solid diffusion, hydrothermal reaction is based on the mass transfer in the solution phase [112, 113]. The conventional hydrothermal approach is a single step process where the anionic and cationic precursors in the solution are elevated to high temperature (100 °C) with high pressure (up to 0.1 MPa). The hydrothermal reaction is based on the bottom-up method for the synthesis of nanoparticles. Despite the advantages of the hydrothermal method compared to the solid-solid diffusion, the major challenge of the conventional hydrothermal method is to synthesize single-phase nanoparticles, as the property of the nanoparticle depends on the phase of the nanomaterial. The phase of the nanomaterial on synthesis can be affected by several parameters. Here, the microwave hydrothermal method uses an in-situ microwave which helps to generate high pressure and temperature for nucleation. In comparison with the conventional hydrothermal method, the microwave hydrothermal method is (i) cost-effective, (ii) economic, (iii) reproducible, (iii) provides accelerated nucleation, (iv) energy-efficient and (v) faster [114]. Nevertheless, it has disadvantages like precisely controlling the parameters is difficult, studying the growth phase is infeasible, and the temperature and pressure are not directly accessible. The mechanism of the microwave hydrothermal method is the use of 2.5 GHz (penetration depth -12.23 cm) microwave, which is based on the ionic conductivity of the interaction of dielectric material with the solid, liquid or both the phases and thus, results in the effective formation of single-phase nanoparticles. Another limitation of the microwave assisted hydrothermal approach is that the reactor size is limited to the typical cavity size of a microwave reactor, while conventional hydrothermal approaches may be scaled up to very large volumes.

3.2. Materials

Strontium hydroxide octahydrate (98%), titanium butoxide (98%), ammonium hydroxide (25%), isopropyl alcohol, benzoquinone, silver nitrate, ethylenediaminetetraacetic acid and titanium dioxide (P25) purchased from Sigma-Aldrich Chemicals were used for the material synthesis. Methyl orange as model pollutant, was purchased from Sigma-Aldrich Chemicals. All the chemicals were used without further purification. Meanwhile, other species referred to as unintentional doping account for $\leq 2\%$ according to specifications provided by the suppliers.

3.3. Synthesis of SrTiO₃

The microwave-hydrothermal method was employed for the chemical synthesis of SrTiO₃ nanoparticles (SrTiO₃ NPs). Firstly, 0.45 g of titanium butoxide (Ti(C₄H₉O)₄) was added to 10 mL distilled water. 2 mL of ammonium hydroxide (NH₄OH) was added to the above reaction mixture to attain a pH of 14. Finally, 0.6 g of strontium hydroxide (Sr(OH)₂) was added to the reaction mixture and then stirred at 80° C for 20 min to obtain a homogenous solution. The solution was transferred to a 23 mL Teflon container, sealed in a microwave acid digestion PTFE autoclave and the hydrothermal reaction was performed at 120W (2.5 GHz) for 7 min for the formation of SrTiO₃. The prepared NPs were collected by precipitation and then washed twice with ethanol, water and dried at 80°C for 16 h. The NPs were annealed at 1000° C for 2h, with a heating rate of 20° C/min.

The SrO termination on SrTiO₃ NPs was attained by annealing. Here, 0.2g of synthesized SrTiO₃ was annealed at 900°C for 2 h with a heating rate of 20° C/min. The TiO₂ termination on SrTiO₃ NPs was attained by hydrothermal etching. Firstly, the as prepared SrTiO₃ (0.2g) was added to 12 mL of water and the reaction mixture was transferred to a Teflon line autoclave and then transferred into a microwave acid digestion PTFE container, where the hydrothermal reaction was performed at 120W (2.5 GHz) for 7 min. Then the prepared NPs were collected by precipitation and then washed twice with ethanol, water and dried at 80°C for 16 h. The NPs were annealed at 500° C for 2h, with a heating rate of 20° C/min to obtain TiO₂ terminated SrTiO₃. The chemical equation on the synthesis is as given in Eq. 42 and 43 [115].



3.4. Photocatalytic experiment

The photocatalytic activity of SrTiO₃ (SrO terminated and TiO₂ terminated) NPs was tested against methyl orange (MO) as a model pollutant (Fig. 18). Firstly, 50 mg/L of SrTiO₃ (SrO terminated and TiO₂ terminated) NPs and 10 mg/L of methyl orange were sonicated in a water-bath for 20 min at room temperature and the reaction mixture was stirred in the dark for 30 min. Then, the reaction mixture was irradiated under light (100 mW/cm²) and the transmittance was recorded. All the experiments were performed in triplicate to determine the standard deviation, and to reduce the sources of statistical error for the sake of reproducibility.

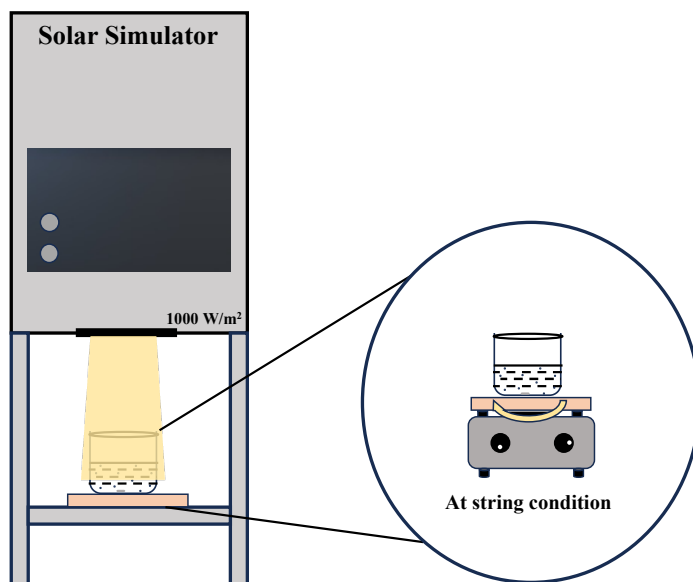
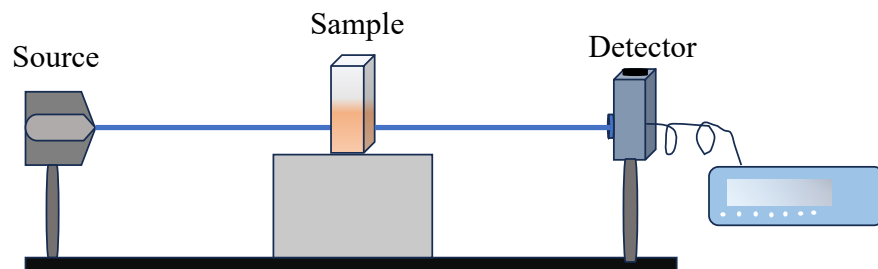


Figure 18. Photocatalytic setup to perform degradation of methyl orange.

3.5. Spectrophotometric set up to determine the optical density

The catalytic activity of the nanomaterial is quantified through the relative loss in the absorbance or increase in the transmittance on irradiation. The optical density of the reaction mixture at regular intervals of time is determined by a simple spectrophotometric setup (Fig. 19). Here, the source of the setup is a monochromatic blue laser light source (405 nm). The light from the source passes through a glass cuvette and reaches the detector to record the transmittance of the reaction mixture at time 't'. Here, the photodiode connected with the potentiometer was used as a detector to collect the transmitted light and convert it to an electrical signal. The use of monochromatic light as a source, avoids the filter wheel, grating and quartz cuvette traditionally contained in a spectrophotometer as the source and the absorption maximum of methyl orange is in visible range.

To avoid contributions from wavelength-dependent scattering of catalytic nanoparticles, the solution was first centrifuged to remove catalyst particles from the dye-solution, which results in systematically higher transmittance (now only limited by the presence of the dye) leading to better reproducibility of results.



Source - blue laser (405 nm)
 Sample – reaction mixture glass cuvette
 Detector – photodiode connected with potentiometer

Figure 19. Optical setup to measure the transmittance of the reaction mixture.

3.6. Sono-photocatalytic experiment

The combination of two catalytic process can boost the catalytic activity of the SrTiO₃ nanoparticle against the targeted pollutant (methyl orange). In the present study, the combination of photocatalysis with the use of a sonification was performed to resolve the rate-limiting step in photocatalysis, the sonification of the reaction enhances the mixing and thereby increases the mass transfer between the nanomaterial and pollutant. The exposure to sonification (between intervals of photocatalytic experiment – 10 min) is varied on a logarithmic scale: 0, 6, 18, 30, 60, 100, 300 and 600 s for every 10 min (photocatalysis) of each experiment. The intervals between sonication and photocatalysis are illustrated in Fig. 20.

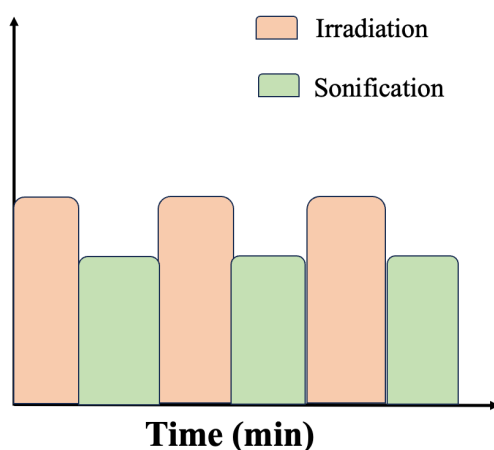


Figure 20. Graphical illustration of sonophotocatalytic experiment for alternating sonification with photocatalysis.

3.7. Characterization of samples

The surface engineering of SrO terminated or TiO₂ terminated SrTiO₃ and untreated SrTiO₃ was confirmed by XRD. XRD is also used to determine the purity and crystallinity of the prepared sample. XRD measurements were done using a Bruker D8 Advance X-Ray Diffractometer. The morphology and structure of the SrTiO₃ with different surface terminations was determined by TEM (JEOL, JEM-2100). UV-visible-NIR spectroscopy (Perkin–Elmer Lambda 750) of the SrO terminated, TiO₂ terminated SrTiO₃ and untreated SrTiO₃ is performed to compare the absorption spectra of the prepared particles. The Raman spectra were acquired using a Horiba iHR320 spectrometer incorporated with a 473 nm DPSS laser. The scattered light was detected by a thermoelectrically cooled CCD (Synapse BIDD QE). Photoluminescence spectrum was obtained using a Horiba iHR320 spectrometer incorporated with a 355 nm DPSS laser with 1200 l/mm grating. X-ray photoelectron spectroscopy was obtained on a Physical Electronics (VG Escalab 220i XL) system. A 1486.6 eV Al-K α source operating at 15 kV and 20 mA was used while the calibration was done using the ubiquitous C 1s peak positioned at 284.8 \pm 0.05.

3.8. Band structure determination

The conduction (E_{CB}) and valence band (E_{VB}) of the material can be determined by Eq. 44 and 45.

$$E_{VB} = X - E_C - \frac{1}{2}E_g \quad (44)$$

$$E_{CB} = E_{VB} - E_g \quad (45)$$

where, X is the electronegativity of the nanomaterial, E_c is the energy of a free electron, while E_g is the band gap energy of the nanomaterial. The electronegativity of the nanomaterial can be determined by the geometric mean of the electronegativities of the constituent atoms (Sr, Ti and O).

4 RESULTS AND DISCUSSION

4.1. X-ray diffraction

X-ray diffraction was performed on SrO-terminated SrTiO₃, TiO₂- terminated SrTiO₃ and untreated SrTiO₃ to determine the crystal properties of the nanoparticles (Fig. 21). The results shows that the all the samples showed peaks (2θ) at 22.7°, 32.3°, 39.9°, 46.4°, 57.7°, 67.7° and 77.1° which corresponds to the (100), (110), (111), (200), (211) and (310) crystallographic Miller indices (hkl) respectively of SrTiO₃ (JCPDS card no: 01-089-4934). The results show that all the nanoparticles are highly crystalline showing well-defined diffraction patterns corresponds to the space group of Pm-3m (cubic phase) with lattice parameter $a \sim 3.9 \text{ \AA}$ [116]. However, the peaks are not sharp and singular (as is the example of the peak at 32.3° where peak splitting is observed) as is not seen in a single crystal indicating that the SrTiO₃ nanoparticles are polycrystalline. Here, the peak at 25.1° corresponds to TiO₂ which, as expected, can only be seen in the TiO₂ terminated and untreated SrTiO₃ nanoparticles, and seems to be subsumed in the background even if it is present in the case of the SrO terminated SrTiO₃. However, XRD is not suited to determine the termination of SrTiO₃ and these observations are merely a supportive indicator of other characterizations used to conclude the nature of terminations in the prepared samples.

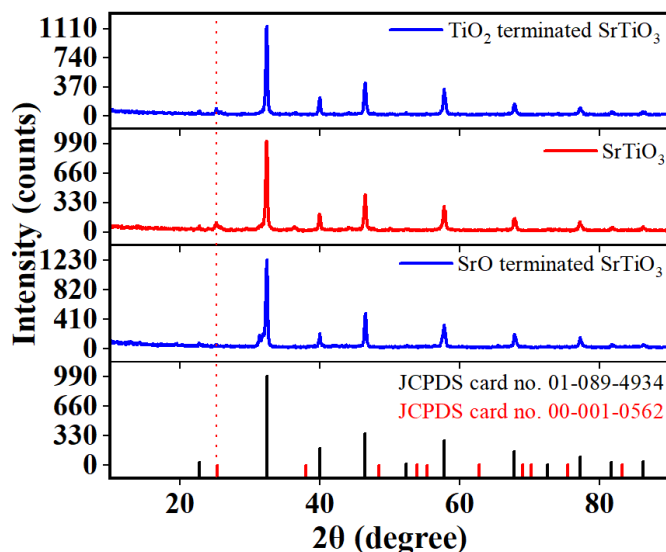


Figure 21. XRD pattern of different surface engineered SrTiO₃ (SrO- terminated and TiO₂- terminated and untreated SrTiO₃).

The average crystallite size of the nanomaterial was determined using the Scherrer equation [117] (Eq. 46)

$$D = \frac{0.9\lambda}{\beta \cos \theta} \quad (46)$$

where, D represents the crystallite size, λ represents wavelength ($\lambda = 1.54 \text{ \AA}$) and β represents the peak broadening at FWHM. The size of the SrO terminated SrTiO₃, TiO₂ terminated SrTiO₃ and untreated SrTiO₃ was calculated to be 82 nm, 79.2 and 76.2 nm respectively.

5.2. Raman spectroscopy

The Raman spectra of the surface engineered SrTiO₃ (SrO terminated and TiO₂ terminated) and untreated SrTiO₃ are shown in Fig. 22. Strontium titanate is Raman inactive for first-order modes i.e. the modes that couple one photon to one phonon [118]. The peaks in the low frequency range below 1000 wavenumbers are second order peaks, originating from the coupling of one photon to two phonons. Since they are three-particle processes, their intensities are very low. Further, the first order peak at 1052 cm⁻¹ corresponds to the presence of adsorbed carbonates, which is observed in SrO terminated SrTiO₃, and untreated SrTiO₃, whereas it is not observed in TiO₂ terminated SrTiO₃. The carbonate peak is attributed to the adsorption of carbon dioxide on SrO vicinal surfaces resulting in the formation of Sr(CO₃) [119]. This shows that hydrothermal etching removes the SrO layer resulting in the formation of TiO₂ terminated SrTiO₃.

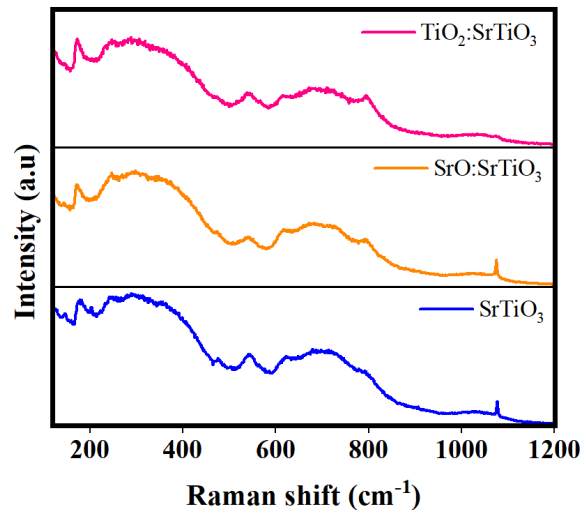


Figure 22. Raman measurements of SrTiO₃ samples.

5.3. Transmission electron microscopy

Transmission electron microscopy (TEM) measurement was performed on SrO terminated, TiO₂ terminated and untreated SrTiO₃ nanoparticles (Fig. 23). The results show that the particle size

of the SrO terminated, TiO_2 terminated and untreated SrTiO_3 is 69.8 ± 4.3 , 69.3 ± 6.8 and 71.5 ± 6.8 nm respectively, and all the three nanoparticles are cubic in shape (Fig. 24 and 25). In addition, the TEM image of the TiO_2 terminated SrTiO_3 was processed using the java software, ImageJ and shown in Fig. 25. The inverse FFT of the nanoparticle are shown in Fig. 25 b1, b2 and b3. The results show that the curves of TiO_2 and SrO layers which have the lattice parameter of 0.2 nm for each layer (from the histogram plot in Fig. 24 a3, b3 and c3), correspond to the half unit cell parameter of SrTiO_3 (~ 0.4 nm) [120]. Thus, the results confirm the formation of layers of SrO and TiO_2 for SrTiO_3 nanoparticles. TEM is suboptimal for characterizing the surface termination of the nanoparticle, further surface characterization techniques are required in conjunction to ascertain the terminations uniquely.

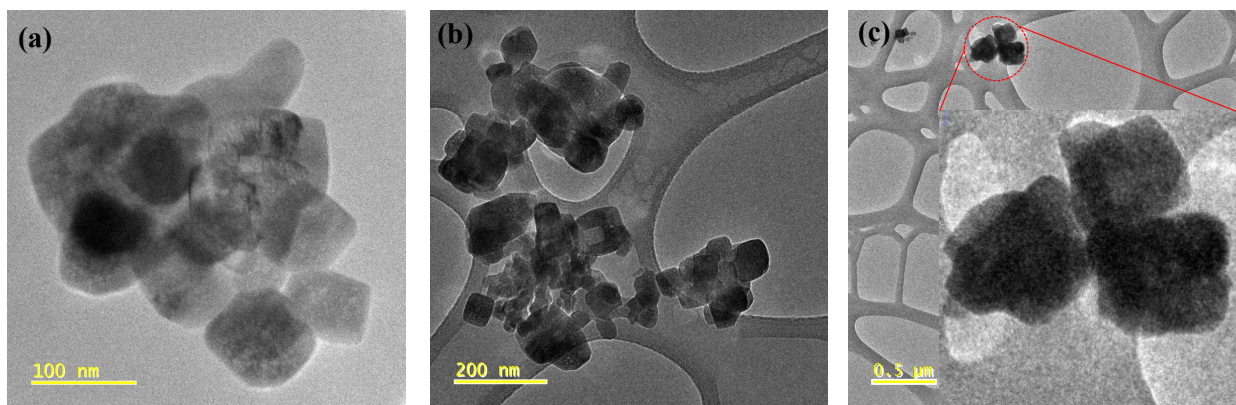


Figure 23. TEM images of TiO_2 terminated (a), SrO terminated (b) and untreated SrTiO_3 (c) nanoparticles.

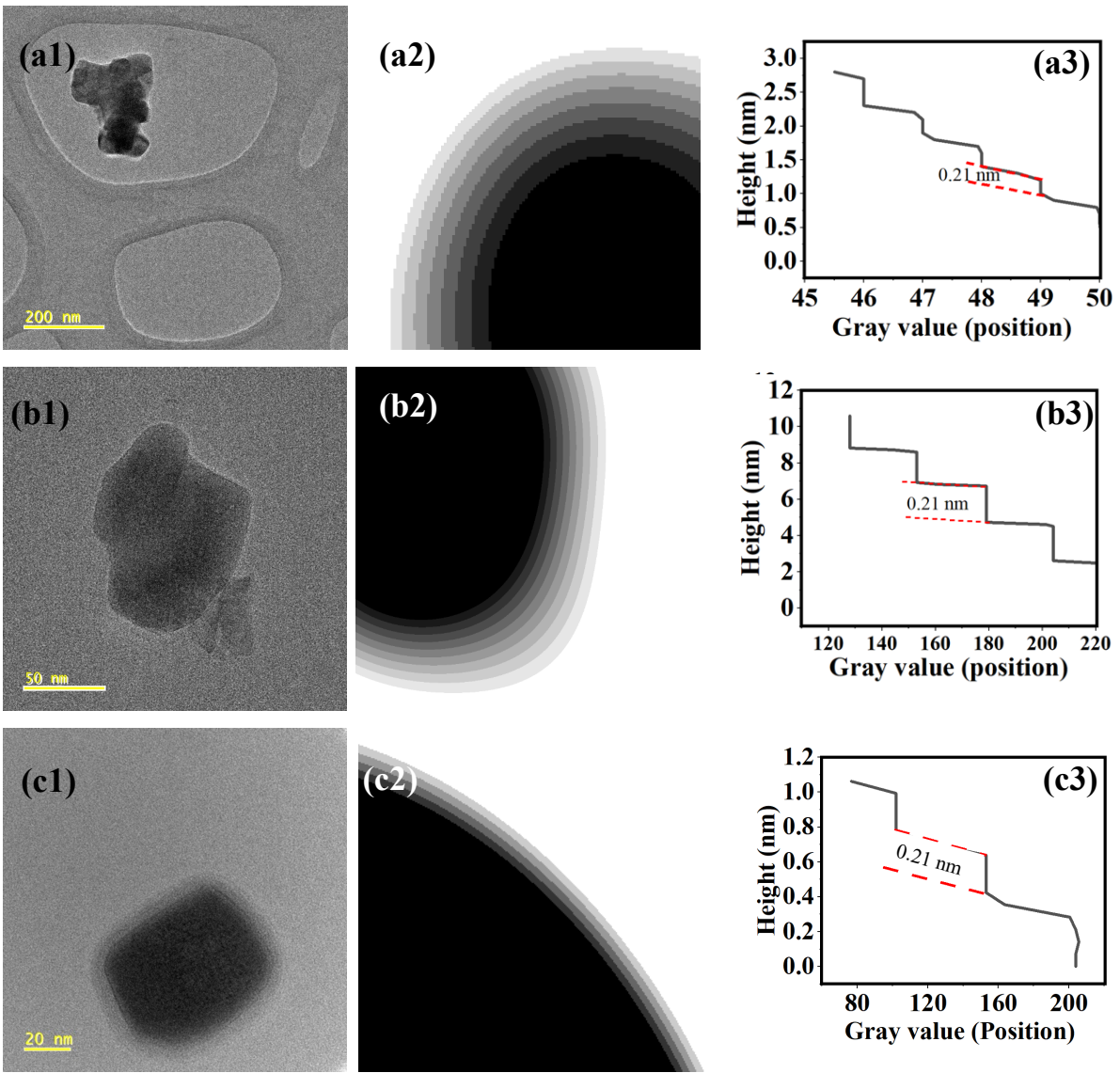


Figure 24. TEM image (a), ImageJ processed (b), and the histogram plot on the surface of the nanomaterial (c), of untreated SrTiO₃ (a1-3), SrO terminated (b1-3) and TiO₂ terminated SrTiO₃ (c1-3).

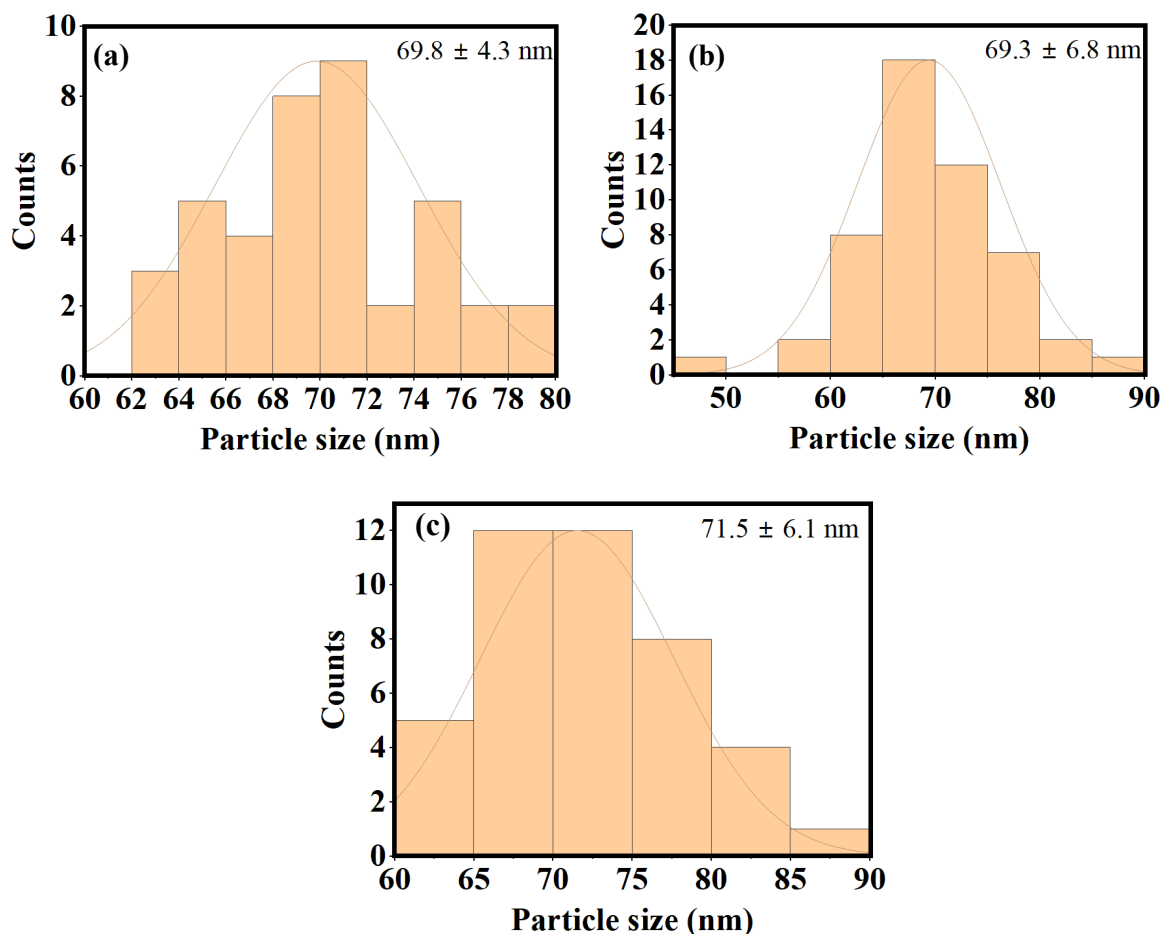


Figure 25. Particle size distribution graph of TiO_2 terminated (a), SrO terminated (b) and untreated SrTiO_3 (c).

5.4. X-ray photoemission spectroscopy

The X-ray photoemission spectroscopy (XPS) of TiO_2 terminated SrTiO_3 was performed to determine the chemical composition and electronic properties of the nanoparticle (Fig. 26). The XPS survey shows the presence of Sr, Ti, O and C, confirming the formation of SrTiO_3 , where carbon is from the experimental setup for calibration. The peaks at 131.8 eV and 133.6 eV correspond to the Sr 3d with the orbital spin of $3d_{5/2}$ and $3d_{3/2}$ which represent the oxidation state of Sr^{2+} [121]. The strong peak at 457.3 eV and 463.0 eV corresponds to Ti 2p with the orbital spin of $2p_{3/2}$ and $2p_{1/2}$ indicating the oxidation state of Ti^{4+} [121]. In addition, the peaks at 471.1 eV and 478.2 eV are attributed to the satellite peak of Ti. The binding energy at 528.7 eV and 530.8 eV is attributed to the O 1s orbital with the oxidation state of O^{2-} , where the strongest peak at 528.7 eV is attributed to the lattice oxygen (Ti-O) and the weakest peak is associated to surface oxygen presenting through water and carbonates (530.8 eV) [121]. On the TiO_2 terminated SrTiO_3 , a shift in the Ti $2p_{3/2}$ and $2p_{1/2}$ peak is observed in comparison with the SrO terminated and untreated

SrTiO₃, where the peaks match. In addition, a peak shift is also observed in the Sr 3d_{5/2} and 3d_{3/2} in the case of SrO terminated SrTiO₃, when compared to the same peaks on the TiO₂ terminated and untreated SrTiO₃. A peak shift in the oxygen spectrum (O 1s) is also observed on TiO₂ terminated SrTiO₃, whereas it is not observed in the other two samples, which is due to the Ti-O binding in the SrTiO₃ crystal. The peak shifts are indicated in the Table. 1. These observations are clearly indicative of differences in surface compositions of the three samples possibly arising from the variation in surface terminations. However, this result in isolation is not ideal to identify the surface termination in a sample and will need to be interpreted in conjunction with other characterizations.

Table 1. XPS peaks of Ti, Sr and O spectra of TiO₂-terminated, SrO-terminated, and untreated SrTiO₃ nanoparticles.

	Sr	Ti	O
SrTiO ₃	132.7	457.7	528.7
	134.4	463.4	530.8
SrO terminated SrTiO ₃	132.5	457.8	528.7
	134.1	463.6	530.7
TiO ₂ terminated SrTiO ₃	132.7	458.1	529.2
	134.4	464.0	531.6

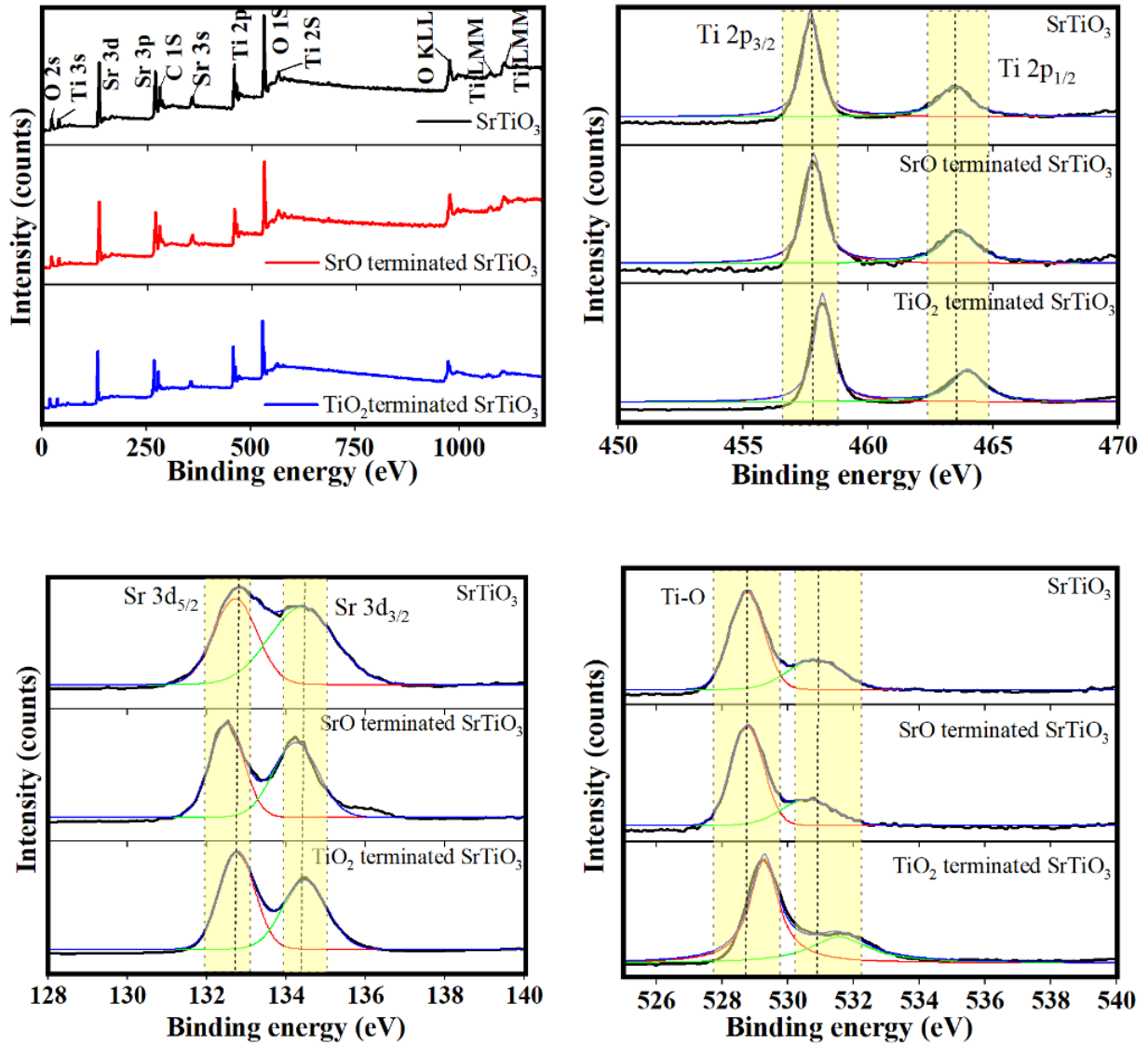


Figure 26. XPS spectrum of different surface terminated SrTiO₃ samples.

5.5. UV-visible-NIR spectroscopy

To determine the optical properties and band gap of the surface engineered SrTiO₃ (SrO terminated and TiO₂ terminated) and untreated SrTiO₃ nanoparticles UV-visible-NIR spectroscopy was performed. The results are shown in Fig. 27a. The tauc plot of the absorption spectrum of the prepared nanomaterial is shown in Fig. 27b. The indirect band gap of the material was determined using the Tauc equation [122] (Eq. 47)

$$(\alpha h\nu)^{1/n} = A(h\nu - E_g) \quad (47)$$

where A , h , E_g and n represent the absorption co-efficient, Planck constant, band gap energy and Tauc exponent respectively. The results show that the band gap energy of all the nanoparticles is 3.25 eV. This confirms that the surface engineering has no effect the band gap energy of the material, and the difference in the catalytic activity was mainly due to the reactive site kinetics on the surface [93].

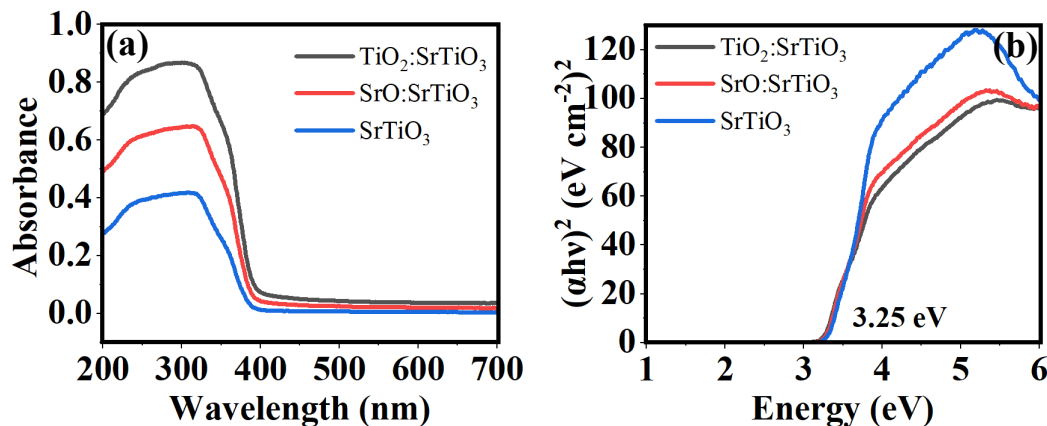


Figure 27. (a) UV-VIS-NIR absorption spectra and (b) Tauc plots of SrTiO₃ nanoparticles (normalized y axis).

5.6. Photoluminescence of SrTiO₃

Generally, the photoluminescent (PL) properties of nanomaterials are performed to attribute the order-disorder degree to the electronic state of the crystal. The PL spectrum of the SrO terminated, TiO₂ terminated SrTiO₃ and untreated SrTiO₃ with the excitation of 355 nm was measured and is illustrated in Fig. 28. The results show that the two peaks at 446.7 and 567.2 nm indicate the blue and green emissions which represent the electron from the excited state jumps to the intermediate state (mostly owing to defect states) and then falls back to the ground state [123, 124]. The higher the intensity of the PL spectra the higher the rate of recombination of charge carriers [125]. The results show that the intensity of the PL emission is higher for TiO₂ terminated SrTiO₃ as compared to the SrO terminated or the untreated SrTiO₃. Nevertheless, despite the high rate of recombination, the catalytic activity is based on the surface interactions and the number of reactive sites. Considering that the reactive sites of the SrO terminated SrTiO₃ are easily occupied by $-CO_3^{2-}$ thereby inhibit the catalytic activity on the minerlization of toxic pollutant for water treatment, whereas SrO terminated SrTiO₃ shows a higher effeciecny for CO₂ reduction owing to the same reason [126].

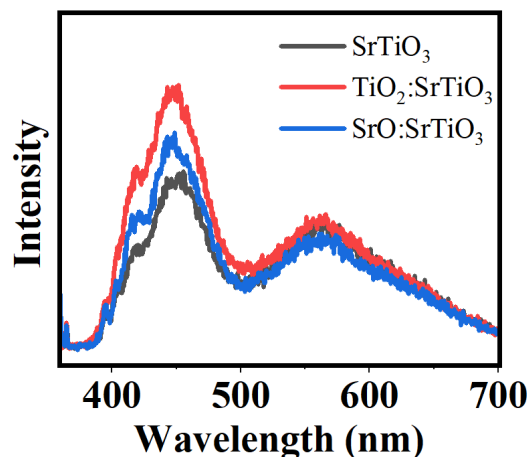


Figure 28. Photoluminescence spectra of SrTiO₃ samples.

5.7. Zeta potential

To determine the surface charge of the synthesised SrO terminated, TiO₂ terminated and untreated SrTiO₃ nanoparticles, zeta potential was measured, the results of which, are illustrated in Fig. 29. The zeta potential of TiO₂ terminated (-9.8 mV) and untreated SrTiO₃ (-10.1 mV) showed a high negative surface charge, whereas the SrO terminated SrTiO₃ showed a surface charge of 0.4 mV indicative of surface neutralization by carbonate adsorption. In addition, the surface of untreated SrTiO₃ is made up of 50% TiO₂ terminated layer which promote the adsorption of hydroxyl ions leading to the high surface charge, which confirms that the TiO₂ layer is highly active to adsorption in comparison to SrO terminated SrTiO₃.

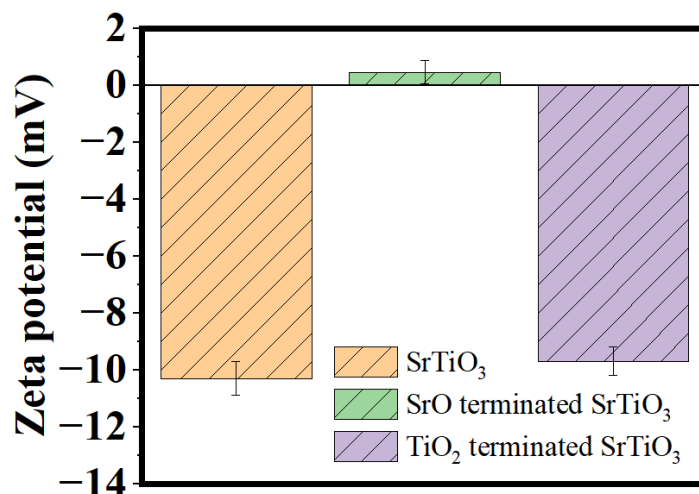


Figure 29. Zeta potential analysis of TiO₂-terminated, SrO-terminated and untreated SrTiO₃ samples.

5.7. Photocatalysis

The photocatalytic activity of SrTiO₃ (SrO and TiO₂ terminated) NPs was determined by the photodegradation of methyl orange. Here, for each reaction mixture consisting of one type of SrTiO₃ (SrO-, TiO₂- terminated and untreated) NPs and methyl orange (50: 10 mg/L), the reaction mixture was stirred for 30 min to attain the adsorption and desorption equilibrium, and then irradiated with a constant intensity illumination of 100 mW/cm². The transmittance was recorded at random intervals of time until the complete mineralization of methyl orange was observed. The photocatalytic degradation efficiency of untreated SrTiO₃, SrO terminated SrTiO₃ and TiO₂ terminated SrTiO₃ was calculated to be 25.35 ± 0.9%, 40.6 ± 1.6% and 94 ± 1.6% in 120 min respectively (Fig. 28). The degradation efficiency of methyl orange by TiO₂ terminated SrTiO₃ was three times higher than SrO terminated SrTiO₃ (Table.1). The rate kinetics on the photocatalytic degradation of methyl orange by SrTiO₃ (SrO and TiO₂ terminated) NPs was calculated by Eq. 48.

$$\ln\left(\frac{C}{C_0}\right) = kt \quad (48)$$

where C and C₀ represent the transmittance at time t=0 and at time 't'. Here, the photodegradation of methyl orange follows the zero order kinetic reaction (Fig. 30), with rate constants (min⁻¹) of 0.0035 (SrO terminated SrTiO₃ NPs), 0.009 (TiO₂ termination SrTiO₃ NPs) and 0.0023 (SrTiO₃ without surface treatment) and a regression co-efficient of <0.95 (Table. 2). The results shows that the catalytic activity of TiO₂ terminated SrTiO₃ was higher than the SrO terminated SrTiO₃ and untreated SrTiO₃ (without surface engineering).

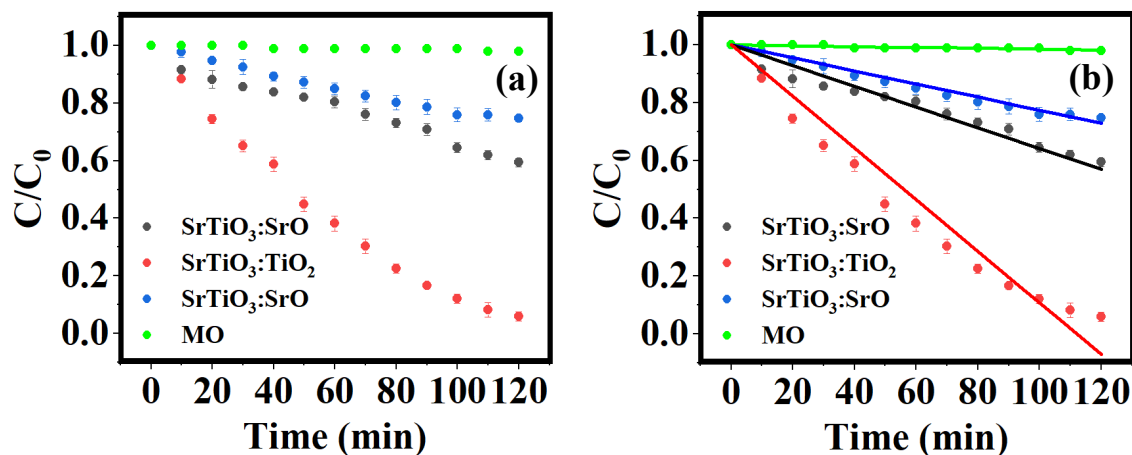


Figure 30. Plots of C/C₀: (a) Time-dependent variation of C/C₀, and (b) linear fit for the photocatalytic degradation of methyl orange using SrTiO₃ nanoparticles (MO – methyl orange, SrTiO₃:SrO – SrO terminated SrTiO₃ and SrTiO₃: TiO₂ – TiO₂ terminated SrTiO₃).

Table 2. Rate constant and degradation percentage of methyl orange against SrTiO₃ concentration (photocatalysis)

S/N	Photocatalysis (120 min)	SrTiO ₃ :TiO ₂	SrTiO ₃ :SrO	SrTiO ₃
1.	Rate constant (min ⁻¹)	0.009	0.0035	0.0023
2.	Degradation (%)	94 ± 1.6	40.6 ± 1.6	25.35 ± 0.9

5.8. Sono-photocatalysis

To improve the catalytic activity of the SrTiO₃ against methyl orange and to resolve the rate-limiting step in photocatalysis (mass transfer), the catalytic photodegradation of MO using SrTiO₃ nanoparticles was performed with the combination of sonification in intervals. Briefly, the SrTiO₃ (TiO₂ terminated) NPs and methyl orange (50: 10 mg/L) reaction mixture was stirred for 30 min to attain the adsorption and desorption equilibrium. Then the reaction mixture was irradiated under 100 mW/cm² for 60 minutes, followed by the introduction of a sonification phase (varying between 0 to 300s), where the solar irradiation is stopped during the duration of the sonification. The transmittance of the reaction mixture was determined by the spectrophotometric set-up at regular intervals of time (Fig. 30a). The plot of the relative concentration of the methyl orange on photobleaching shows that the percentage of photocatalysis in the presence of sonification increases from 63.3 to 94.4% under 60 min irradiation (Table. 2). The degradation rate on the photocatalytic degradation of methyl orange against TiO₂ terminated SrTiO₃ with various sonification durations follows zero order kinetics (Fig. 30b). The rate of the degradation of methyl orange against TiO₂ terminated SrTiO₃ under different sonification durations, increases from 0.011 to 0.0155 min⁻¹ (Table. 3). The results show that the catalytic activity of TiO₂ terminated SrTiO₃ increases 1.3 times with the combination of sonification, which is relatively higher than only photocatalysis without sonification.

Table 3. Rate constant and degradation percentage of methyl orange of sono-photocatalysis in TiO₂-terminated SrTiO₃ with varying sonification interval duration.

S/N	Sonfication (s)	Rate constant (min ⁻¹)	Degradation percentage (%)
1.	0	0.011	63.3 ± 1.33
2.	6	0.0114	66.9 ± 0.81
3.	18	0.0122	68.2 ± 0.86
4.	30	0.013	71.5 ± 0.98
5.	60	0.0136	76.1 ± 1.03
6.	100	0.0138	81.2 ± 1.96
7.	300	0.0148	89.2 ± 2.02
8.	600	0.0155	94.4 ± 1.17

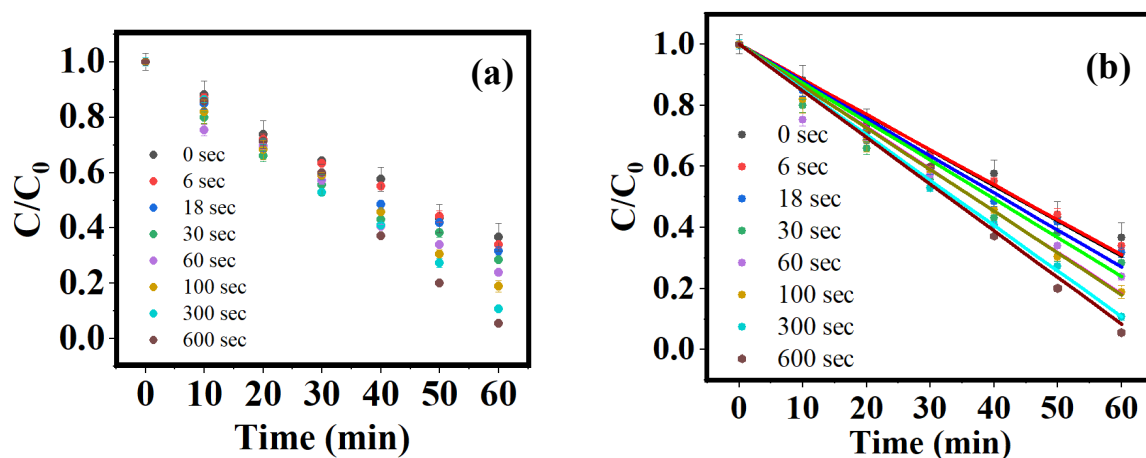


Figure 31. Plot of C/C_0 (a), liner fit on plot C/C_0 (b) on the sono-photocatalytic degradation of methyl orange by TiO₂ terminated SrTiO₃ nanoparticles.

The plot on the rate of the catalytic degradation of methyl orange versus the sonification duration is illustrated in Fig. 32. The plots follow the exponential degradation of the methyl orange with an increase in the sonification duration from 0s to 100s and a sudden hike in the catalytic activity with between 100 to 300s. The plot was fitted with the exponential function, given by Eq. 49.

$$y = f(x) = a\left(1 - \exp\left(-\frac{x-b}{c}\right)\right) + m \times x \quad (49)$$

where $m \times x$ represents the steady increase after 100 s pulse (m is slope of this increment). The results show that the sonification increases the catalytic efficiency, the sonification enhances the mixing from 0 to 100s. The immediate increase in the catalytic activity after 100s instead of saturation might due to be the activation of either sonocatalytic or tribocatalytic mechanism on the degradation of methyl orange against TiO_2 terminated SrTiO_3 . As the Goldschmidt tolerance of SrTiO_3 is unity ($t = 1$), the nanoparticle will not show piezocatalysis [127].

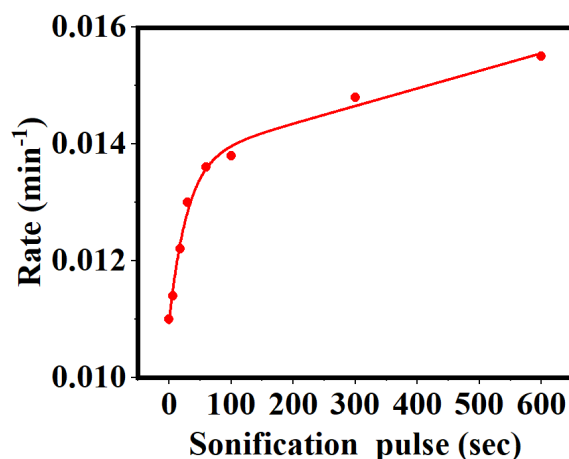


Figure 32. Plot of the reaction rate of sono-photocatalytic activity versus sonification interval duration on the catalytic degradation of methyl orange against TiO_2 -terminated SrTiO_3 .

In other words, to explain the trend of Fig. 32, we suggest that there is a beneficial contribution of the sonification to the mass transport which tremendously enhances the reaction rate even for very short sonification durations. This effect should then saturate as more sonification beyond 100s should not further improve the reaction rate. We however see a linear trend for even longer sonifications which indicates that sonification itself also has a contribution to the catalytic performance, most likely due to either sono-, or tribocatalysis.

Similarly, the sono-photocatalytic activity of the SrO terminated SrTiO_3 and untreated SrTiO_3 was performed at 600s and illustrated in Fig. 33. The results show that the degradation was more effective with TiO_2 terminated SrTiO_3 than with SrO terminated SrTiO_3 and untreated SrTiO_3 nanoparticles (Fig. 33). Here, the rate of the reaction for TiO_2 - terminated SrTiO_3 shows the combination of first order (until 30 min) and zero order reaction (predominantly from 30 min to 60

min), with a combined rate constant of 0.059 min^{-1} . The rate of the degradation of SrO terminated SrTiO_3 and untreated SrTiO_3 nanoparticle was 1.7 times and 1.3 times lower than the TiO_2 terminated SrTiO_3 (Table. 4). In comparison, with the photocatalysis and sono-photocatalysis experiment, the increase in the efficiency of catalysis was sequenced as TiO_2 terminated $\text{SrTiO}_3 > \text{SrO}$ terminated $\text{SrTiO}_3 > \text{untreated SrTiO}_3$ for photocatalysis, whereas the efficiency of sono-photocatalysis was ordered as TiO_2 terminated $\text{SrTiO}_3 > \text{untreated SrTiO}_3 > \text{SrO}$ terminated SrTiO_3 for sono-photocatalysis. The lower activity of SrO terminated SrTiO_3 was due to the formation of $\text{Sr}(\text{CO}_3)$, which blocks the reactive sites for the catalytic degradation of methyl orange, which reaction was also increased by the sonification resulting in even lower available active sites on the SrO when compared to only photocatalysis. As a result, photocatalysis (and sono-photocatalysis, either by themselves or in combination) could also act as one of the tools to determine the different termination of SrTiO_3 nanoparticles as SrO terminated or TiO_2 terminated.

Table 4. Rate constant and degradation percentage of methyl orange against TiO_2 terminated SrTiO_3 , SrO terminated SrTiO_3 and untreated SrTiO_3 nanoparticles (sono-photocatalysis at 600s sonification interval)

S/N	Sono-photocatalysis (60 min)	$\text{SrTiO}_3:\text{TiO}_2$	$\text{SrTiO}_3:\text{SrO}$	SrTiO_3
1.	Rate constant (min^{-1})	0.0155	0.0091	0.0113
2.	Degradation (%)	94.4 ± 1.6	57.3 ± 1.6	67 ± 0.9

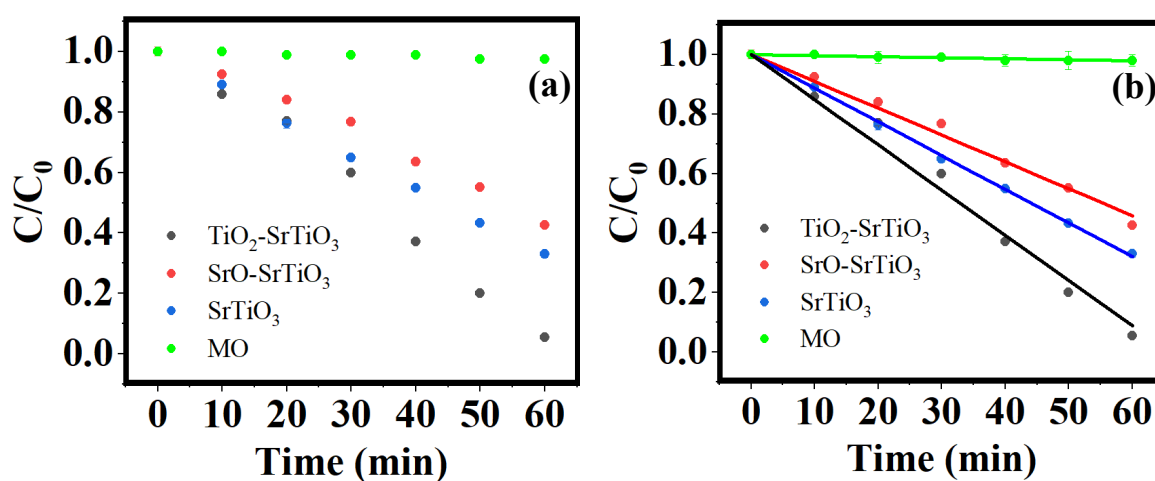


Figure 33. Plots of C/C_0 : (a) Time-dependent variation of C/C_0 , and (b) linear fit for the sono-photocatalytic degradation of methyl orange using TiO_2 -terminated SrTiO_3 , SrO-terminated SrTiO_3 , and untreated SrTiO_3 nanoparticles (sonication interval: 600 s, MO – methyl orange).

Further, to determine the comparative efficiency and propagation of error, the photocatalytic activity with sonication was performed with TiO₂ (P25, 50 mg/L) using the same experimental parameters as those used for SrTiO₃. The results shows that the rate of the reaction on photocatalysis with sonication against TiO₂ was 0.0074 to 0.0096 (0 to 600s) as illustrated in Table. 4. The results show that the catalytic efficiency of TiO₂ terminated SrTiO₃ is 1.5 times higher than the standard TiO₂ for a 600s sonification duration (Fig. 34a and 34b). In addition, the plot of the rate of the reaction versus the sonification interval in the sono-photocatalytic degradation of methyl orange against TiO₂ is shown in Fig. 32c. The results display that the sonification increases the catalytic efficiency by enhancing the mixing from 0 to 100s (Fig. 34c, Table. 5), while the sudden increase in the catalytic activity after 100s rather than saturation might be due to be the activation of sonocatalytic or tribocatalytic mechanism on degradation of methyl orange against TiO₂.

Table 5. Rate constant and degradation percentage of methyl orange against TiO₂ (sono-photocatalysis)

S/N	sonification (s)	Rate constant (min ⁻¹)	Degradation percentage (%)
1.	0	0.0074	47.3 ± 2.55
2.	6	0.008	48.1 ± 1.09
3.	18	0.0081	49.7 ± 2.93
4.	30	0.0085	50.1 ± 0.98
5.	60	0.0085	51.4 ± 0.32
6.	100	0.0086	53.2 ± 1.88
7.	300	0.009	57.5 ± 3.02
8.	600	0.0096	59.1 ± 4.41

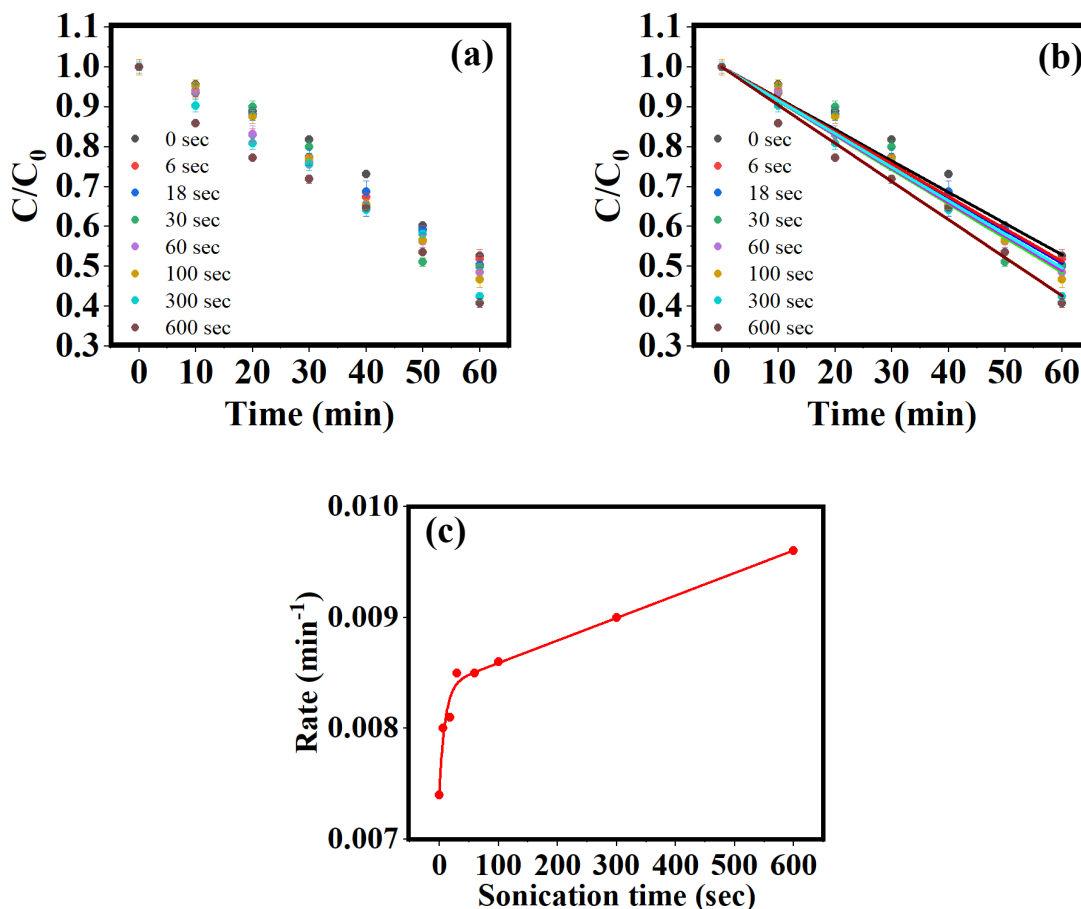


Figure 34. Sono-photocatalytic degradation of methyl orange using TiO_2 : (a) Time-dependent variation of C/C_0 , (b) linear fit of C/C_0 , and (c) reaction rate as a function of sonication interval duration.

Further, to determine if the sudden hike from 100 to 600s sonification interval is due to the increase in the sonification interval between two photo cycles, the photocatalysis experiment was repeated with the absence of the sonification and instead a chopping illumination (light switched ON and OFF at regular intervals) experiment was performed with the TiO_2 terminated SrTiO_3 against methyl orange (Table. 6). The plot of the relative concentration, shows that the catalytic activity in the absence of irradiation did not have any effect on the rate of the reaction (Fig. 35a and 35b). In addition, the plot on the rate of the reaction vs the interval duration of light shut off did not undergo the exponential degradation (Fig. 35c).

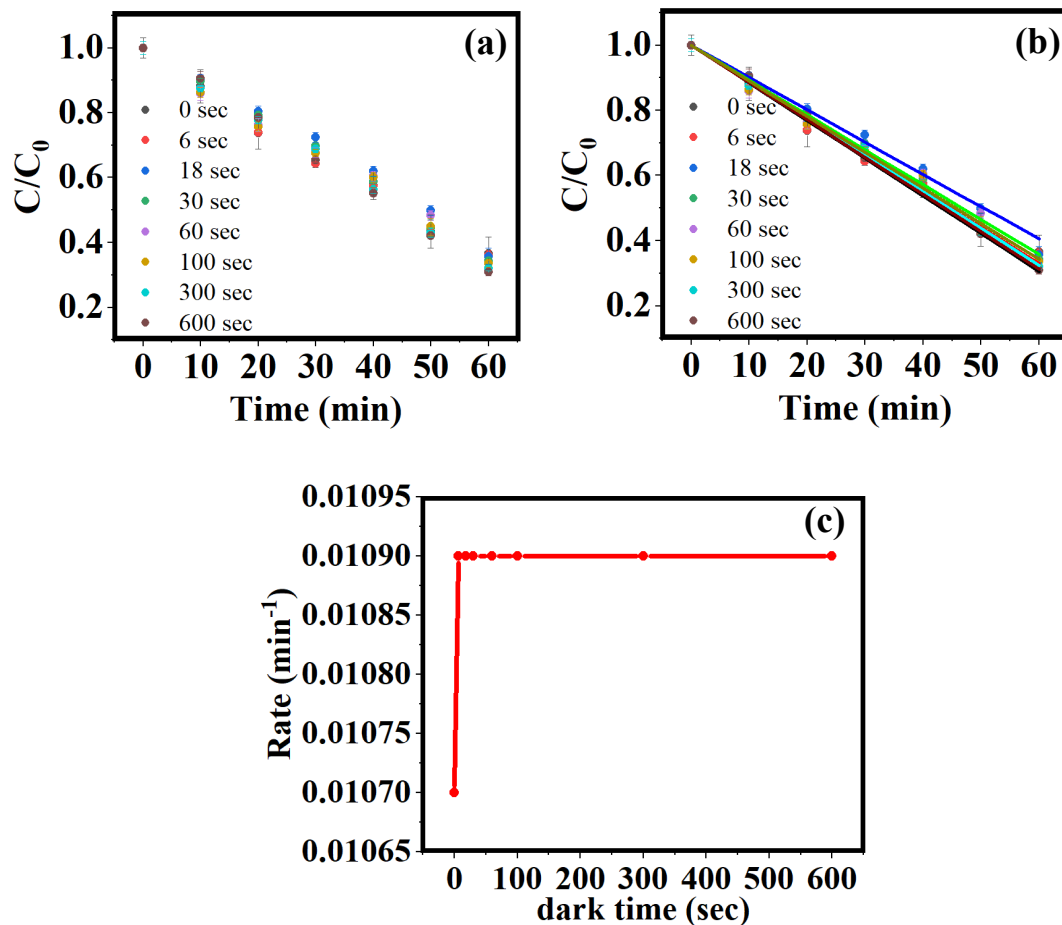


Figure 35. Photocatalytic degradation of methyl orange by TiO₂-terminated SrTiO₃ at room temperature (light-off pulse): (a) Time-dependent variation of C/C_0 , (b) linear fit of C/C_0 , and (c) reaction rate as a function of light- on and off pulse.

Table 6. Rate constant and degradation percentage of methyl orange against TiO₂ terminated SrTiO₃ photocatalysis.

S/N	Light off (s)	Rate constant (min ⁻¹)	Degradation percentage (%)
1.	0	0.0107	63.3 ± 3.27
2.	6	0.0109	63.9 ± 0.91
3.	18	0.0109	64.6 ± 2.20
4.	30	0.0109	65.6 ± 1.51
5.	60	0.0109	66.5 ± 0.62
6.	100	0.0109	67.1 ± 0.34
7.	300	0.0109	68 ± 0.90
8.	600	0.0109	69.1 ± 1.22

Further, to study the sono catalytic effect on the degradation of methyl orange against TiO₂ terminated SrTiO₃, the experiment was performed at 60 °C where the increase in the temperature increases the rate of bubble cavitation and therefore confirms the effect of sonocatalysis. Generally, at high temperature sono-catalytic effect increases and the tribo-catalytic effect decreases [128, 129]. The plot on the relative concentrations shows that the catalytic activity was higher from 0s to 100s which explains the effective agument of improved mixing to boost the mass transfer between the nanoparticle and methyl orange (Fig. 36a and 36b). As similar to the sono-photocatalytic experiment at room temperature, the sudden hike in the rate of the reaction from 100 to 600s was observed with sonification at 60 °C also, where the rate of the reaction is relatively higher at 60 °C than at room temperature (Fig. 36c and Table. 7).

Table 7. Rate constant and degradation percentage of methyl orange against sonophotocatalysis in TiO₂ terminated SrTiO₃ at 60 °C.

S/N	Sonification (s)	Rate constant (min ⁻¹)	Degradation percentage (%)
1.	0	0.0106	63.3 ± 3.27
2.	6	0.0106	65.0 ± 0.91
3.	18	0.0112	69.0 ± 2.20
4.	30	0.0124	73.7 ± 1.51
5.	60	0.0127	76.6 ± 0.62
6.	100	0.0133	80.0 ± 0.34
7.	300	0.0157	92.7 ± 0.90
8.	600	0.0158	96.6 ± 1.22

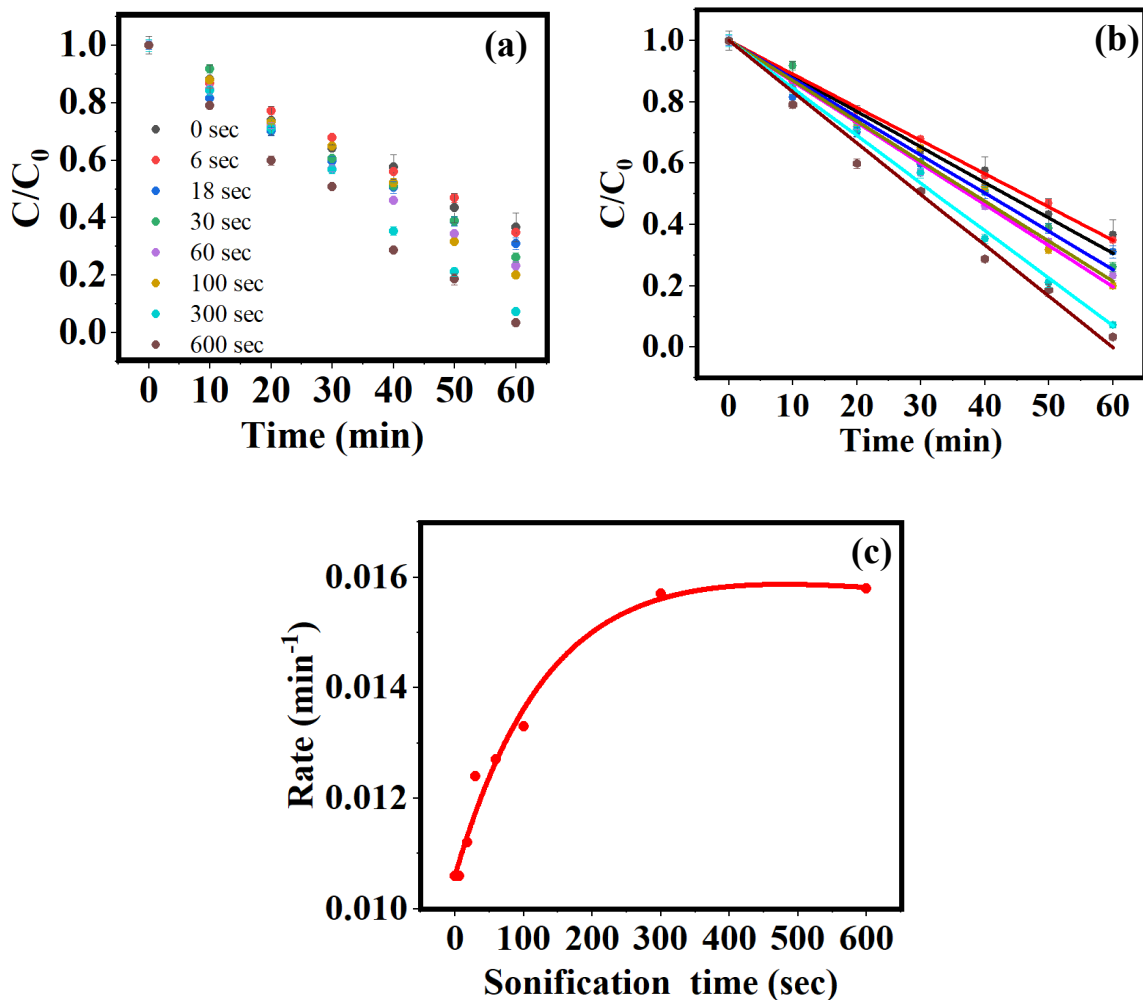


Figure 36. Sono-photocatalytic degradation of methyl orange at 60 °C by TiO_2 -terminated SrTiO_3 : (a) Time-dependent variation of C/C_0 , (b) linear fit of C/C_0 , and (c) reaction rate as a function of sonication duration.

In addition, to confirm the effect of sonocatalysis, the catalytic experiment with sonication intervals (0 to 600s) at 60 °C (without illumination) was performed and the catalytic efficiency was determined. The plot of the relative concentration at different sonication intervals (0 to 600s), shows that the catalytic activity was constant (almost nil) from 0 to 30s, with a slight increase at 60s and 100s, and a hike in the catalytic activity from 300 to 600s (Fig. 37a and 37b, Table. 8). The plot on the rate kinetics versus the sonication interval does not follow the exponential degradation seen before, which shows that the catalytic activity increase from 300 to 600s was due to the effect of bubble cavitation (Fig. 37c).

Table 8. Rate constant and degradation percentage of methyl orange against sono-catalysis in TiO₂ terminated SrTiO₃ at 60 °C.

S/N	Sonification (s)	Rate constant (min ⁻¹)	Degradation percentage (%)
1.	0	0.0001	0
2.	6	0.0001	0
3.	18	0.0001	0
4.	30	0.0004	0
5.	60	0.0004	2.2 ± 1.10
6.	100	0.0004	2.2 ± 0.93
7.	300	0.0014	8.9 ± 0.98
8.	600	0.0029	16.8 ± 0.40

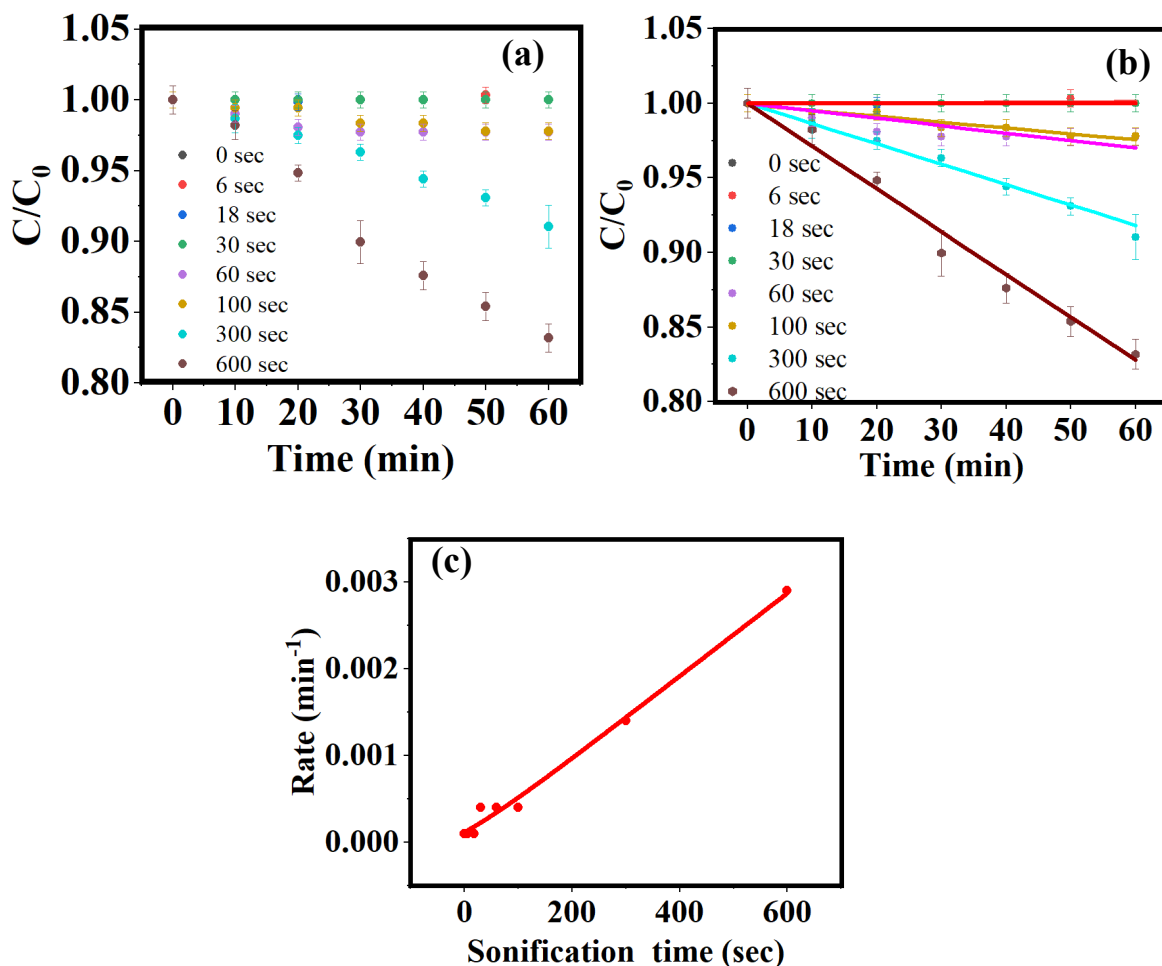


Figure 37. Sono-catalytic degradation of methyl orange by TiO_2 -terminated SrTiO_3 at 60 °C (varying sonication interval): (a) Time-dependent variation of C/C_0 , (b) linear fit of C/C_0 , and (c) reaction rate as a function of sonication duration.

In addition, a control experiment with only sonification (without illumination) at room temperature (25 °C) at intervals of 600s was performed. The results show the sonocatalysis at room temperature does not have any effect on the degradation of methyl orange against TiO_2 terminated SrTiO_3 (Fig. 38). Thus the results confirm the sono-catalytic effect, and not the tribocatalytic effect as the mechanism responsible for the sudden rise in reaction rate seen from 300 to 600s. Therefore, the present study demonstrates that the combination of light irradiation followed by sonification follows sono-photocatalysis. The sonocatalysis changes the rate of the reaction from first order to zero order, thereby increasing mass transportation. Further, to determine the effect of temperature in sonification of methyl orange was determined by performing sonocatalysis at 600s sonification interval duration at 25 °C and at 60 °C, the results shows that the methyl orange doesn't undergo degradation upon sonification at 25 °C and at 60 °C.

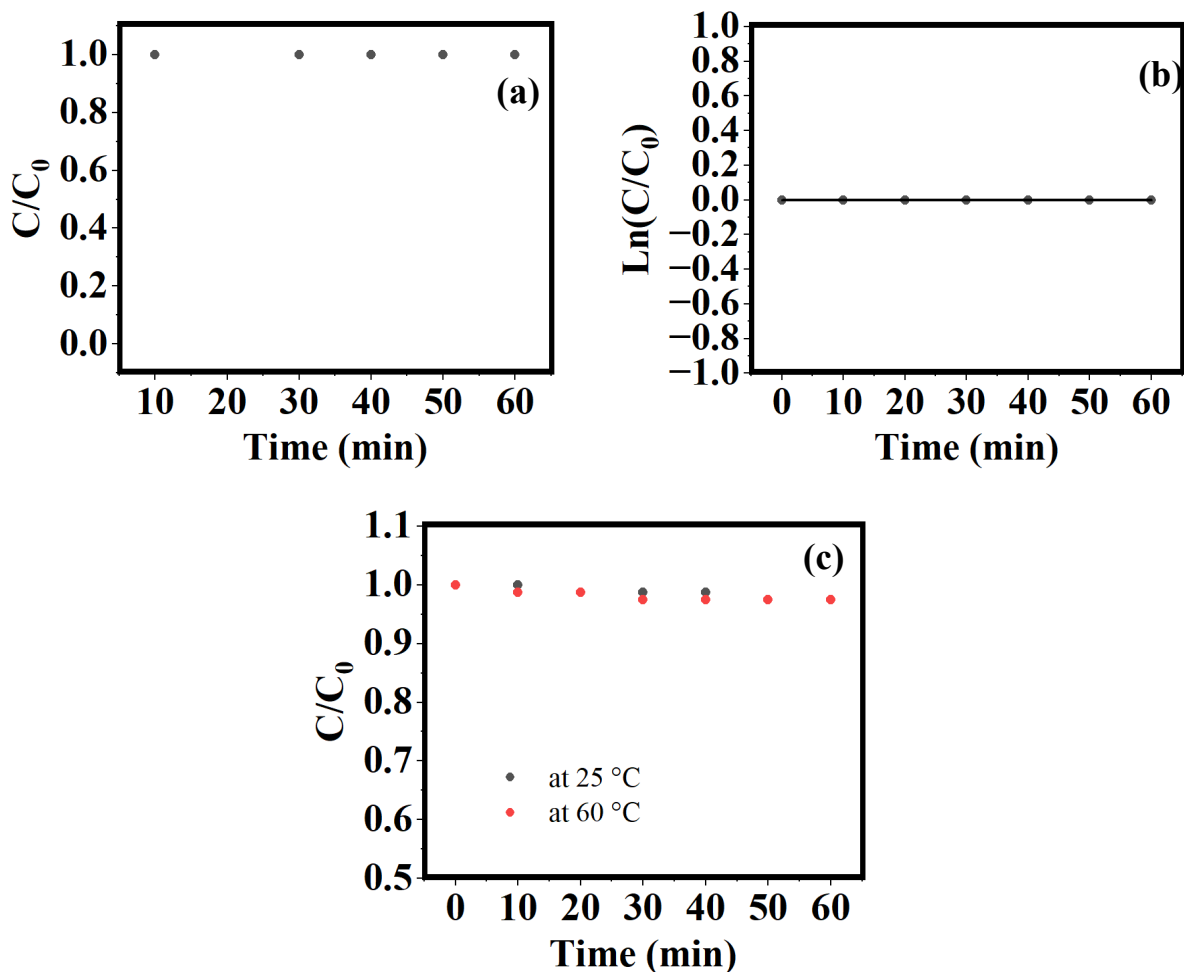


Figure 38. Sono-catalytic degradation of methyl orange by TiO_2 -terminated SrTiO_3 : (a) Time-dependent variation of C/C_0 , (b) $\ln(C/C_0)$ at room temperature (600 s sonication interval), and (c) sonocatalytic effect of methyl orange at 25 °C and 60 °C (600 s sonication interval).

5.9. Optimization of sono-photocatalytic activity of TiO_2 terminated SrTiO_3

Further, the sono-photocatalytic activity of TiO_2 terminated SrTiO_3 was performed at 600s sonification interval by varying the concentration of the methyl orange by keeping the nanoparticle concentration constant (50 mg/L). The plot on the relative concentration shows that the degradation increases with a decrease in the concentration of methyl orange (20 mg/L to 5 mg/L) (Fig. 39 and Table. 9). At higher concentrations, the degradation slows down due to the competitive absorption of light by methyl orange and reduced availability of active sites on the photocatalyst surface.

Table 9. Rate constant and degradation percentage of methyl orange against sono-photocatalysis in TiO₂ terminated SrTiO₃ by varying the concentration of methyl orange.

S/N	Photocatalysis (60 min)	5 mg/L	10 mg/L	15 mg/L	20 mg/L
1.	Rate constant (min ⁻¹)	0.0156	0.0154	0.0125	0.0112
2.	Degradation (%)	95.9 ± 0.70	94.4 ± 1.08	79.3 ± 1.37	64 ± 1.61

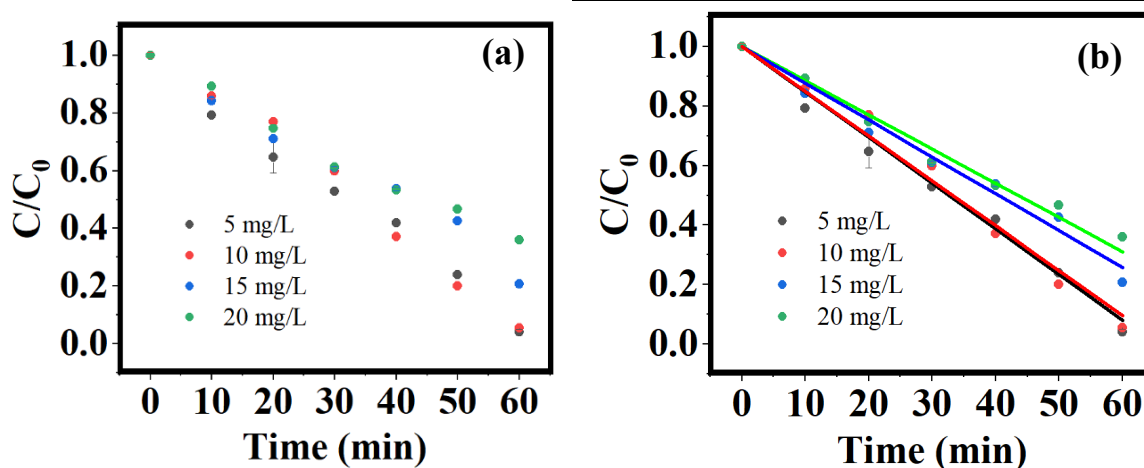


Figure 39. Plot of C/C_0 (a) and linear fit on plot C/C_0 (b) on the sono-photocatalytic degradation of methyl orange by TiO₂ terminated SrTiO₃ for different concentrations of methyl orange.

In addition, the sono-photocatalytic activity of TiO₂ terminated SrTiO₃ was performed at 600s sonification interval by varying the concentration of the nanoparticle by keeping the methyl orange concentration as constant (50 mg/L). The plot on the relative concentration shows that the degradation increases with an increase in the concentration of the nanoparticle (10 mg/L to 100 mg/L) (Fig. 40 and Table. 10). The higher the concentration of nanoparticle increase the adsorption of methyl orange and thereby increase in the rate of the reaction. Nevertheless, it is not advisable to dump kilogram of SrTiO₃ for water treatment.

Table 10. Rate constant and degradation percentage of methyl orange against sono-photocatalysis in TiO₂ terminated SrTiO₃ by varying the concentration of nanoparticle

S/N	Photocatalysis (60 min)	100 mg/L	50 mg/L	25 mg/L	10 mg/L
1.	Rate constant (min ⁻¹)	0.0164	0.0155	0.013	0.0109
2.	Degradation (%)	97.7 ± 1.11	94.4 ± 1.08	80.9 ± 0.97	67.9 ± 1.09

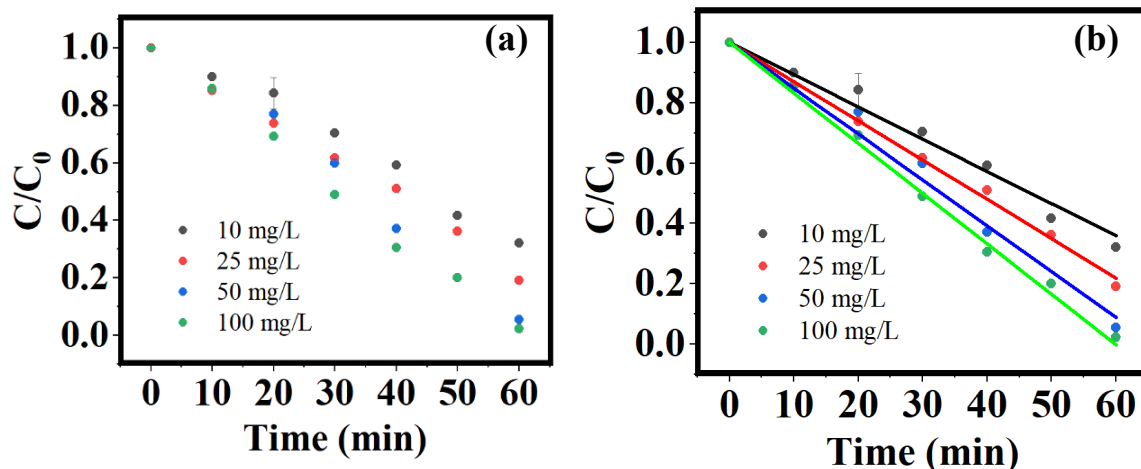


Figure 40. Plot of C/C_0 (a) and $\ln(C/C_0)$ (b) on the sono-photocatalytic degradation of methyl orange by TiO₂ terminated SrTiO₃ for different concentrations of the nanoparticle.

5.10. Scavenging and photocorrosion

To determine the role of radicals on the sono-photocatalytic degradation of methyl orange against TiO₂ terminated SrTiO₃ nanoparticle, radical sequencers were added to the reaction mixture (AgNO₃ 1mM – 1 mL: electron, ethylenediaminetetraacetic acid (EDTA) 1 mM – 1mL - hole, isopropyl alcohol (IPA) 1mL: •OH and benzoquinone (BQ) 1mM – 1 mL: •O²⁻). The results shows that the degradation percentage was 95.9, 94.4, 79.3, 64 and 94.4% for EDTA, AgNO₃, BQ, IPA and no scavengers respectively (Fig. 41 and Table. 11). Similarly, the rate kinetics of the reaction with radical sequencers in terms of degradation of methyl orange, follow the order: no scavengers>EDTA>AgNO₃>BQ>IPA (Fig. 41b). The lower degradation percentage with IPA and BQ was due to the inhibition of the interaction of •OH and •O²⁻ with methyl orange, which shows that the •OH and •O²⁻ plays a major role in the catalytic degradation of methyl orange.

Table 11. Rate of the reaction and the degradation percentage of radical sequencing on the sono-photocatalytic degradation of methyl orange against concentration of TiO₂-terminated SrTiO₃

S/N	Sono-photocatalysis	EDTA	AgNO ₃	BQ	IPA
1.	Rate constant (min ⁻¹)	0.0094	0.008	0.0028	0.0014
2.	Degradation (%)	95.9 ± 0.11	94.4 ± 5.5	79.3 ± 0.53	64 ± 0.77

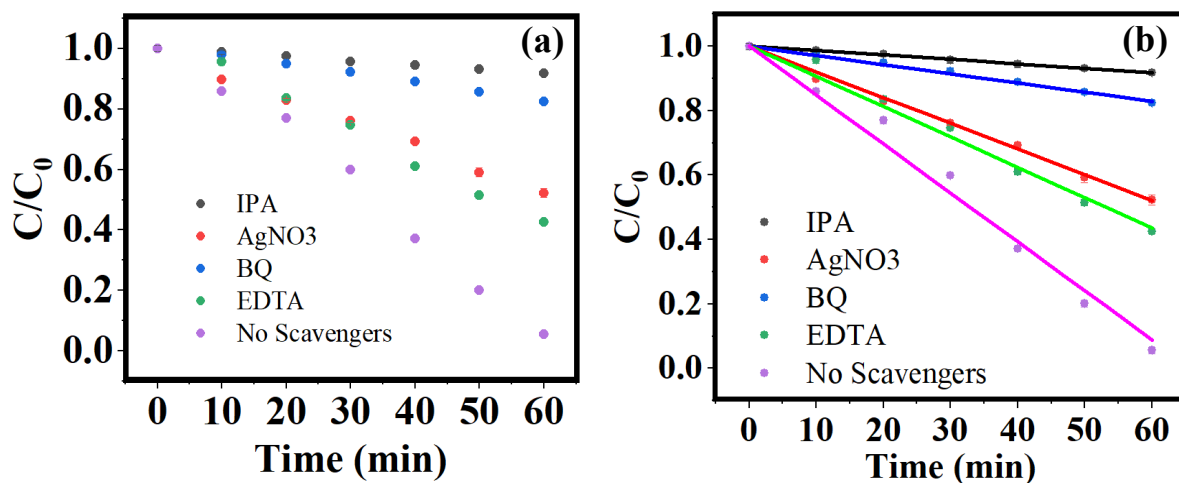


Figure 41. Radical sequencing on the sono-photocatalytic degradation of methyl orange against TiO_2 terminated SrTiO_3 (a) plot of C/C_0 vs time and (b) linear fit on plot C/C_0 vs time.

In addition, to determine the stability of the nanoparticle during catalysis, photocorrosion of the nanoparticle is studied by performing post catalysis XRD, TEM and XPS analysis of TiO_2 terminated SrTiO_3 (Fig. 40 and 41). Briefly, after the catalytic process, the TiO_2 terminated SrTiO_3 nanoparticles were collected by centrifugation, dried and then characterized. The results shows that the XRD and XPS spectrum of the TiO_2 terminated SrTiO_3 before and after catalysis remains the same, which indicate that the photocorrosion was minimal, if any (Fig. 42 and 43). TEM analysis of the TiO_2 terminated SrTiO_3 nanoparticle after catalysis showed that the nanoparticle retains its cubic shape with a size ~ 70 nm as before (Fig. 44), which further reaffirms the high stability of the nanoparticle under photocatalytic degradation of methyl orange.

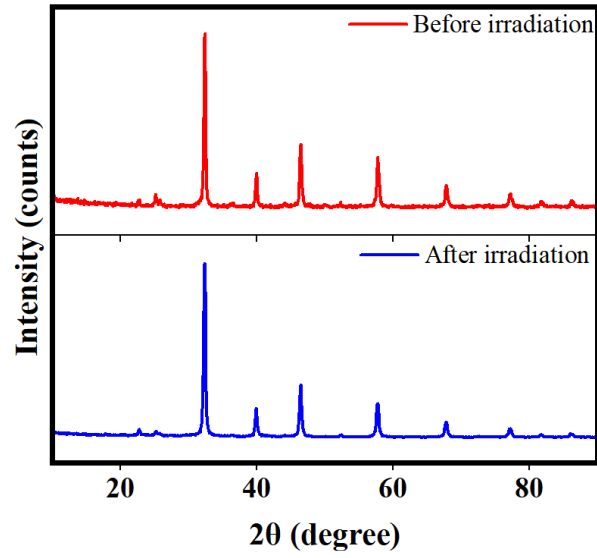


Figure 42. XRD patterns of TiO₂ terminated SrTiO₃ before and after catalysis (before irradiation - before catalysis and after irradiation - after catalysis).

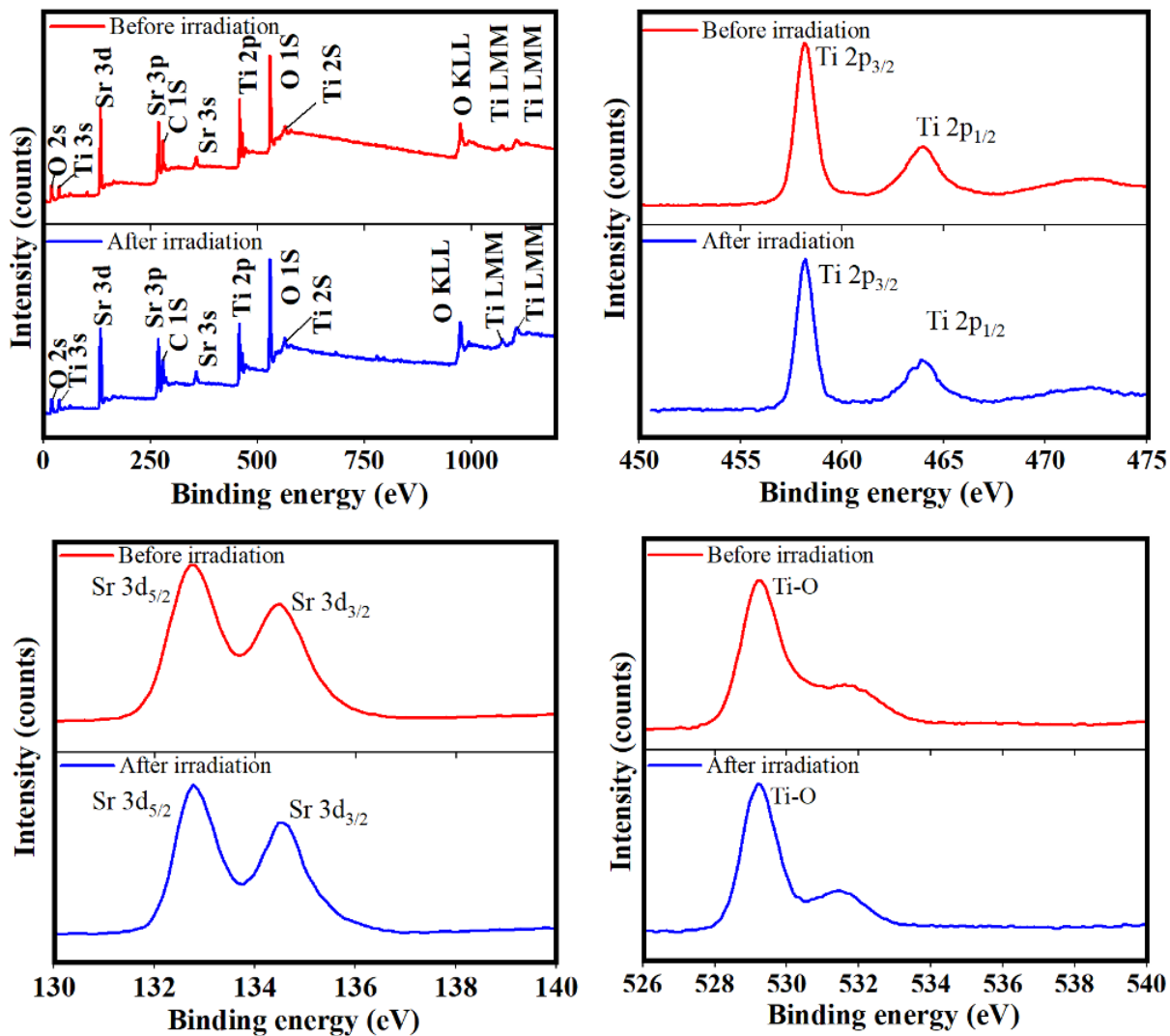


Figure 43. XPS spectrum of TiO₂ terminated SrTiO₃ before and after catalysis (before irradiation - before catalysis and after irradiation - after catalysis).

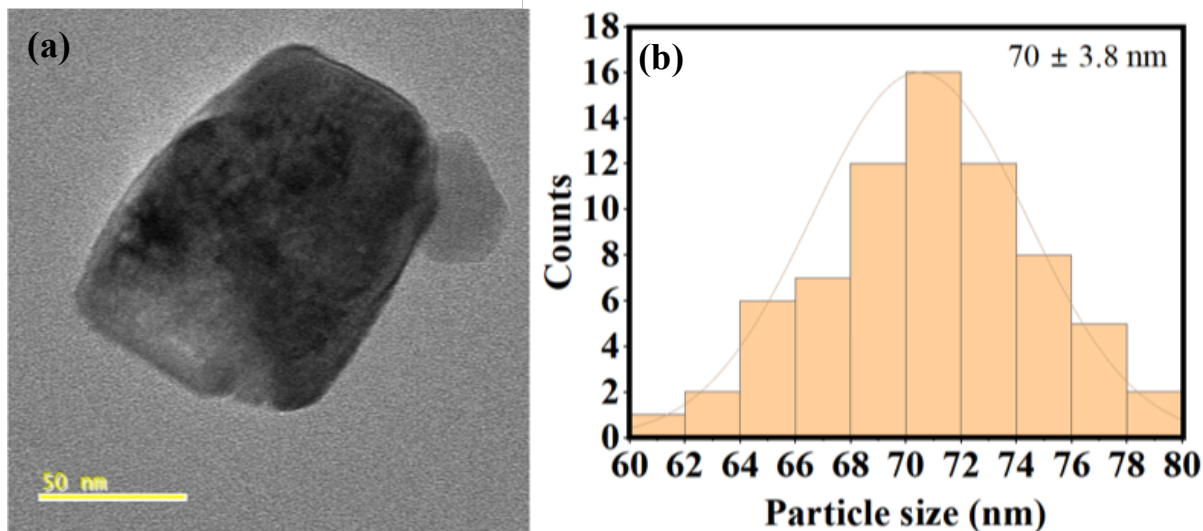


Figure 44. (a) TEM image and (b) particle size distribution plot of TiO₂ terminated SrTiO₃.

5.10. Tribo-catalysis of TiO₂

To better understand the tribo-catalytic effect, the tribo-catalytic degradation of methyl orange against TiO₂ with different concentrations was studied. Briefly, the tribo-catalytic experiment was performed by mixing 20 mL of methyl orange (10 mg/L) with different concentrations of TiO₂ (500 to 2000 mg/L) using magnetic stirring under dark condition to attain adsorption and desorption kinetics. Then the reaction mixture was sonicated for 60 min and the transmittance of the reaction mixture was determined before and after sonification. The tribo-catalytic degradation of methyl orange increases with an increase in the concentration of TiO₂ from 500 to 1000 mg/L and drops from 1000 to 2000 mg/L (Fig. 45a and 45b). The plot on the rate of the reaction versus the concentration of the TiO₂ follows the second-order polynomial fitting (Fig. 45c). The drop in the efficiency at a higher concentration above 1000 mg/L was due to the aggregation of the nanomaterial at higher concentrations. Further, to confirm the aggregation due to the tribo-catalytic effect, zeta potential of the TiO₂ with different concentrations was measured and shown in Fig. 46. The results show the high negative potential from 500 to 1000 mg/L which drops at the same as the degradation of MO with increase in TiO₂ concentration (Table. 12) confirming the aggregation of nanoparticles. Thus, the experiment confirms the tribo-catalytic effect is influenced by the stability and concentration of the nanomaterial.

Table 12. Zeta potential of different concentrations of TiO₂.

S/N	Photocatalysis (60 min)	500 mg/L	1000 mg/L	1500 mg/L	2000 mg/L
1.	Zeta potential (eV)	-6.8 ± 0.55	-14.2 ± 0.2	-8.87 ± 1.34	-8.19 ± 0.2
2.	Degradation percentage (%)	27.2 ± 2.0	50 ± 0.1	40 ± 0.1	3.6 ± 9.1

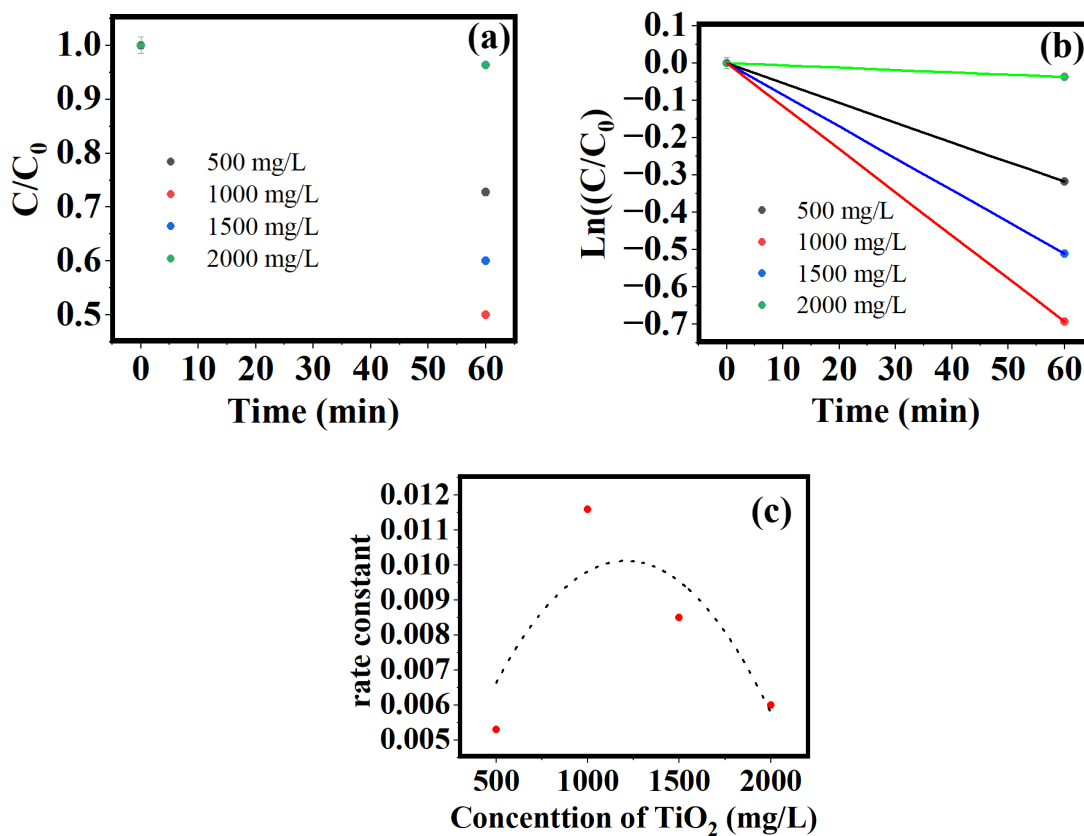


Figure 45. Plot of C/C_0 (a), $\ln(C/C_0)$ (b) and the reaction rate versus concentration of TiO₂ (c) on the tribocatalytic degradation of methyl orange by TiO₂.

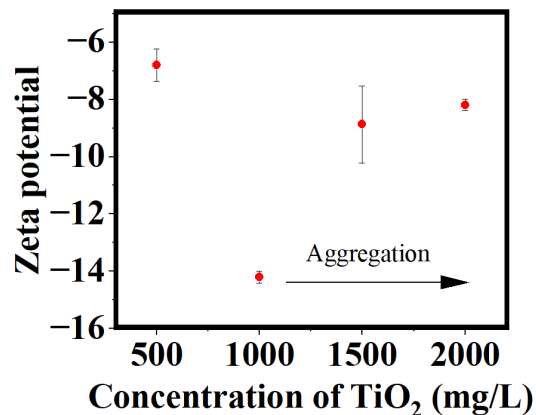


Figure 46. Zeta potential measurement of different concentrations of TiO₂.

In addition, the degradation efficiency of the present work is compared with the reaction rates reported in previous literature, as shown in Table 13. The surface-engineered TiO₂-terminated SrTiO₃, combined with sono-photocatalysis, demonstrates higher efficiency compared to some studies. Nevertheless, it is not the best reported in the literature. In summary, this study highlights that surface engineering and the combined influence of sonocatalysis significantly improve degradation activity by enhancing surface kinetics and mass transport, rather than relying on the formation of heterojunctions.

Table 13. Comparison table on catalytic degradation of methyl orange

Nanomaterial	Process	Rate kinetics (min ⁻¹)	Degradation efficiency (%)	Ref
Nd-TiO ₂ -SBA-15	Sono- photocatalysis	0.0108	70	[130]
CdS/g-C ₃ N ₄	Photocatalysis	0.025	-	[131]
TiO ₂ /CuO	Photocatalysis	0.0181	67.4	[132]
ZnO-NiO	Photocatalysis	0.050	83	[133]
Fe ₃ O ₄ @TiO ₂ core-shell	Photocatalysis	0.043	96	[134]
ZnO Nanorods	Photocatalysis	0.048	96.06	[135]
ZnFe ₂ O ₄	Sono- photocatalysis	0.038	75.9	[136]
CuO-TiO ₂ /rGO	Sono- photocatalysis	0.049	99	[137]
TiO ₂ terminated SrTiO ₃	Sono- photocatalysis	0.0155	94.4	(present study)

6 CONCLUSION AND PERSPECTIVES

6.1. Conclusion

In the pursuit to boost the catalytic properties of SrTiO₃ nanomaterial through surface engineering (SrO terminated and TiO₂ terminated SrTiO₃), we obtained the following results: The surface termination of the SrTiO₃ was mainly characterized by the carbonate layer formation on the SrO termination, which was confirmed by Raman spectroscopy. The Raman spectrum of the TiO₂ terminated SrTiO₃ did not show a carbonate peak, whereas the carbonate peak was observed on SrO terminated SrTiO₃ and untreated SrTiO₃. The TEM image confirmed the layer formation with lattice parameters similar to bulk SrTiO₃. The morphological characterization technique shows that the particle is cuboid with an average size of ~70 nm. The characterization techniques used show that surface engineering by post annealing and hydrothermal etching results in the controlled formation of SrO terminated SrTiO₃ and TiO₂ terminated SrTiO₃ respectively. Nevertheless, the band energy of both the SrO termination and TiO₂ termination samples remains the same as the untreated SrTiO₃, which was confirmed by UV-visible-NIR spectroscopy (Band gap – 3.25 eV). The photocatalytic activity of the surface engineered SrTiO₃ shows that the TiO₂ terminated SrTiO₃ was more effective than SrO terminated SrTiO₃ and untreated SrTiO₃ nanoparticles. The carbonation on the surface of SrO layer apparently blocks the reactive sites for the effective interaction of the nanoparticle and pollutant. To enhance the catalytic activity of the SrTiO₃ against methyl orange and to resolve the rate limiting step in photocatalysis (mass transfer), the catalytic activity of SrTiO₃ nanoparticles was performed with the combination of sono- and photocatalysis. The catalytic activity of TiO₂ terminated SrTiO₃ increases 3.9 times on sonification, which is relatively higher than only photocatalysis without sonification. The sono-photocatalytic activity boosts the mixing and thereby solves one of the limitations of photocatalysis (mass transfer). The results show that increasing the sonification interval increases the catalytic efficiency, the sonification enhances the mixing from 0 to 100s. The immediate increase in the catalytic activity after 100s rather than the saturation might be due to be the activation of sono-catalytic or tribocatalytic mechanism on the degradation of methyl orange against TiO₂ terminated SrTiO₃. As the Goldschmidt tolerance of SrTiO₃ is unity ($t = 1$), the nanoparticle will not show piezocatalysis. To determine the mechanism on the catalysis process causing the sudden hike after 100s, we conducted control experiments including sonification pulse without irradiation and

chopped illumination (alternating the periods of light on and off). Catalysis is a surface phenomenon, the tunable surface engineering allows us to show the change in the catalytic property of the nanomaterial. As a result, it also acts as an indirect tool to determine the surface composition of the SrTiO_3 as to whether it is TiO_2 terminated or SrO terminated. Surface engineering the SrTiO_3 does not affect the band energy of the SrTiO_3 , the first limiting step in catalysis influencing the light harvesting efficiency as well as the photooxidation and photoreduction for the formation of reactive oxygen species (ROS). Therefore, the surface engineering and combination of sono-photocatalysis on SrTiO_3 solves the two main rate limiting step on catalysis namely the surface kinetics and mass transportation.

6.2. Perspectives

The present work is on water decontamination, and on enhancing the catalytic efficiency using a combination of sono- and photocatalysis. Despite the significant progress starting from synthesis to application, some aspects of the study would actually require further investigation. The present work builds on a non-piezoelectric material: the study of a piezo-electric material in combination with photocatalysis should, ideally, even further boost the catalytic activity of the system. Further, the energy band gap of SrTiO_3 is capable of promoting the catalytic production of hydrogen fuel via water splitting. The combination of different catalytic processes with surface engineering to promote the catalytic efficiency of clean energy production can evolve as a strategy to overcome certain limitations currently associated with hydrogen production. As for the tribo-catalytic effect, the influence of concentration impacts the efficiency of mineralization of organic contaminants. It would be effective to compare the parameter that influences the catalytic activity by using polymers like Teflon (fluoro ethylated polymers), which could provide additional boost to the tribo-catalytic proces.

8 REFERENCES

- [1] Y. Huang, F.J. Mi, J. Wang, X.F. Yang, T. Yu, Water pollution incidents and their influencing factors in China during the past 20 years, *Environ Monit Assess*, 194 (2022).
- [2] R.P. Schwarzenbach, T. Egli, T.B. Hofstetter, U. von Gunten, B. Wehrli, *Global Water Pollution and Human Health*, *Annu Rev Env Resour*, 35 (2010) 109-136.
- [3] M. Ismail, K. Akhtar, M.I. Khan, T. Kamal, M.A. Khan, A.M. Asiri, J. Seo, S.B. Khan, *Pollution, Toxicity and Carcinogenicity of Organic Dyes and their Catalytic Bio-Remediation*, *Curr Pharm Design*, 25 (2019) 3645-3663.
- [4] N. Buvaneswari, C. Kannan, *Plant toxic and non-toxic nature of organic dyes through adsorption mechanism on cellulose surface*, *J Hazard Mater*, 189 (2011) 294-300.
- [5] A. Tkaczyk, K. Mitrowska, A. Posyniak, *Synthetic organic dyes as contaminants of the aquatic environment and their implications for ecosystems: A review*, *Sci Total Environ*, 717 (2020).
- [6] J.O. Tijani, O.O. Fatoba, G. Madzivire, L.F. Petrik, *A Review of Combined Advanced Oxidation Technologies for the Removal of Organic Pollutants from Water*, *Water Air Soil Poll*, 225 (2014).
- [7] M.B. Ahmed, J.L. Zhou, H.H. Ngo, W.S. Guo, N.S. Thomaidis, J. Xu, *Progress in the biological and chemical treatment technologies for emerging contaminant removal from wastewater: A critical review*, *J Hazard Mater*, 323 (2017) 274-298.
- [8] J. Rivera-Utrilla, M. Sánchez-Polo, M.A. Ferro-García, G. Prados-Joya, R. Ocampo-Pérez, *Pharmaceuticals as emerging contaminants and their removal from water. A review*, *Chemosphere*, 93 (2013) 1268-1287.

- [9] H. Ghazal, E. Koumaki, J. Hoslett, S. Malamis, E. Katsou, D. Barcelo, H. Jouhara, Insights into current physical, chemical and hybrid technologies used for the treatment of wastewater contaminated with pharmaceuticals, *J Clean Prod*, 361 (2022).
- [10] J. Derco, A.Z. Gotvajn, O. Cizmárová, J. Dudás, L. Sumegová, K. Simovicová, Removal of Micropollutants by Ozone-Based Processes, *Processes*, 9 (2021).
- [11] K. Wenderich, G. Mul, Methods, Mechanism, and Applications of Photodeposition in Photocatalysis: A Review, *Chem Rev*, 116 (2016) 14587-14619.
- [12] V.W. Atul, G.S. Gaikwad, M.G. Dhonde, N.T. Khaty, S.R. Thakare, Removal of Organic Pollutant from Water by Heterogenous Photocatalysis: A Review, *Res J Chem Environ*, 17 (2013) 84-94.
- [13] M. Swedha, S. Balasurya, A. Syed, A. Das, S.S. Khan, Continuous photocatalysis via Z-scheme based nanocatalyst system for environmental remediation of pharmaceutically active compound: Modification, reaction site, defect engineering and challenges on the nanocatalyst, *J Mol Liq*, 353 (2022).
- [14] G. Harini, S. Balasurya, S.S. Khan, Recent advances on gadolinium-based nanophotocatalysts for environmental remediation and clean energy production: Properties, fabrication, defect engineering and toxicity, *J Clean Prod*, 345 (2022).
- [15] J. Ambigadevi, P.S. Kumar, D.V.N. Vo, S.H. Haran, T.N.S. Raghavan, Recent developments in photocatalytic remediation of textile effluent using semiconductor based nanostructured catalyst: A review, *J Environ Chem Eng*, 9 (2021).
- [16] D. Vaya, P.K. Surolia, Semiconductor based photocatalytic degradation of pesticides: An overview, *Environ Technol Inno*, 20 (2020).

- [17] I.C. Amaechi, A.H. Youssef, A. Dörfler, Y. González, R. Katoch, A. Ruediger, Catalytic Applications of Non-Centrosymmetric Oxide Nanomaterials, *Angew Chem Int Edit*, 61 (2022).
- [18] Q. Guo, C.Y. Zhou, Z.B. Ma, X.M. Yang, Fundamentals of TiO₂ Photocatalysis: Concepts, Mechanisms, and Challenges, *Adv Mater*, 31 (2019).
- [19] J. Schneider, M. Matsuoka, M. Takeuchi, J.L. Zhang, Y. Horiuchi, M. Anpo, D.W. Bahnemann, Understanding TiO₂ Photocatalysis: Mechanisms and Materials, *Chem Rev*, 114 (2014) 9919-9986.
- [20] E. Grabowska, Selected perovskite oxides: Characterization, preparation and photocatalytic properties-A review, *Appl Catal B-Environ*, 186 (2016) 97-126.
- [21] X.J. Wen, C.G. Niu, L. Zhang, C. Liang, G.M. Zeng, An in depth mechanism insight of the degradation of multiple refractory pollutants via a novel SrTiO₃/BiOI heterojunction photocatalysts, *J Catal*, 356 (2017) 283-299.
- [22] X. Wang, L. Jiang, K.X. Li, J. Wang, D.W. Fang, Y.C. Zhang, D.M. Tian, Z.H. Zhang, D.D. Dionysiou, Fabrication of novel Z-scheme SrTiO₃/MnFe₂O₄ system with double-response activity for simultaneous microwave-induced and photocatalytic degradation of tetracycline and mechanism insight, *Chem Eng J*, 400 (2020).
- [23] B.G. Anitha, L.G. Devi, Study of reaction dynamics of photocatalytic degradation of 4-chlorophenol using SrTiO₃, sulfur doped SrTiO₃, silver metallized SrTiO₃ and silver metallized sulfur doped SrTiO₃ catalysts: Detailed analysis of kinetic results, *Surf Interfaces*, 16 (2019) 50-58.
- [24] J.S. Padmaja, T.S. Rao, K.V.D. Lakshmi, I.M. Raju, Fabrication of hetero-structured mesoporous TiO₂-SrTiO₃ nanocomposite in presence of Gemini surfactant: Characterization and application in catalytic degradation of Acid Orange, *J Environ Chem Eng*, 6 (2018) 6457-6467.

- [25] G. Mamba, P.J. Mafa, V. Muthuraj, A. Mashayekh-Salehi, S. Royer, T.I.T. Nkambule, S. Rtimi, Heterogeneous advanced oxidation processes over stoichiometric ABO_3 perovskite nanostructures, *Mater Today Nano*, 18 (2022).
- [26] H. Liu, C.Y. Wang, G.X. Wang, Photocatalytic Advanced Oxidation Processes for Water Treatment: Recent Advances and Perspective, *Chem-Asian J*, 15 (2020) 3239-3253.
- [27] C. Byrne, G. Subramanian, S.C. Pillai, Recent advances in photocatalysis for environmental applications, *J Environ Chem Eng*, 6 (2018) 3531-3555.
- [28] J.M. Herrmann, Heterogeneous photocatalysis: fundamentals and applications to the removal of various types of aqueous pollutants, *Catal Today*, 53 (1999) 115-129.
- [29] A. Kumar, P. Raizada, P. Singh, R.V. Saini, A.K. Saini, A. Hosseini-Bandegharai, Perspective and status of polymeric graphitic carbon nitride based Z-scheme photocatalytic systems for sustainable photocatalytic water purification, *Chem Eng J*, 391 (2020).
- [30] A. Mills, C. O'Rourke, K. Moore, Powder semiconductor photocatalysis in aqueous solution: An overview of kinetics-based reaction mechanisms, *J Photoch Photobio A*, 310 (2015) 66-105.
- [31] X. Zong, L.Z. Wang, Ion-exchangeable semiconductor materials for visible light-induced photocatalysis, *J Photoch Photobio C*, 18 (2014) 32-49.
- [32] C.P. Xu, P.R. Anusuyadevi, C. Aymonier, R. Luque, S. Marre, Nanostructured materials for photocatalysis, *Chem Soc Rev*, 48 (2019) 3868-3902.
- [33] S. Klubnuan, S. Suwanboon, P. Amornpitoksuk, Effects of optical band gap energy, band tail energy and particle shape on photocatalytic activities of different ZnO nanostructures prepared by a hydrothermal method, *Opt Mater*, 53 (2016) 134-141.

- [34] R.B.P. Marcelino, C.C. Amorim, Towards visible-light photocatalysis for environmental applications: band-gap engineering versus photons absorption-a review, *Environ Sci Pollut R*, 26 (2019) 4155-4170.
- [35] P. Kanhere, Z. Chen, A Review on Visible Light Active Perovskite-Based Photocatalysts, *Molecules*, 19 (2014) 19995-20022.
- [36] W.S. Koe, J.W. Lee, W.C. Chong, Y.L. Pang, L.C. Sim, An overview of photocatalytic degradation: photocatalysts, mechanisms, and development of photocatalytic membrane, *Environ Sci Pollut R*, 27 (2020) 2522-2565.
- [37] L.X. Wang, J.J. Zhang, Y. Zhang, H.G. Yu, Y.H. Qu, J.G. Yu, Inorganic Metal-Oxide Photocatalyst for H₂O₂ Production, *Small*, 18 (2022).
- [38] S. Balasurya, M.K. Okla, H. AbdElgawad, A.A. AL-ghamdi, M.A. Abdel-Maksoud, S.S. Al-Amri, M.M.Y. Madany, S.S. Khan, Self-propelled nanojets an interfacial Schottky junctions modulated oxygen vacancies enriched for enhanced photo-Fenton degradation of organic contaminant: Improving H₂O₂ generation, Fe³⁺/Fe²⁺ cycle and enhancing plant metabolism, *Chemosphere*, 314 (2023).
- [39] E. Kusmierek, A CeO₂ Semiconductor as a Photocatalytic and Photoelectrocatalytic Material for the Remediation of Pollutants in Industrial Wastewater: A Review, *Catalysts*, 1435 (2022).
- [40] E. Kusmierek, A CeO₂ Semiconductor as a Photocatalytic and Photoelectrocatalytic Material for the Remediation of Pollutants in Industrial Wastewater: A Review, *Catalysts*, 10 (2020).
- [41] A. International, Standard Solar Constant and Zero Air Mass Solar Spectral Irradiance Tables, ASTM International, (2012).

- [42] J. Corredor, M.J. Rivero, C.M. Rangel, F. Gloaguen, I. Ortiz, Comprehensive review and future perspectives on the photocatalytic hydrogen production, *J Chem Technol Biot*, 94 (2019) 3049-3063.
- [43] N.F. Muhamad, R.A.M. Osman, M.S. Idris, M.N.M. Yasin, Physical and electrical properties of SrTiO₃ and SrZrO₃, *Epj Web Conf*, 162 (2017).
- [44] Y. Matsumoto, T. Ohsawa, R. Takahashi, H. Koinuma, Surface termination effect on the photocatalysis on atomically controlled SrTiO₃ (001) surface, *Thin Solid Films*, 486 (2005) 11-14.
- [45] A. Biswas, P.B. Rossen, C.H. Yang, W. Siemons, M.H. Jung, I.K. Yang, R. Ramesh, Y.H. Jeong, Universal Ti-rich termination of atomically flat SrTiO₃ (001), (110), and (111) surfaces, *Appl Phys Lett*, 98 (2011).
- [46] T. Hikita, T. Hanada, M. Kudo, M. Kawai, Surface-Structure of SrTiO₃ (001) with Various Surface Treatments, *J Vac Sci Technol A*, 11 (1993) 2649-2654.
- [47] F. Voigts, C. Argirusis, W. Maus-Friedrichs, The interaction of CO₂ and CO with Fe-doped SrTiO₃ (100) surfaces, *Surf Interface Anal*, 44 (2012) 301-307.
- [48] S. Kuriakose, V. Choudhary, B. Satpati, S. Mohapatra, Facile synthesis of Ag-ZnO hybrid nanospindles for highly efficient photocatalytic degradation of methyl orange, *Phys Chem Chem Phys*, 16 (2014) 17560-17568.
- [49] N.J. Beiarano-Pérez, M.F. Suárez-Herrera, Sonophotocatalytic degradation of congo red and methyl orange in the presence of TiO₂ as a catalyst, *Ultrason Sonochem*, 14 (2007) 589-595.
- [50] A.P. Nagalingam, S.H. Yeo, Effects of ambient pressure and fluid temperature in ultrasonic cavitation machining, *Int J Adv Manuf Tech*, 98 (2018) 2883-2894.

- [51] A.A. Zewde, L.L. Zhang, Z.F. Li, E.A. Odey, A review of the application of sonophotocatalytic process based on advanced oxidation process for degrading organic dye, *Rev Environ Health*, 34 (2019) 365-375.
- [52] M. Pirsaeheb, N. Moradi, A systematic review of the sonophotocatalytic process for the decolorization of dyes in aqueous solution: Synergistic mechanisms, degradation pathways, and process optimization, *J Water Process Eng*, 44 (2021).
- [53] P. Qiu, B. Park, J. Choi, B. Thokchom, A.B. Pandit, J. Khim, A review on heterogeneous sonocatalyst for treatment of organic pollutants in aqueous phase based on catalytic mechanism, *Ultrason Sonochem*, 45 (2018) 29-49.
- [54] N. Shimizu, C. Ogino, M.F. Dadjour, K. Ninomiya, A. Fujihira, K. Sakiyama, Sonocatalytic facilitation of hydroxyl radical generation in the presence of TiO_2 , *Ultrason Sonochem*, 15 (2008) 988-994.
- [55] U.S. Jonnalagadda, Q.W.H. Fan, X.Q. Su, W. Liu, J.J. Kwan, Nanostructured Sonophotocatalysts for spatially controlled inertial cavitation towards energy-efficient sonochemistry, *Chemcatchem*, 14 (2022).
- [56] B. Savun-Hekimoglu, A Review on Sonochemistry and Its Environmental Applications, *Acoustics-Basel*, 2 (2020) 766-775.
- [57] D.J. Flannigan, K.S. Suslick, Plasma formation and temperature measurement during single-bubble cavitation, *Nature*, 434 (2005) 52-55.
- [58] E.E.a.H.B. R. Haghayeghi, Grain refinement of AA5754 aluminum alloy by ultrasonic cavitation: Experimental study and numerical simulation, *Metals and Materials International*, 21 (2015) pages 109–117.

- [59] N. Meng, W. Liu, R.Y. Jiang, Y. Zhang, S. Dunn, J.Y. Wu, H.X. Yan, Fundamentals, advances and perspectives of piezocatalysis: A marriage of solid-state physics and catalytic chemistry, *Prog Mater Sci*, 138 (2023).
- [60] J. González-García, V. Sáez, I. Tudela, M.I. Díez-García, M.D. Esclapez, O. Louisnard, Sonochemical Treatment of Water Polluted by Chlorinated Organocompounds. A Review, *Water-Sui*, 2 (2010) 28-74.
- [61] J. Wang, B.D. Guo, X.D. Zhang, Z.H. Zhang, J.T. Han, J. Wu, Sonocatalytic degradation of methyl orange in the presence of TiO catalysts and catalytic activity comparison of rutile and anatase, *Ultrason Sonochem*, 12 (2005) 331-337.
- [62] H. Lei, M.X. Wu, F. Mo, S.L. Ji, X.P. Dong, Z. Wu, J. Gao, Y. Yang, Y.M. Jia, Tribo-catalytic degradation of organic pollutants through bismuth oxyiodate triboelectrically harvesting mechanical energy, *Nano Energy*, 78 (2020).
- [63] L.Q. Lin, V.G.N. Thyagaraja, R. Ranjith, R.Z. Yang, S. Ciampi, J.M. Chen, J. Liu, Degradation of organic molecules by tribovoltaic mechano-chemistry, *Nano Energy*, 107 (2023).
- [64] B. Yang, H.B. Chen, Y.D. Yang, L. Wang, J.H. Bian, Q.D. Liu, X.J. Lou, Insights into the tribo-/pyro-catalysis using Sr-doped BaTiO₃ ferroelectric nanocrystals for efficient water remediation, *Chem Eng J*, 416 (2021).
- [65] X.X. Wang, Y.M. Jia, Q.C. Zhang, Z. Wu, H.F. Zhang, J.Q. Qi, Harvesting Friction Energy for Tribo-catalytic Degradation of Organic Pollutions via Natural Tourmaline, *Chemistryselect*, 8 (2023).
- [66] Y.Y. Xu, R.Y. Yin, Y.N. Zhang, B.C. Zhou, P.F. Sun, X.P. Dong, Unveiling the Mechanism of Frictional Catalysis in Water by Bi

TiO₂: A Charge Transfer and Contaminant Decomposition Path Study, *Langmuir*, 38 (2022) 14153-14161.

[67] W. Lv, L.J. Kong, S.Y. Lan, J.X. Feng, Y. Xiong, S.H. Tian, Enhancement effect in the piezoelectric degradation of organic pollutants by piezo-Fenton process, *J Chem Technol Biot*, 92 (2017) 152-156.

[68] W.Q. Qian, K. Zhao, D. Zhang, C.R. Bowen, Y.H. Wang, Y. Yang, Piezoelectric Material-Polymer Composite Porous Foam for Efficient Dye Degradation via the Piezo-Catalytic Effect, *Acs Appl Mater Inter*, 11 (2019) 27862-27869.

[69] R.P. Dahl-Hansen, F. Tyholdt, J. Gjessing, A. Vogl, P. Wittendorp, J. Vedum, T. Tybell, On the Effect of Water-Induced Degradation of Thin-Film Piezoelectric Microelectromechanical Systems, *J Microelectromech S*, 30 (2021) 105-115.

[70] J.P. Ma, X. Xiong, D. Wu, Y. Wang, C.G. Ban, Y.J. Feng, J.Z. Meng, X.S. Gao, J.Y. Dai, G. Han, L.Y. Gan, X.Y. Zhou, Band Position-Independent Piezo-Electrocatalysis for Ultrahigh CO₂ Conversion, *Adv Mater*, 35 (2023).

[71] Y.W. Feng, H. Li, L.L. Ling, S. Yan, D.L. Pan, H. Ge, H.X. Li, Z.F. Bian, Enhanced Photocatalytic Degradation Performance by Fluid-Induced Piezoelectric Field, *Environ Sci Technol*, 52 (2018) 7842-7848.

[72] T. Yamaguchi, K. Higashi, A. Regoutz, Y. Takahashi, M. Lazemi, Q.J. Che, F.M.F. de Groot, A. Hariki, Atomic multiplet and charge transfer screening effects in 1s and 2p core-level x-ray photoelectron spectra of early 3d transition-metal oxides, *Physical Review B*, 109 (2024).

[73] F. Bössl, V.C. Menzel, K. Jeronimo, A. Arora, Y.S. Zhang, T.P. Comyn, P. Cowin, C. Kirk, N. Robertson, I. Tudela, Importance of energy band theory and screening charge effect in piezo-electrocatalytical processes, *Electrochim Acta*, 462 (2023).

- [74] S.C. Tu, Y.X. Guo, Y.H. Zhang, C. Hu, T.R. Zhang, T.O.Y. Ma, H.W. Huang, Piezocatalysis and Piezo-Photocatalysis: Catalysts Classification and Modification Strategy, Reaction Mechanism, and Practical Application, *Adv Funct Mater*, 30 (2020).
- [75] X.L. Xu, Z. Wu, L.B. Xiao, Y.M. Jia, J.P. Ma, F.F. Wang, L. Wang, M.S. Wang, H.T. Huang, Strong piezo-electro-chemical effect of piezoelectric BaTiO₃ nanofibers for vibration-catalysis, *J Alloy Compd*, 762 (2018) 915-921.
- [76] Q. Liu, Z.Y. Li, J. Li, F.Q. Zhan, D. Zhai, Q.W. Sun, Z.D. Xiao, H. Luo, D. Zhang, Three dimensional BaTiO₃ piezoelectric ceramics coated with TiO₂ nanoarray for high performance of piezo-photoelectric catalysis, *Nano Energy*, 98 (2022).
- [77] Y. Li, L.L. Shu, Y.C. Zhou, J. Guo, F. Xiang, L. He, H. Wang, Enhanced flexoelectric effect in a non-ferroelectric composite, *Appl Phys Lett*, 103 (2013).
- [78] W.H. Shi, Y.F. Guo, Z.H. Zhang, W.L. Guo, Flexoelectricity in Monolayer Transition Metal Dichalcogenides, *J Phys Chem Lett*, 9 (2018) 6841-6846.
- [79] L. Sai, Y.T. Xiao, F.L. Yan, T. Ying, Z. Wu, H. Xu, Y.M. Jia, F.F. Wang, Integration of hydrogen evolution and dye removal in flexocatalysis by centrosymmetric semiconductor nanorods, *Int J Hydrogen Energ*, 69 (2024) 944-952.
- [80] K. Liu, T. Wu, L.Y. Xu, Z.Z. Zhang, Z.Y. Liu, L.F. Wang, Z.L. Wang, Flexo-photocatalysis in centrosymmetric semiconductors, *Nano Res*, 17 (2024) 1173-1181.
- [81] W.F. Wüst, R. Köber, O. Schlicker, A. Dahmke, Combined zero- and first-order kinetic model of the degradation of TCE and cis-DCE with commercial iron, *Environ Sci Technol*, 33 (1999) 4304-4309.
- [82] D.D. Thongam, H. Chaturvedi, Advances in nanomaterials for heterogeneous photocatalysis, *Nano Express*, 2 (2021).

- [83] A. Sharma, A. Mittal, S. Sharma, K. Kumari, S. Maken, N. Kumar, Cu²⁺-doped α - β phase heterojunctions in Bi₂O₃ nanoparticles for enhanced photocatalytic degradation of organic dye rhodamine B, *Appl Nanosci*, 12 (2022) 151-164.
- [84] X.J. Cao, J.J. Huo, L. Li, J.P. Qu, Y.F. Zhao, W.H. Chen, C.T. Liu, H. Liu, G.X. Wang, Recent Advances in Engineered Ru-Based Electrocatalysts for the Hydrogen/Oxygen Conversion Reactions, *Adv Energy Mater*, 12 (2022).
- [85] S. Abbasi, D. Dastan, S. Talu, M.B. Tahir, M. Elias, L. Tao, Z. Li, Evaluation of the dependence of methyl orange organic pollutant removal rate on the amount of titanium dioxide nanoparticles in MWCNTs-TiO₂ photocatalyst using statistical methods and Duncan's multiple range test, *Int J Environ an Ch*, (2022).
- [86] S. Saha, T.P. Sinha, A. Mookerjee, Structural and optical properties of paraelectric SrTiO₃, *J Phys-Condens Mat*, 12 (2000) 3325-3336.
- [87] A. Ohtomo, H.Y. Hwang, A high-mobility electron gas at the LaAlO₃/SrTiO₃ heterointerface (vol 427, pg 423, 2004), *Nature*, 441 (2006) 120-120.
- [88] M. Irshad, Q.T. Ain, M. Zaman, M.Z. Aslam, N. Kousar, M. Asim, M. Rafique, K. Siraj, A.N. Tabish, M. Usman, M.U. Farooq, M.A. Assiri, M. Imran, Photocatalysis and perovskite oxide-based materials: a remedy for a clean and sustainable future, *Rsc Adv*, 12 (2022) 7009-7039.
- [89] S. Ramos-Terrón, A.D. Jodlowski, C. Verdugo-Escamilla, L. Camacho, G. de Miguel, Relaxing the Goldschmidt Tolerance Factor: Sizable Incorporation of the Guanidinium Cation into a Two-Dimensional Ruddlesden-Popper Perovskite, *Chem Mater*, 32 (2020) 4024-4037.
- [90] P. Goudochnikov, A.J. Bell, Correlations between transition temperature, tolerance factor and cohesive energy in 2⁺:4⁺perovskites, *J Phys-Condens Mat*, 19 (2007).

- [91] F.V.E. Hensling, C. Baeumer, M.A. Rose, F. Gunkel, R. Dittmann, SrTiO₃ termination control: a method to tailor the oxygen exchange kinetics, *Mater Res Lett*, 8 (2020) 31-40.
- [92] S. Thapa, S.R. Provence, D. Jessup, J. Lapano, M. Brahlek, J.T. Sadowski, P. Reinke, W.C. Jin, R.B. Comes, Correlating surface stoichiometry and termination in SrTiO₃ films grown by hybrid molecular beam epitaxy, *Journal of Vacuum Science & Technology A*, 39 (2021).
- [93] J.D.S. H. Choi, K. R. Lee, S. Kim, Correlated Visible-Light Absorption and Intrinsic Magnetism of SrTiO₃ Due to Oxygen Deficiency: Bulk or Surface Effect? , *Inorganic Chemistry*, 8 (2015) 3759–3765.
- [94] Y.S. Xu, Y.H. Liang, Q.Q. He, R.L. Xu, D.C. Chen, X.J. Xu, H.W. Hu, Review of doping SrTiO₃ for photocatalytic applications, *B Mater Sci*, 46 (2022).
- [95] Y.X. Song, W.Q. Ma, J.J. Chen, J. Xu, Z.Y. Mao, D.J. Wang, Photocatalytic activity of perovskite SrTiO₃ catalysts doped with variable rare earth ions, *Rare Metals*, 40 (2021) 1077-1085.
- [96] S. Patial, V. Hasija, P. Raizada, P. Singh, A.A.P.K. Singh, A.M. Asiri, Tunable photocatalytic activity of SrTiO₃ for water splitting: Strategies and future scenario, *J Environ Chem Eng*, 8 (2020).
- [97] Z.J. Chi, L.X. Yan, Z. Zhang, Z. Zhou, L.M. Zheng, D. Wang, Q.L. Tian, W. Wang, Z. Nie, J. Zhang, Y.C. Du, J.F. Hua, J.R. Shi, C.H. Pai, W. Lu, W.H. Huang, H.B. Chen, C.X. Tang, Diffraction based method to reconstruct the spectrum of the Thomson scattering x-ray source, *Rev Sci Instrum*, 88 (2017).
- [98] A. Ali, Y.W. Chiang, R.M. Santos, X-ray Diffraction Techniques for Mineral Characterization: A Review for Engineers of the Fundamentals, Applications, and Research Directions, *Minerals-Basel*, 12 (2022).
- [99] B.D.C.a.S.R. Stock, *Elements of X-Ray Diffraction*, Prentice Hall, (2001).

- [100] A.A. Makki, F. Bonnier, R. Respaud, F. Chtara, A. Tfayli, C. Tauber, D. Bertrand, H.J. Byrne, E. Mohammed, I. Chourpa, Qualitative and quantitative analysis of therapeutic solutions using Raman and infrared spectroscopy, *Spectrochim Acta A*, 218 (2019) 97-108.
- [101] M. Abu Bakkar, H. Nawaz, M.I. Majeed, A. Naseem, A. Ditta, N. Rashid, S. Ali, J. Bajwa, S. Bashir, S. Ahmad, H. Hyat, K.S. Bukhari, F. Bonnier, Raman spectroscopy for the qualitative and quantitative analysis of solid dosage forms of Sitagliptin, *Spectrochim Acta A*, 245 (2021).
- [102] F. Wan, L.L. Du, W.G. Chen, P.Y. Wang, J.X. Wang, H.Y. Shi, A Novel Method to Directly Analyze Dissolved Acetic Acid in Transformer Oil without Extraction Using Raman Spectroscopy, *Energies*, 10 (2017).
- [103] Y.X. Luo, X.L. Yang, T.L. Feng, J.Y. Wang, X.L. Ruan, Vibrational hierarchy leads to dual-phonon transport in low thermal conductivity crystals, *Nat Commun*, 11 (2020).
- [104] S.M. Zhu, C.Z. Fan, P. Ding, E.J. Liang, H.W. Hou, Y.D. Wu, Theoretical investigation of a plasmonic substrate with multi-resonance for surface enhanced hyper-Raman scattering, *Sci Rep-Uk*, 8 (2018).
- [105] B. Lee, S. Yoon, J.W. Lee, Y. Kim, J. Chang, J. Yun, J.C. Ro, J.S. Lee, J.H. Lee, Statistical Characterization of the Morphologies of Nanoparticles through Machine Learning Based Electron Microscopy Image Analysis, *Acs Nano*, 14 (2020) 17125-17133.
- [106] D.M. Maher, D.C. Joy, Formation and Interpretation of Defect Images from Crystalline Materials in a Scanning-Transmission Electron-Microscope, *Ultramicroscopy*, 1 (1976) 239-253.
- [107] X.L. Wei, S. Wang, Q. Chen, L.M. Peng, Breakdown of Richardson's Law in Electron Emission from Individual Self-Joule-Heated Carbon Nanotubes, *Sci Rep-Uk*, 4 (2014).

- [108] D.N.G. Krishna, J. Philip, Review on surface-characterization applications of X-ray photoelectron spectroscopy (XPS): Recent developments and challenges, *Appl Surf Sci Adv*, 12 (2022).
- [109] B.J. Schultz, R.V. Dennis, V. Lee, S. Banerjee, An electronic structure perspective of graphene interfaces, *Nanoscale*, 6 (2014) 3444-3466.
- [110] R.A. Schoonheydt, UV-VIS-NIR spectroscopy and microscopy of heterogeneous catalysts, *Chem Soc Rev*, 39 (2010) 5051-5066.
- [111] F.S. Rocha, A.J. Gomes, C.N. Lunardi, S. Kaliaguine, G.S. Patience, Experimental methods in chemical engineering: Ultraviolet visible spectroscopy-UV-Vis, *Can J Chem Eng*, 96 (2018) 2512-2517.
- [112] G. Yang, S.J. Park, Conventional and Microwave Hydrothermal Synthesis and Application of Functional Materials: A Review, *Materials*, 12 (2019).
- [113] S. Komarneni, Nanophase materials by hydrothermal, microwave-hydrothermal and microwave-solvothermal methods, *Curr Sci India*, 85 (2003) 1730-1734.
- [114] R. Krishnan, S.N. Shibu, D. Poelman, A.K. Badyal, A.K. Kunti, H.C. Swart, S.G. Menon, Recent advances in microwave synthesis for photoluminescence and photocatalysis, *Mater Today Commun*, 32 (2022).
- [115] J. Livage, M. Henry, C. Sanchez, Sol-Gel Chemistry of Transition-Metal Oxides, *Prog Solid State Ch*, 18 (1988) 259-341.
- [116] T. Hikita, T. Hanada, M. Kudo, M. Kawai, Structure and Electronic State of the TiO₂ and SrO Terminated SrTiO₃(100) Surfaces, *Surf Sci*, 287 (1993) 377-381.
- [117] F.T.L. Muniz, M.A.R. Miranda, C.M. dos Santos, J.M. Sasaki, The Scherrer equation and the dynamical theory of X-ray diffraction, *Acta Crystallogr A*, 72 (2016) 385-390.

- [118] D.A. Tenne, A.K. Farrar, C.M. Brooks, T. Heeg, J. Schubert, H.W. Jang, C.W. Bark, C.M. Folkman, C.B. Eom, D.G. Schlom, Ferroelectricity in nonstoichiometric SrTiO₃ films studied by ultraviolet Raman spectroscopy, *Appl Phys Lett*, 97 (2010).
- [119] M. Bakhtbidar, I. Amaechi, A. Doerfler, A. Merlen, A. Ruediger, Direct Observation of Carbonate Chemisorption on Barium Titanate Surfaces by Tip-Enhanced Raman Spectroscopy, *Adv Mater Interfaces*, 11 (2024).
- [120] Y.L. Tang, Y.L. Zhu, B. Wu, Y.J. Wang, L.X. Yang, Y.P. Feng, M.J. Zou, W.R. Geng, X.L. Ma, Periodic Polarization Waves in a Strained, Highly Polar Ultrathin SrTiO₃, *Nano Lett*, 21 (2021) 6274-6281.
- [121] M. Lee, X.L. Tan, M. Yoneda, T. Okamoto, I. Tanaka, Y. Higa, D.W. Peng, M. Ogi, S. Kobayashi, M. Taguchi, M. Lippmaa, M.J. Casanove, H. Daimon, Distortion Analysis of Ir- and Co-doped LaAlO₃/SrTiO₃ (001) Interfaces by Hard X-ray Photoelectron Diffraction, *J Phys Soc Jpn*, 87 (2018).
- [122] J.B. Coulter, D.P. Birnie, Assessing Tauc Plot Slope Quantification: ZnO Thin Films as a Model System, *Phys Status Solidi B*, 255 (2018).
- [123] D. Kumar, R.C. Budhani, Defect-induced photoluminescence of strontium titanate and its modulation by electrostatic gating, *Physical Review B*, 92 (2015).
- [124] H. Shen, X.Y. Shi, Z. Wang, Z.Y. Hou, C.L. Xu, L.B. Duan, X.R. Zhao, H.J. Wu, Defects control and origins of blue and green emissions in sol-gel ZnO thin films, *Vacuum*, 202 (2022).
- [125] M.B. Johnston, L.M. Herz, Hybrid Perovskites for Photovoltaics: Charge-Carrier Recombination, Diffusion, and Radiative Efficiencies, *Accounts Chem Res*, 49 (2016) 146-154.

- [126] A. Staykov, S. Fukumori, K. Yoshizawa, K. Sato, T. Ishihara, J. Kilner, Interaction of SrO-terminated SrTiO₃ surface with oxygen, carbon dioxide, and water, *J Mater Chem A*, 6 (2018) 22662-22672.
- [127] I. Yamada, A. Takamatsu, H. Ikeno, Complementary evaluation of structure stability of perovskite oxides using bond-valence and density-functional-theory calculations, *Sci Technol Adv Mat*, 19 (2018) 101-107.
- [128] K.S. Suslick, Sonochemistry, *Science*, 247 (1990) 1439-1445.
- [129] B.L. Cheng, Q. Xu, Y.Q. Ding, S. Bai, X.F. Jia, Y.D.C. Yu, J. Wen, Y. Qin, High performance temperature difference triboelectric nanogenerator, *Nat Commun*, 12 (2021).
- [130] L.M. Bai, S. Wang, Z.Y. Wang, E.L. Hong, Y. Wang, C.H. Xia, B.Q. Wang, Kinetics and mechanism of photocatalytic degradation of methyl orange in water by mesoporous Nd-TiO₂-SBA-15 nanocatalyst, *Environ Pollut*, 248 (2019) 516-525.
- [131] N. Pourshirband, A. Nezamzadeh-Ejhi, S.N. Mirsattari, The CdS/g-C₃N₄ nano-photocatalyst: Brief characterization and kinetic study of photodegradation and mineralization of methyl orange, *Spectrochim Acta A*, 248 (2021).
- [132] N.A.S. Ridha, H.K. Egzar, N.M. Kamal, Synthesis and Characterization of CuO Nanoparticles and TiO₂/CuO Nanocomposite and Using them as Photocatalysts, *Aip Conf Proc*, 2290 (2020).
- [133] U.S.U. Thampy, A. Mahesh, K.S. Sibi, I.N. Jawahar, V. Biju, Enhanced photocatalytic activity of ZnO-NiO nanocomposites synthesized through a facile sonochemical route, *Sn Appl Sci*, 1 (2019).
- [134] S. Salamat, H. Younesi, N. Bahramifar, Synthesis of magnetic core-shell Fe

O

@TiO

nanoparticles from electric arc furnace dust for photocatalytic degradation of steel mill wastewater, *Rsc Adv*, 7 (2017) 19391-19405.

[135] S.K. Godlaveeti, S.K. Arla, K. Thippana, K.A. Alrashidi, S. Mohammad, S.W. Joo, A.R. Somala, Tailoring Photocatalytic Degradation Efficiency of ZnO Nanorods for Methyl Orange Dye Removal: Unveiling Key Parameters and Performance Optimization, *Bionanoscience*, (2024).

[136] J. Han, B.M. Jun, J. Heo, S. Kim, Y. Yoon, C.M. Park, Heterogeneous sonocatalytic degradation of an anionic dye in aqueous solution using a magnetic lanthanum dioxide carbonate-doped zinc ferrite-reduced graphene oxide nanostructure, *Ecotox Environ Safe*, 182 (2019).

[137] S.G. Babu, P. Karthik, M.C. John, S.K. Lakhera, M. Ashokkumar, J. Khim, B. Neppolian, Synergistic effect of sono-photocatalytic process for the degradation of organic pollutants using CuO-TiO₂/rGO, *Ultrason Sonochem*, 50 (2019) 218-223.

COMPARAISON DES MÉCANISMES CATALYTIQUES DE DIFFÉRENTES TERMINAISONS DE SURFACE DU TITANATE DE STRONTIUM POUR LA DÉGRADATION DES POLLUANTS ORGANIQUES

Résumé en Français

1. Introduction

Au cours de la dernière décennie, la contamination de l'eau a connu une augmentation significative au niveau mondial et pourrait entraîner une pénurie d'eau douce, principalement due à l'urbanisation rapide au cours de la dernière décennie [1-3]. La principale source de contamination de l'eau est due à l'éjection d'effluents toxiques (colorants, pigments, pesticides, produits pharmaceutiques, etc.) dans les masses d'eau de l'environnement, ce qui entraîne des effets dangereux pour l'homme et les organismes aquatiques en affectant la chaîne alimentaire de l'environnement [3-5]. Il est essentiel de traiter les effluents avant de les rejeter dans les masses d'eau. Selon la littérature disponible, les technologies existantes pour l'élimination ou la décontamination des polluants toxiques sont l'adsorption, l'osmose, l'ozonation, le charbon actif, la photolyse (avec UV et H_2O_2) et d'autres processus d'oxydation avancés [6-10]. La photocatalyse a attiré les chercheurs au fil du temps en raison de ses propriétés étendues dans la conversion de l'énergie solaire en énergie chimique. La photocatalyse est un processus d'oxydation avancé, dans lequel le nanomatériau est excité par l'énergie solaire en vue de la formation de radicaux libres pour la minéralisation des polluants toxiques. [11-14]. La catalyse est largement utilisée dans les techniques de traitement de l'eau à grande échelle dans les industries pour endommager efficacement les liaisons avec les polluants et réduire ainsi la toxicité de l'effluent. Les métaux abondants dans la terre ont été étudiés, notamment les métaux rares et les catalyseurs à base de métaux nobles, en tant que matériaux rentables pour une minéralisation efficace des polluants toxiques dans le traitement de l'eau [15, 16]. Le nanomatériau à base de semi-conducteur a été largement utilisé comme nano photocatalyseur, car il est efficace dans la collecte de la lumière pour la séparation des charges, la principale étape limitant la vitesse étant le transfert de masse dans la catalyse.

On ne peut pas exclure complètement la technique existante, les inconvénients au niveau de la toxicité qui conduit à des maladies d'origine hydrique. Les matériaux à base de TiO_2 ont été largement utilisés pour le traitement catalytique de l'eau, car ils sont relativement non toxiques et possèdent de grandes propriétés de collecte de la lumière [17, 18]. Cela a conduit au développement de nanomatériaux à base de pérovskite (ABO_3 - B est le titane) qui influencent

l'efficacité de la dégradation catalytique des polluants [19]. Le titanate de strontium SrTiO₃, qui possède une structure de pérovskite (ABO²⁺⁴⁺²⁻), est un matériau intéressant à cet égard avec le mécanisme actuel et présente une bande d'énergie plus importante [20-23]. SrTiO₃ présente des couches empilées alternées de SrO et de TiO₂ le long du plan (001). La catalyse étant un phénomène de surface, l'ingénierie de surface de SrTiO₃ tend à attribuer différentes propriétés d'activité catalytique, l'efficacité dépendant à peine du site réactif du nanomatériau. La combinaison de différents processus catalytiques peut résoudre l'étape limitant la vitesse, ce qui augmente l'efficacité catalytique de la nanoparticule. Techniquement, l'ingénierie de surface et la combinaison peuvent stimuler l'efficacité catalytique avec un nanomatériau respectueux de l'environnement pour la dégradation catalytique des polluants toxiques pour le traitement de l'eau.

1.2 Objectifs

Les objectifs généraux de la thèse sont : (1) l'ingénierie de surface des nanoparticules SrTiO₃ sur la formation de terminaisons SrO et TiO₂, (2) l'étude de l'efficacité catalytique des différentes terminaisons sur la dégradation de l'orange de méthyle. (3) l'effet de la sonification pour stimuler le transport de masse pour un processus catalytique efficace pour le traitement de l'eau.

1.3. Étape limitant la vitesse de la photocatalyse

Le facteur primitif limitant la vitesse peut être déterminé comme l'utilisation du nanomatériau souhaitable, qui dépend à peine de la bande interdite du matériau qui peut exciter l'électron à l'énergie photonique donnée. La partie inefficace de la photocatalyse est le transport de masse de la paire e⁻/h⁺, qui peut être considéré comme l'étape limitant la vitesse d'une réaction photocatalytique. En fait, le photovoltaïque et la photocatalyse sont considérés comme des phénomènes physiques similaires dans les nanomatériaux. Dans le cas de la photovoltaïque, le nanomatériau est irradié par la lumière, puis connecté à un circuit externe pour la conversion de l'énergie lumineuse en énergie électrique (cellule solaire), tandis que dans le cas de la photocatalyse, le nanomatériau est irradié par la lumière, puis les porteurs de charge s'adsorbent sur la formation de radicaux pour la conversion chimique. La photovoltaïque est un processus de conversion de l'énergie lumineuse en énergie électrique et la photocatalyse est la conversion de l'énergie lumineuse en énergie chimique. Le rendement de conversion de l'énergie photovoltaïque est de 10⁻¹ et le rendement de conversion de la photocatalyse est de 10⁻⁶.

1.4. Efficacité de conversion - photocatalyse

$$Energy\ in = P_{total} \left(\frac{W}{m^2} \right) \times Area\ (m^2) \times time(s)$$

L'énergie entrante : 1 heure de 1 kW/m² sur 1 m² = 3600 kJ = 3,6 x 10⁶ J

L'énergie sortante : la minéralisation de 1 mM de polluant (p. ex. méthylène orange 327g/mol) sur une durée d'une heure et 1 m² est donnée par la formule suivante

- Chaque liaison rompue est de l'ordre de 1eV

- 1 mM de liaisons rompues : $1 \text{ eV} \times 6 \times 10^{23} \times 10^{-3} = 96 \text{ J/mmol}$

$$\text{Conversion efficiency} = \frac{\text{energy out}}{\text{energy in}}$$

L'efficacité de la dégradation de 1 mM d'orange de méthyle en 1 heure avec un soleil de puissance est de 2×10^{-6} .

Ici, il est clairement indiqué que le transfert de charge efficace et la désorption des polluants après minéralisation sont considérés comme l'étape limitant la vitesse de la photocatalyse.

2. La méthodologie

2.1. Synthèse de SrTiO₃

La méthode micro-ondes-hydrothermique a été employée pour la synthèse chimique des nanoparticules SrTiO₃ (STO NPs). Tout d'abord, 0,45 g de butoxyde de titane (Ti(CH₃CH₂CH₂CH₂O)₄) a été ajouté à 10 ml d'eau distillée. 2 mL d'hydroxyde d'ammonium (NH₄ OH) ont été ajoutés au mélange réactionnel ci-dessus pour atteindre un pH de 14. Enfin, 0,6 g d'hydroxyde de strontium (Sr(OH)₂) a été ajouté au mélange réactionnel, puis agité à 80° C pendant 20 minutes pour obtenir une solution homogène. Le mélange réactionnel a été transféré dans l'autoclave à ligne en Téflon, puis déplacé dans le dispositif de digestion acide en PTFE pour micro-ondes et la réaction hydrothermique a été effectuée à 120 W (2,5 GHz) pendant 7 minutes pour la formation effective de SrTiO₃. Les NP préparées ont été recueillies par précipitation, puis lavées deux fois avec de l'éthanol, de l'eau et séchées à 80° C pendant 16 h. Les NPs ont été recuites à 1000° C pendant 2 h, avec une vitesse de chauffage de 20° C/min.

La terminaison SrO sur les NP de SrTiO₃ a été obtenue par recuit. Ici, 0,2 g de SrTiO₃ synthétisé a été recuit à 900° C pendant 2 h avec une vitesse de chauffage de 20° C/min. La terminaison TiO₂ sur les NPs SrTiO₃ a été obtenue par gravure hydrothermale. La terminaison TiO₂ sur SrTiO₃ a été synthétisée par gravure hydrothermale. Tout d'abord, le SrTiO₃ préparé (0,2 g) a été ajouté à 12 mL d'eau et le mélange réactionnel a été transféré dans l'autoclave à conduite en téflon, puis placé dans le PTFE à digestion acide par micro-ondes, la réaction hydrothermique a été effectuée à 120 W (2,5 GHz) pendant 7 min. Ensuite, les NPs préparées ont été recueillies par précipitation, puis lavées deux fois avec de l'éthanol, de l'eau et séchées à 80° C pendant 16 h pour obtenir des TiO₂ terminés par des SrTiO₃.

2.2. Expérience photocatalytique

L'activité photocatalytique des NPs SrTiO₃ (terminées par SrO et TiO₂) a été testée contre l'orange de méthyle (MO) comme polluant modèle. Tout d'abord, 50 mg/L de NPs SrTiO₃ (terminées par SrO et TiO₂) et 10 mg/L d'orange de méthyle ont été soniqués dans un bain-marie pendant 20 min à température ambiante et le mélange réactionnel a été agité dans l'obscurité pendant 30 min. Ensuite, le mélange réactionnel a été irradié à la lumière (100 mW/cm²) et la transmittance a été enregistrée. Toutes les expériences ont été réalisées en triple afin de déterminer l'écart-type et de négliger les sources d'erreur et la reproductibilité.

2.3. Spectroscopie Raman

L'analyse structurale et les propriétés optiques du nanomatériau préparé ont été déterminées par spectroscopie Raman en se basant sur la vibration moléculaire et l'interaction photon-phonon (Fig. 1). Les spectres Raman de SrTiO₃ (terminés par SrO et TiO₂) et de SrTiO₃ non traité sont présentés dans la figure 22. Les résultats montrent que tous les échantillons présentent un pic Raman à 175 cm⁻¹, correspondant à LO1 et TO2, 266 cm⁻¹ correspondant à TO3 et LO2 ; 474 cm⁻¹, 545 cm⁻¹ et 795 cm⁻¹ qui correspondent à LO3, TO4 et LO4 respectivement. [96]. L'émission de phonons est le pic Raman de premier ordre. En outre, le pic à 1052 cm⁻¹ correspond au carbonate qui a été observé dans le SrTiO₃ terminé par SrO et le SrTiO₃ non traité et il n'a pas été observé dans le SrTiO₃ terminé par le TiO₂. Le pic de carbonate s'explique par l'adsorption du carbonate sur la couche de SrO, ce qui entraîne la formation de Sr(CO₃). Cela montre que la gravure hydrothermale élimine la couche de SrO et entraîne la formation de le SrTiO₃ terminé par le TiO₂.

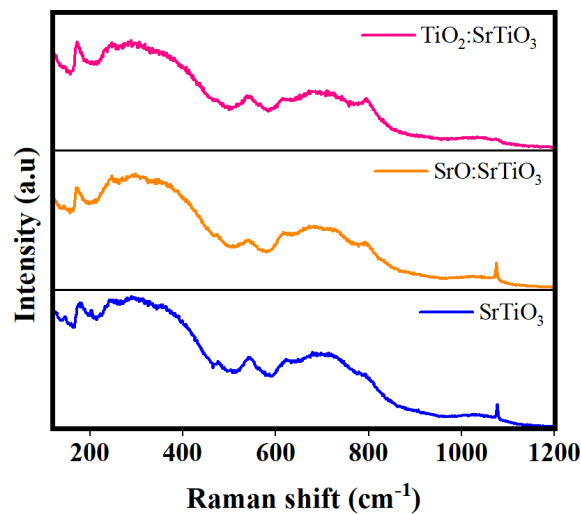


Fig. 1. Mesure par spectroscopie Raman de SrTiO₃ .

2.4. Photocatalyse

L'activité photocatalytique des NPs SrTiO₃ (terminées par SrO et TiO₂) a été déterminée par la photodégradation de l'orange de méthyle. Ici, le mélange des NPs SrTiO₃ (terminées par SrO et TiO₂) : orange de méthyle (50 : 10 mg/L) a été agité pendant 30 min pour atteindre l'équilibre d'adsorption et de désorption, irradié avec une intensité constante de 100 mW/cm². Le mélange réactionnel a ensuite été irradié et la transmittance a été enregistrée à des intervalles de temps aléatoires. L'efficacité de la dégradation photocatalytique du SrTiO₃ non traité, du SrTiO₃ terminé par du SrO et du SrTiO₃ terminé par du TiO₂ a été calculée pour être de 32,6± 1,6 % et de 94± 1,6 % en 120 min, l'activité photocatalytique du SrTiO₃ sans ingénierie de surface a été calculée pour être de 25,35± 0,9 % (Fig. 2). L'efficacité de la dégradation de l'orange de méthyle par le SrTiO₃ terminé par TiO₂ était trois fois plus élevée que le SrTiO₃ terminé par SrO (tableau 1). La cinétique de vitesse de la dégradation photocatalytique de l'orange de méthyle par les NPs SrTiO₃ (terminées par SrO et TiO₂) a été calculée par Eq. 1.

$$\ln\left(\frac{C}{C_0}\right) = kt \quad (1)$$

où C et C₀ représentent la transmittance au temps t=0 et au temps 't'. Ici, la photodégradation de l'orange de méthyle suit la réaction cinétique du pseudo-premier ordre avec des constantes de vitesse de 0,004 (NPs SrTiO₃ terminées par SrO), 0,015 (NPs SrTiO₃ terminées par TiO₂) et 0,002 (SrTiO₃ sans traitement de surface) avec un coefficient de régression de <0,95 (Fig. 2). Le taux de dégradation de l'orange de méthyle par le SrTiO₃ terminé par TiO₂ était 0,38 fois plus élevé que le SrTiO₃ terminé par SrO et 0,75 fois plus élevé que le SrTiO₃ sans traitement de surface (Tableau. 1). Les résultats montrent que l'activité catalytique du SrTiO₃ terminé par TiO₂ était plus élevée que celle du SrTiO₃ terminé par SrO et du SrTiO₃ non traité (sans ingénierie de surface).

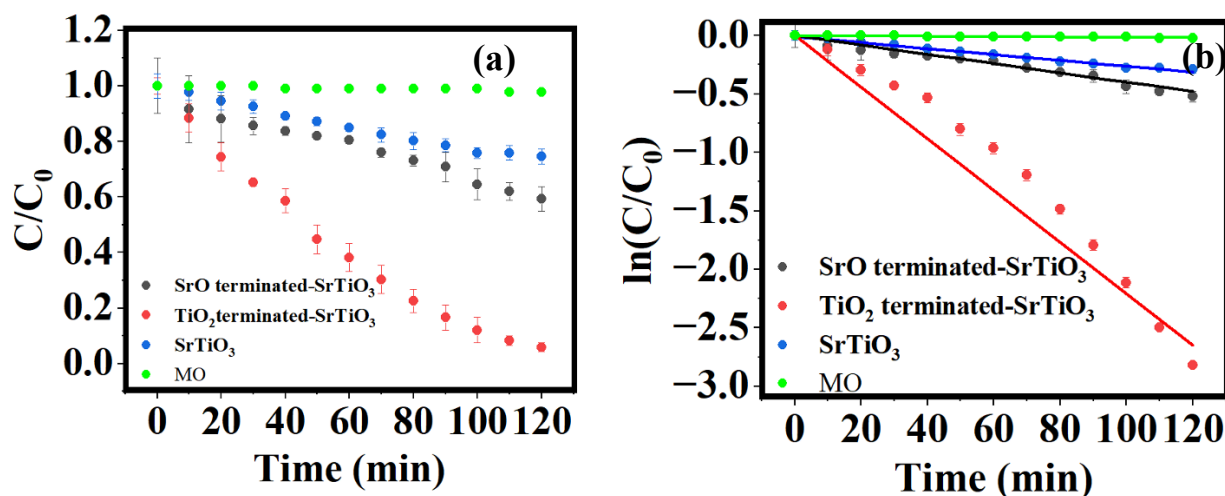


Fig. 2. Tracé de C/C_0 (a) et de $\ln(C/C_0)$ (b) sur la dégradation photocatalytique de l'orange de méthyle par les nanoparticules $SrTiO_3$

Tableau. 1. Constante de vitesse et pourcentage de dégradation de l'orange de méthyle contre $SrTiO_3$ (photocatalyse)

S/N	Photocatalyse	$SrTiO_3:TiO_2$	$SrTiO_3:SrO$	$SrTiO_3$
1	Constante de vitesse (min^{-1})	0,015	0,004	0,002
2	Dégradation (%)	$94 \pm 1,6$	$32,6 \pm 1,6$	$25,35 \pm 0,9$

2.5. Sono-photocatalyse

Pour stimuler l'activité catalytique du $SrTiO_3$ contre l'orange de méthyle et résoudre l'étape limitant le taux de photocatalyse (transfert de masse), l'activité catalytique des nanoparticules de $SrTiO_3$ a été réalisée en combinant l'impulsion de sonification et le système d'irradiation. En bref, le mélange de réaction $SrTiO_3$ (TiO_2 terminé) NPs : méthyl orange (50 : 10 mg/L) a été agité pendant 30 minutes pour atteindre l'équilibre d'adsorption et de désorption. Ensuite, le mélange réactionnel a été irradié sous 100 mW/cm^2 avec l'introduction d'une impulsion de sonification (0 à 300 secondes), l'irradiation solaire étant coupée pendant l'impulsion de sonification. La transmittance du mélange réactionnel a été déterminée par le dispositif spectrophotométrique à des intervalles de temps aléatoires (Fig. 3a). Le graphique de la concentration relative de l'orange de méthyle sur le photoblanchiment montre que le pourcentage de photocatalyse en présence de

sonification augmente de 63,3 à 94,4 % sous 60 minutes d'irradiation (Tableau 2). Le taux de dégradation photocatalytique de l'orange de méthyle contre le SrTiO₃ terminé par TiO₂ avec différentes impulsions de sonification suit une cinétique de pseudo-premier ordre (Fig. 3b). Le taux de dégradation de l'orange de méthyle contre le SrTiO₃ terminé par TiO₂ sous différentes impulsions de sonification augmente de 0,015 à 0,059 min⁻¹ (Tableau. 2). Les résultats montrent que l'activité catalytique du SrTiO₃ terminé par TiO₂ augmente de 3,9 fois avec l'impulsion de sonification, ce qui est relativement plus élevé que la photocatalyse sans sonification.

Tableau. 2. Constante de vitesse et pourcentage de dégradation de l'orange de méthyle contre SrTiO₃ terminé par TiO₂ (sono-photocatalyse)

S/N	Impulsion (s)	Constante de vitesse (min ⁻¹)	Taux de dégradation (%)
1	0	0,015	63,3± 1,33
2	6	0,017	66,9± 0,81
3	18	0,018	68,2± 0,86
4	30	0,020	71,5± 0,98
5	60	0,021	76,1± 1,03
6	100	0,048	81,2± 1,96
7	300	0,056	89,2± 2,02
8	600	0,059	94,4± 1,17

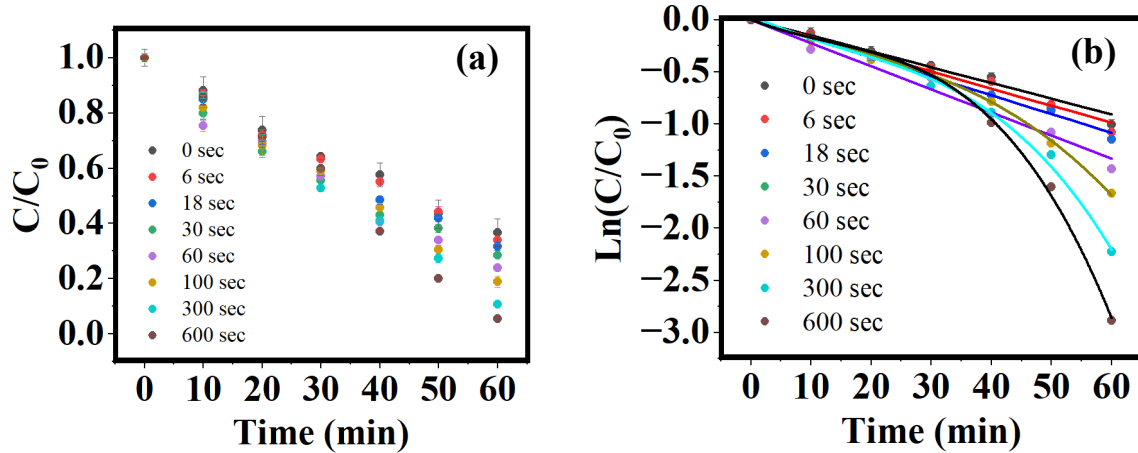


Fig. 3. Tracé de C/C_0 (a) et de $\ln(C/C_0)$ (b) sur la dégradation sono-photocatalytique de l'orange de méthyle par des nanoparticules de SrTiO_3 terminées par TiO_2

Le tracé du taux de dégradation catalytique de l'orange de méthyle en fonction de l'impulsion de sonification est illustré à la figure 4. Les tracés suivent la dégradation exponentielle de l'orange de méthyle avec une augmentation de l'impulsion de sonification de 0 à 100 secondes et une augmentation soudaine de l'activité catalytique avec une augmentation de l'impulsion de 100 à 300 secondes. Le tracé a été ajusté avec la fonction exponentielle de dégradation de l'orange de méthyle et a été donné par Eq. 3.

$$y = f(x) = a(1 - \exp(-\frac{x-b}{c})) + m \times x \quad (3)$$

où $m \times x$ représente l'augmentation régulière après une impulsion de 100 secondes (m est la pente). Les résultats montrent que l'impulsion de sonification augmente l'efficacité catalytique, la sonification améliore le mélange de 0 à 100 secondes. L'augmentation immédiate de l'activité catalytique après 100 secondes plutôt que la saturation pourrait être due à l'activation du mécanisme sonocatalytique ou tribocatalytique sur la dégradation de l'orange de méthyle contre le SrTiO_3 terminé par le TiO_2 . Comme la tolérance de Goldschmidt de SrTiO_3 est égale à l'unité ($t = 1$), la nanoparticule ne se développera pas par catalyse piézoélectrique [101].

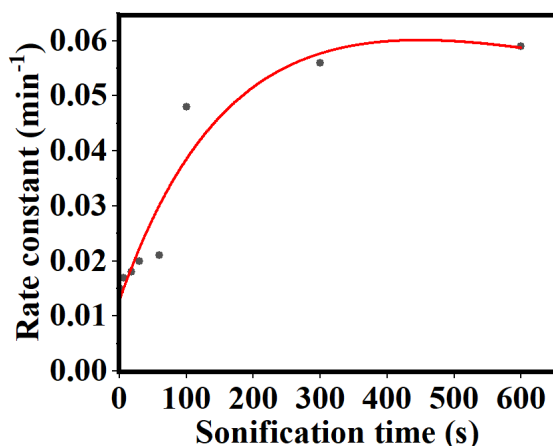


Fig. 4. Tracé du taux de réaction de l'activité sono-photocatalytique en fonction de l'impulsion de sonification sur la dégradation catalytique de l'orange de méthyle contre SrTiO₃ terminé par TiO₂

De même, l'activité sono-photocatalytique des nanoparticules de SrTiO₃ terminées par du SrO et de SrTiO₃ non traitées a été réalisée à 600 secondes et illustrée dans la Fig. 5. Les résultats montrent que la dégradation est plus efficace avec le SrTiO₃ terminé par le TiO₂ qu'avec le SrO terminé par le SrTiO₃ et les nanoparticules de SrTiO₃ non traitées (Fig. 5). La vitesse de dégradation des nanoparticules de SrTiO₃ terminées par du SrO et de SrTiO₃ non traitées était 2,16 fois et 1,6 fois plus faible que celle des nanoparticules de SrTiO₃ terminées par du TiO₂ (Tableau 3). En comparaison avec l'expérience de photocatalyse et de sono-photocatalyse, l'augmentation de l'efficacité de la catalyse était ordonnée comme suit : SrTiO₃ terminé par TiO₂ > SrTiO₃ terminé par SrO > SrTiO₃ non traité pour la photocatalyse, tandis que l'efficacité de la catalyse était classée comme suit : SrTiO₃ terminé par TiO₂ > SrO non traité > SrTiO₃ terminé par SrO pour la sono-photocatalyse. L'activité plus faible du SrTiO₃ terminé par du SrO est due à la formation de Sr(CO₃), qui bloque les sites réactifs pour la dégradation catalytique de l'orange de méthyle. Ici, la photocatalyse sert également d'outil pour déterminer les différentes terminaisons des nanoparticules SrTiO₃ en tant que nanoparticules terminées par SrO ou TiO₂.

Tableau. 3. Constante de vitesse et pourcentage de dégradation de l'orange de méthyle contre les nanoparticules de TiO₂ terminées par SrTiO₃, SrTiO terminées par SrO₃ et SrTiO₃ non traitées (sono-photocatalyse à 600 secondes d'impulsion).

S/N	Sono-photocatalyse	SrTiO ₃ :TiO ₂	SrTiO ₃ :SrO	SrTiO ₃
1	Constante de vitesse (min ⁻¹)	0,015	0,004	0,002
2	Dégradation (%)	94± 1,6	32,6± 1,6	25,35± 0,9

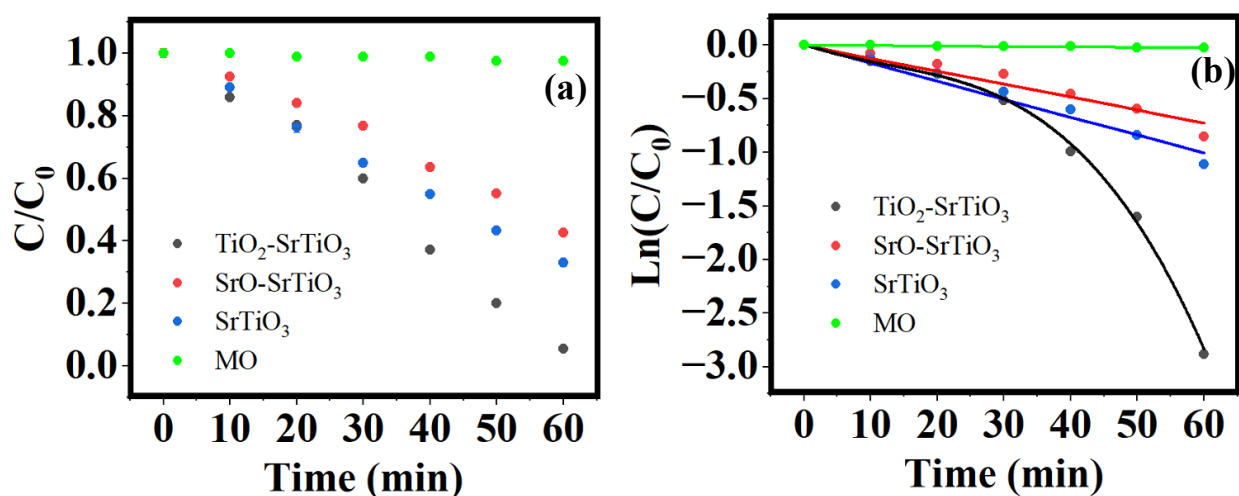


Fig. 5. Tracé de C/C_0 (a) et de $\ln(C/C_0)$ (b) sur la dégradation sono-photocatalytique de l'orange de méthyle par des nanoparticules de SrTiO₃ terminées par TiO₂, SrTiO₃ terminées par de SrO et de SrTiO₃ non traitées (sonification à 600 secondes d'impulsion).

En outre, pour déterminer l'efficacité comparative et la propagation de l'erreur, l'activité photocatalytique avec impulsion de sonification a été réalisée avec TiO₂ (P25, 50 mg/L) avec un paramètre similaire à celui de SrTiO₃. Les résultats montrent que le taux de réaction sur la photocatalyse avec impulsion de sonification contre TiO₂ était de 0,009 à 0,030 (0 à 600 sec) comme illustré dans le Tableau. 4. Les résultats montrent que l'efficacité catalytique du SrTiO₃ terminé par du TiO₂ est deux fois plus élevée que le TiO₂ standard sur une impulsion de sonification de 600 secondes (Fig. 6 a et b). En outre, le tracé du taux de réaction en fonction de l'impulsion de sonification de la dégradation sono-photocatalytique de l'orange de méthyle contre

TiO₂ a été montré dans la Fig. 6c. Les résultats montrent que l'impulsion de sonification augmente l'efficacité catalytique, la sonification améliore le mélange de 0 à 100 secondes (Fig. 6c). L'augmentation immédiate de l'activité catalytique après 100 secondes plutôt que la saturation pourrait être due à l'activation du mécanisme sonocatalytique ou tribocatalytique sur la dégradation de l'orange de méthyle contre TiO₂.

Tableau. 4. Constante de vitesse et pourcentage de dégradation de l'orange de méthyle par rapport au TiO₂ (sono-photocatalyse)

S/N	Impulsion (s)	Constante de vitesse (min ⁻¹)	Taux de dégradation (%)
1	0	0,009	47,3± 2,55
2	6	0,010	48,1± 1,09
3	18	0,010	49,7± 2,93
4	30	0,010	50,1± 0,98
5	60	0,011	51,4± 0,32
6	100	0,011	53,2± 1,88
7	300	0,018	57,5± 3,02
8	600	0,030	59,1± 4,41

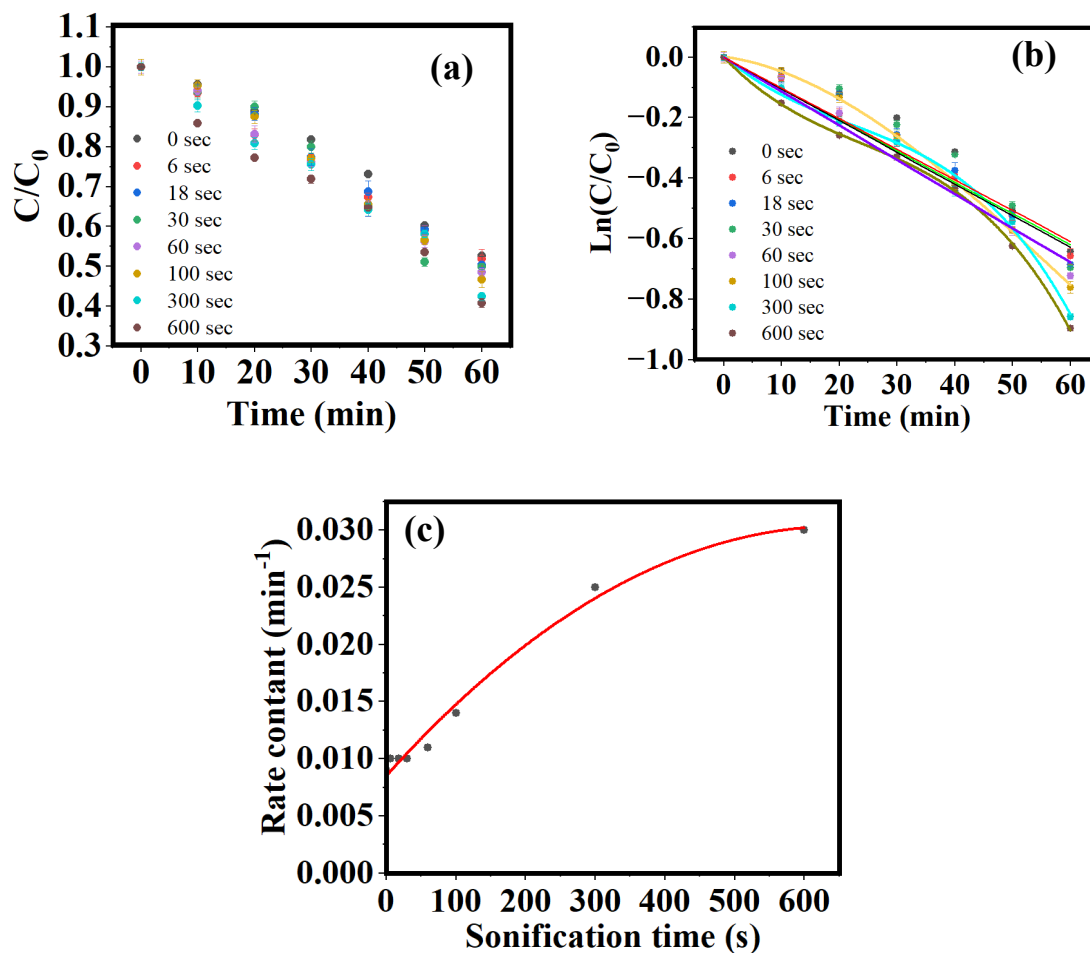


Fig. 6. Tracé de C/C_0 (a), $\ln(C/C_0)$ (b) et vitesse de réaction en fonction de l'impulsion de sonification (c) sur la dégradation sono-photocatalytique de l'orange de méthyle par TiO_2

En outre, afin de déterminer le mécanisme catalytique lors d'un passage immédiat d'une impulsion de sonification de 100 à 600 secondes, l'expérience de photocatalyse a été répétée en l'absence d'impulsion de sonification (impulsion d'extinction de la lumière) avec SrTiO_3 terminé par TiO_2 contre l'orange de méthyle (Tableau 5). Le graphique de la concentration relative montre que l'activité catalytique en l'absence d'irradiation n'a pas eu d'effet sur le taux de réaction (Fig. 7 a et b). En outre, le tracé de la vitesse de réaction en fonction de l'impulsion d'extinction de la lumière n'a pas développé la dégradation exponentielle (Fig. 7c). Ainsi, les résultats montrent que la dégradation catalytique du méthyle-orange contre le SrTiO_3 terminé par le TiO_2 ne suit pas l'effet tribo-catalytique.

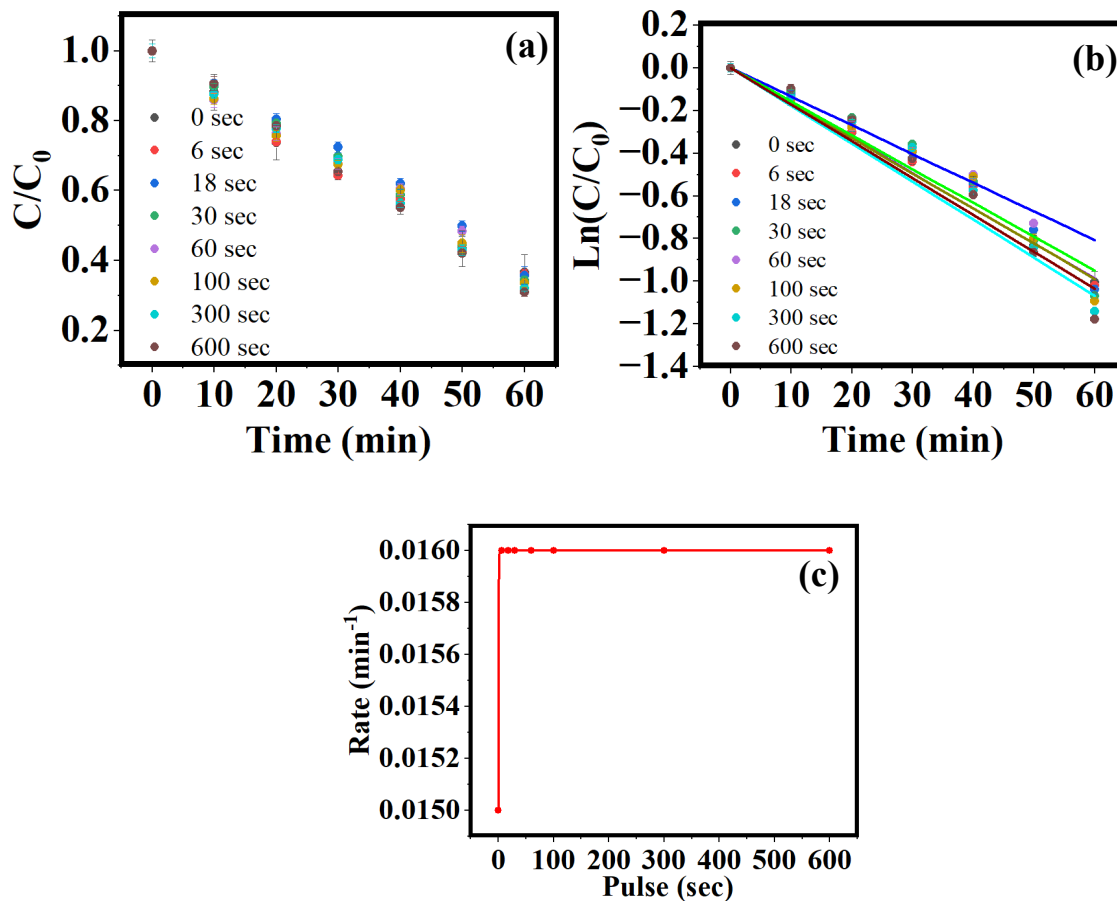


Fig. 7. Tracé de C/C_0 (a), $\ln(C/C_0)$ (b) et de la vitesse de réaction en fonction de l'impulsion d'extinction de la lumière sur la dégradation photocatalytique de l'orange de méthyle par SrTiO_3 terminé par TiO_2 à température ambiante (avec une impulsion d'extinction de la lumière de 600 secondes, sans sonification)

Tableau. 5. Constante de vitesse et pourcentage de dégradation de l'orange de méthyle contre SrTiO₃ terminé par TiO₂ - photocatalyse à 600 secondes d'impulsion d'arrêt de la lumière.

S/N	Impulsion (s)	Constante de vitesse (min ⁻¹)	Taux de dégradation (%)
1	0	0,015	63,3± 3,27
2	6	0,016	63,9± 0,91
3	18	0,016	64,6± 2,20
4	30	0,016	65,6± 1,51
5	60	0,016	66,5± 0,62
6	100	0,016	67,1± 0,34
7	300	0,016	68± 0,90
8	600	0,016	69,1± 1,22

En outre, pour étudier l'effet sono-catalytique sur la dégradation de l'orange de méthyle contre SrTiO₃ terminé par TiO₂, l'expérience de photocatalyse a été répétée avec l'impulsion de sonification (à 60 °C). En effet, l'augmentation de la température augmente la cavitation des bulles et confirme donc l'effet de la sonocatalyse. En général, à haute température, l'effet sono-catalytique augmente la dégradation et diminue la dégradation sur l'effet tribo-catalytique. Le graphique de la concentration relative montre que l'activité catalytique est plus élevée entre 0 et 100 secondes, ce qui explique l'augmentation efficace du mélange réactionnel pour stimuler le transfert de masse entre les nanoparticules et l'orange de méthyle (Fig. 8 a et b). Comme pour l'expérience de sono-photocatalyse à température ambiante, l'augmentation soudaine du taux de réaction de 100 à 300 secondes a été observée avec la sonification à 60 °C, où le taux de réaction est relativement plus élevé à 60 °C qu'à température ambiante (Fig. 8c et Tableau. 6).

Tableau. 6. Constante de vitesse et pourcentage de dégradation de l'orange de méthyle contre SrTiO₃ terminé par TiO₂ - Sono-photocatalyse à 60 °C.

S/N	Impulsion (s)	Constante de vitesse (min ⁻¹)	Taux de dégradation (%)
1	0	0,015	63,3± 3,27
2	6	0,016	65,0± 0,91
3	18	0,018	69,0± 2,20
4	30	0,019	73,7± 1,51
5	60	0,021	76,6± 0,62
6	100	0,047	80,0± 0,34
7	300	0,058	92,7± 0,90
8	600	0,065	96,6± 1,22

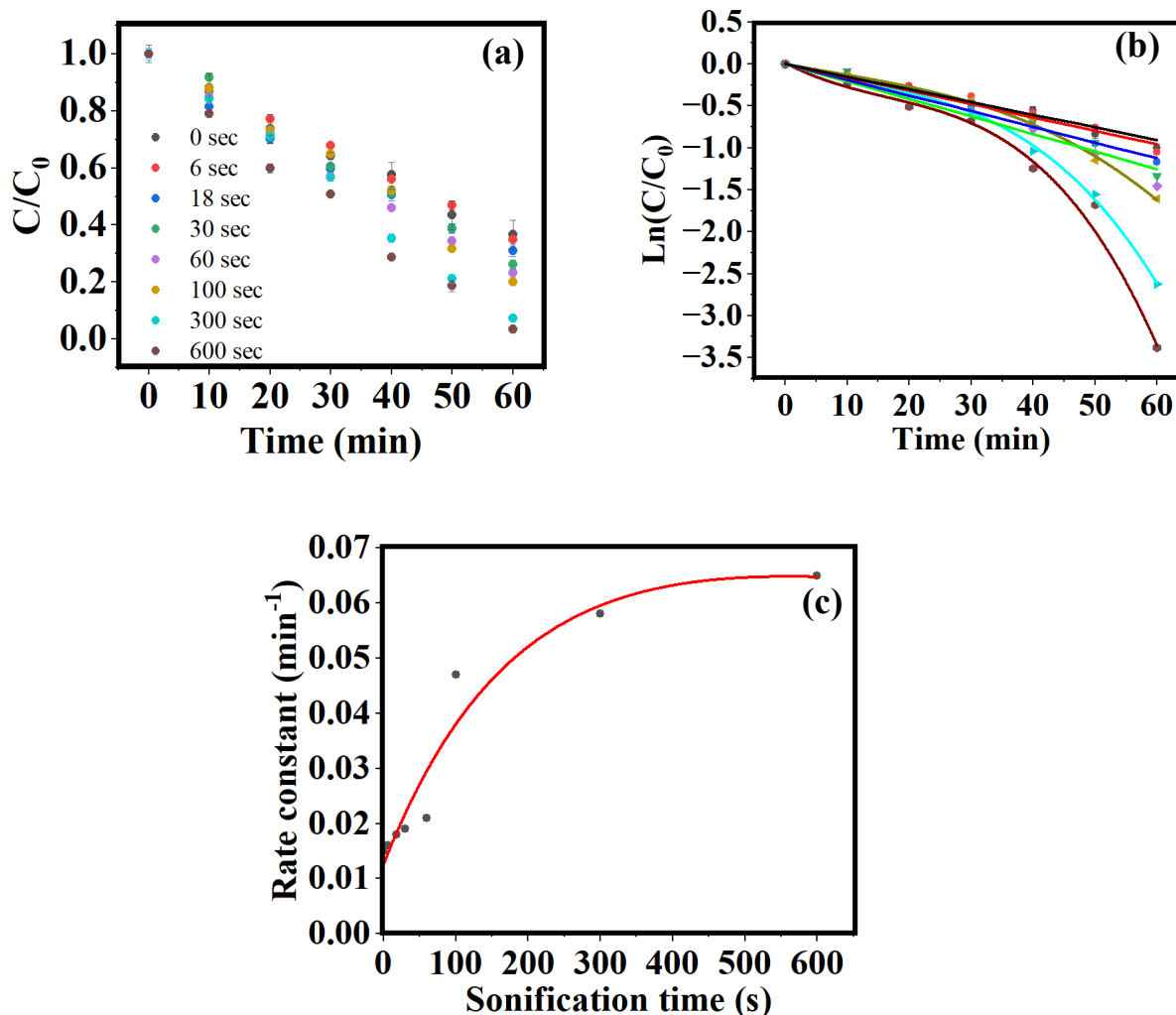


Fig. 8. Tracé de C/C_0 (a), $\ln(C/C_0)$ (b) et vitesse de réaction en fonction de l'impulsion d'extinction de la lumière (c) sur la dégradation sono-photocatalytique de l'orange de méthyle à 60 °C par SrTiO_3 terminé par TiO_2 .

En outre, pour confirmer l'effet de la sonocatalyse, l'expérience catalytique avec une impulsion de sonification avec une impulsion d'arrêt de la lumière à 60 °C (absence d'impulsion) et l'efficacité catalytique ont été déterminées. Le graphique de la concentration relative avec une impulsion différente (0 à 600 s), montre que l'activité catalytique était constante (presque nulle) de 0 à 30 s, avec une légère augmentation à 60 et 100 s et une augmentation de l'activité catalytique de 300 à 600 s (Fig. 9 a&b et Tableau. 7). Le tracé de la cinétique du taux en fonction de l'impulsion de sonification ne suit pas la dégradation exponentielle de l'orange de méthyle et

montre que l'activité catalytique augmente de 300 à 600 secondes, ce qui est dû à l'effet de cavitation des bulles (Fig. 9c).

Tableau. 7. Constante de vitesse et pourcentage de dégradation de l'orange de méthyle contre SrTiO₃ terminé par TiO₂ - Sono-catalyse avec impulsion d'extinction de la lumière à 60 °C.

S/N	Impulsion (s)	Constante de vitesse (min ⁻¹)	Taux de dégradation (%)
1	0	0,0001	0
2	6	0,0001	0
3	18	0,0001	0
4	30	0,0004	0
5	60	0,0004	2,2± 1,10
6	100	0,0004	2,2± 0,93
7	300	0,0015	8,9± 0,98
8	600	0,003	16,8± 0,40

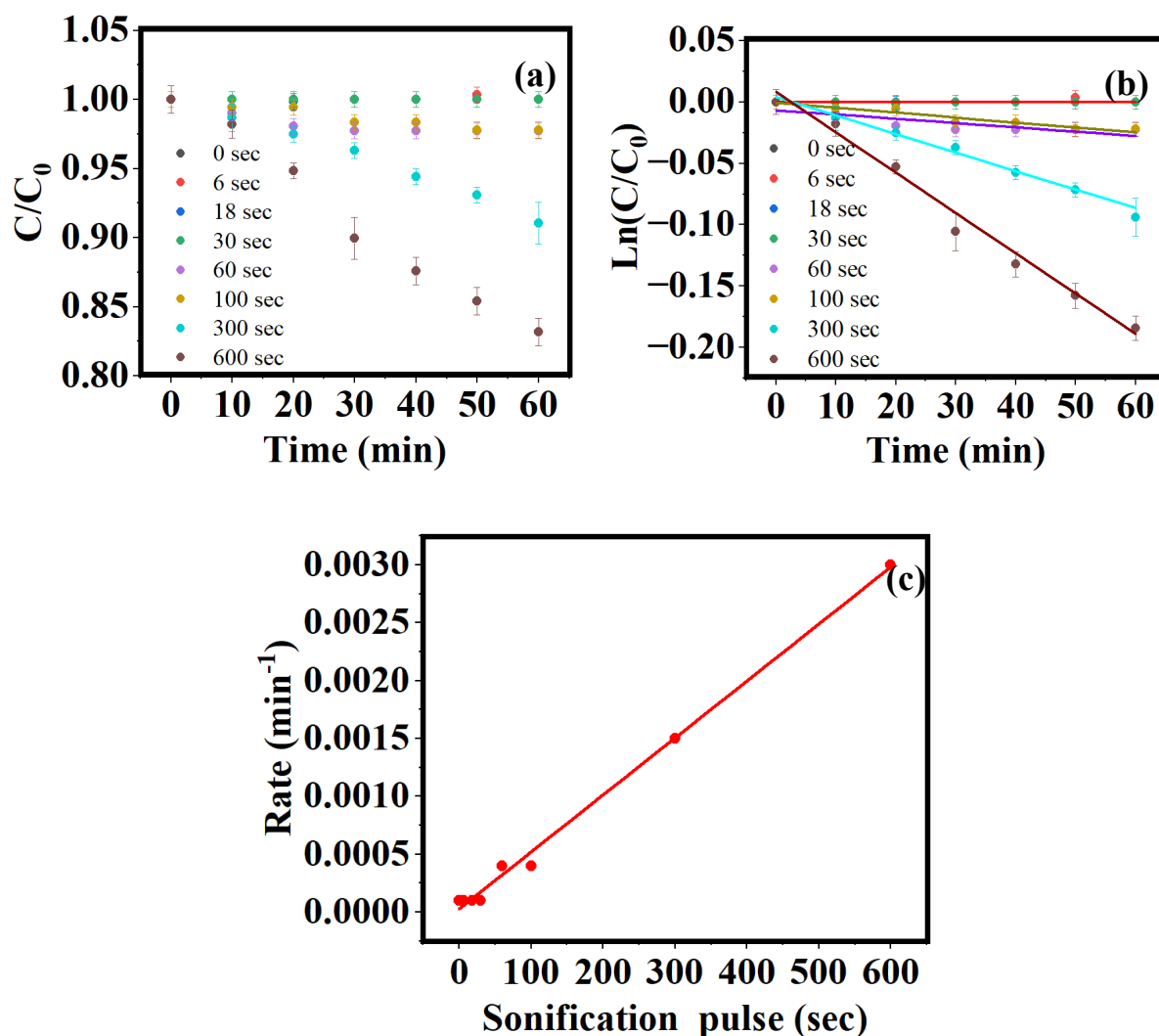


Fig. 9. Tracé de C/C_0 (a), $\ln(C/C_0)$ (b) et vitesse de réaction en fonction de l'impulsion d'extinction de la lumière (c) sur la dégradation sono-catalytique de l'orange de méthyle à 60 °C par SrTiO_3 terminé par TiO_2

3. Conclusion

Dans la recherche d'une solution pour stimuler l'efficacité des propriétés catalytiques du nanomatériau sur l'ingénierie de surface de SrTiO_3 (SrO terminé et TiO_2 terminé). La terminaison de la surface du SrTiO_3 a été principalement caractérisée par la formation d'une couche de carbonate sur la terminaison du SrO , ce qui a été confirmé par la spectroscopie Raman. Le spectre Raman du SrTiO_3 terminé par TiO_2 n'a pas montré de pic de carbonate, alors que le pic de carbonate a été observé sur le SrTiO_3 terminé par SrO et le SrTiO_3 non traité. L'activité photocatalytique du SrTiO_3 modifié en surface montre que le SrTiO_3 terminé par TiO_2 était plus

efficace que le SrTiO₃ terminé par SrO et les nanoparticules de SrTiO₃ non traitées. La carbonatation à la surface de la couche de SrO bloque le site réactif pour une interaction efficace entre la nanoparticule et le polluant. Pour stimuler l'activité catalytique du SrTiO₃ contre le méthyle orange et résoudre l'étape limitant le taux de photocatalyse (transfert de masse), l'activité catalytique des nanoparticules de SrTiO₃ a été réalisée en combinant l'impulsion de sonification et le système d'irradiation. L'activité catalytique de SrTiO₃ terminées par TiO₂ augmente de 1,7 fois avec la sonification, ce qui est relativement plus élevé que la photocatalyse sans sonification. L'activité sono-photocatalytique stimule le mélange et résout ainsi l'une des limitations de la photocatalyse (transfert de masse). Les résultats montrent que l'impulsion de sonification augmente l'efficacité catalytique, la sonification améliore le mélange de 0 à 100 secondes. Les résultats concluent que la combinaison de la sonification et de l'irradiation prouve l'effet sono-photocatalytique. En fait, la catalyse est un phénomène de surface, l'ingénierie de surface accordable permet de montrer le changement dans la propriété catalytique du nanomatériau.